

---

## Large 3D maps of bone tissues at single-cell resolution

**Auteur :** Dequiedt, Lucie

**Promoteur(s) :** Geris, Liesbet

**Faculté :** Faculté des Sciences appliquées

**Diplôme :** Master en ingénieur civil biomédical, à finalité spécialisée

**Année académique :** 2020-2021

**URI/URL :** <http://hdl.handle.net/2268.2/13019>

---

### *Avertissement à l'attention des usagers :*

*Tous les documents placés en accès ouvert sur le site le site MatheO sont protégés par le droit d'auteur. Conformément aux principes énoncés par la "Budapest Open Access Initiative"(BOAI, 2002), l'utilisateur du site peut lire, télécharger, copier, transmettre, imprimer, chercher ou faire un lien vers le texte intégral de ces documents, les disséquer pour les indexer, s'en servir de données pour un logiciel, ou s'en servir à toute autre fin légale (ou prévue par la réglementation relative au droit d'auteur). Toute utilisation du document à des fins commerciales est strictement interdite.*

*Par ailleurs, l'utilisateur s'engage à respecter les droits moraux de l'auteur, principalement le droit à l'intégrité de l'oeuvre et le droit de paternité et ce dans toute utilisation que l'utilisateur entreprend. Ainsi, à titre d'exemple, lorsqu'il reproduira un document par extrait ou dans son intégralité, l'utilisateur citera de manière complète les sources telles que mentionnées ci-dessus. Toute utilisation non explicitement autorisée ci-avant (telle que par exemple, la modification du document ou son résumé) nécessite l'autorisation préalable et expresse des auteurs ou de leurs ayants droit.*

---



UNIVERSITY OF LIÈGE - FACULTY OF APPLIED SCIENCES  
JOHNS HOPKINS UNIVERSITY - INSTITUTE FOR NANOBIO TECHNOLOGY

---

# Large 3D Maps of Bone Tissues at Single-Cell Resolution

---

Master Thesis conducted by

**Lucie Dequiedt**

with the aim of obtaining the degree of Master in Biomedical Engineering

**Supervisors :**

Pr. Denis WIRTZ

Pr. Liesbet GERIS

Academic Year 2020-2021

# Acknowledgements

I would like to begin by paying my special regards to my advisor, Pr.Denis Wirtz. He is the reason why I had the chance to work on such an exciting and stimulating project. Being part a top-level research laboratory such as his had been a lifelong dream that is now fulfilled thanks to his support.

I would also like to express my deepest gratitude to all members of the Wirtz Lab. In particular, I would like to recognize the invaluable assistance of Ashley Kiemen. Without her insights and precious advice, this project would not have been completed. I would also like to thank Pr.Pei-Hsun Wu for the many helpful discussions.

Furthermore, I would like to acknowledge Pr.Liesbet Geris for her assistance and supervision in the practical realization of this project.

Finally, I would like to express my deepest thanks to my friends and family for their unwavering support during the course of my studies. In particular, I would like to thank my parents for their essential help and guidance every step of the way.

# Abstract

Breast and prostate cancer are amongst the most common and deadly forms of cancer namely due to the formation of metastasis, which is the leading cause of death in both cancer types. In particular, bone tissue is a preferential site for metastasis formation, with 70% of metastatic breast and prostate cancers developing bone metastases. Their important death rates are mainly due to the lack of understanding of the bone metastasis formation process, which prevented the scientific community from finding effective treatments limiting the spread of the disease. Two main models have historically been used to study bone metastasis development - *in vitro* 2D cultures of cancer cells and *in vivo* animal models - but none of them succeeded at faithfully recapitulating the human bone microenvironment, which is thought to play a crucial role in the process. There is therefore a real need for better biomimetic models that would give new insights on the formation of bone metastasis, eventually leading to the development of drugs specifically targeting this process. In recent years, tissue engineered models appeared as promising alternatives to conventional models, although they still require important improvements to be considered as truly recapitulating tumor features *in vitro*. The work developed here thus aimed at ultimately deriving new ways of improving bone tissue engineered models for the study of breast and prostate cancer metastasis by comparing their 3D tissular and cellular contents with the ones of human bone tissues harboring metastasis. Through the use of CODA on seven tissue engineered bone samples infused with either prostate or breast cancer cells, this report presents the first ever in-depth characterization of tissue engineered models at the millimeter scale and with single-cell resolution. Indeed, CODA allowed for the creation of fully annotated 3D digital reconstructions of the different samples, which were then used to perform quantification of cellular and tissular contents. It has led to preliminary results that need to be confirmed by further investigations before being compared with quantitative results obtained on *in situ* bone metastasis of breast and prostate cancer.

**Keywords:** Bone metastasis, Tissue Engineering, Convolutional Neural Networks, Biomedical Image Registration, Cell Detection

# Contents

<b>List of Figures</b>	<b>iv</b>
<b>List of Tables</b>	<b>vii</b>
<b>1 Introduction</b>	<b>1</b>
1 Motivation . . . . .	1
2 Aims of the Thesis . . . . .	2
3 Organization of the Thesis . . . . .	2
<b>2 Background</b>	<b>3</b>
1 Healthy Bone Physiology . . . . .	3
1.1 The Bone at the Cellular Level . . . . .	3
1.1.1 Osteoblasts . . . . .	4
1.1.2 Osteocytes and Bone Lining Cells . . . . .	4
1.1.3 Osteoclasts . . . . .	5
1.2 The Bone at the Tissue Level . . . . .	5
2 Breast and Prostate Cancer Bone Metastasis . . . . .	8
2.1 Colonization . . . . .	9
2.2 Dormancy . . . . .	10
2.3 Reactivation and Development . . . . .	10
2.4 Reconstruction . . . . .	10
3 Models of Bone Metastasis . . . . .	12
3.1 Tissue-Engineered Models . . . . .	12
3.1.1 Scaffold material . . . . .	13
3.1.2 Incorporating Growth Factors, Proteins or Minerals . . . . .	14
3.1.3 Choice of co-cultured cells . . . . .	14
3.2 Current Challenges . . . . .	14
<b>3 Theoretical Bases</b>	<b>15</b>
1 Image Registration . . . . .	15
1.1 Generalities . . . . .	15
1.2 Intensity-based Image Registration . . . . .	17
1.2.1 Geometric Transformation . . . . .	18
1.2.2 Interpolation . . . . .	19
1.2.3 Similarity Measure . . . . .	19
1.2.3.1 Radon Transform . . . . .	20
1.2.3.2 Problem Statement and Implementation . . . . .	21
1.2.4 Optimisation . . . . .	23
2 Deep Learning Classification . . . . .	24

2.1	One Neuron Perceptron Model . . . . .	24
2.2	Multilayer Perceptron . . . . .	27
2.3	Convolutional Neural Networks . . . . .	28
2.3.1	Architecture Overview . . . . .	28
2.3.1.1	Convolutional Layer . . . . .	29
2.3.1.2	Non-Linear Layer . . . . .	30
2.3.1.3	Pooling Layer . . . . .	30
2.3.1.4	Fully-connected Layer . . . . .	32
2.3.2	Network Training . . . . .	32
2.3.2.1	Loss Function . . . . .	32
2.3.2.2	Optimization Algorithm . . . . .	33
2.3.2.3	Hyperparameters . . . . .	34
2.3.2.4	Network troubleshooting . . . . .	35
2.3.3	Residual Networks . . . . .	35
3	Color Deconvolution . . . . .	38
<b>4</b>	<b>Materials and Methods</b>	<b>40</b>
1	Development Environment . . . . .	40
2	Overall Workflow . . . . .	40
3	Sample Acquisition . . . . .	42
3.1	Tissue Engineering Process . . . . .	42
3.2	Sample Preparation and Scanning . . . . .	44
4	Tissue Semantic Segmentation . . . . .	45
4.1	Training and Validation Datasets Creation . . . . .	46
4.2	CNN Training and Validation . . . . .	46
4.3	Section Labelling . . . . .	47
5	Sample 3D Reconstruction . . . . .	49
5.1	Image Registration . . . . .	49
5.2	Creation of 3D Renderings . . . . .	51
6	Quantification . . . . .	52
6.1	Quantification at the Tissue Level . . . . .	52
6.1.1	Calculation of Tissue Content and Volume . . . . .	52
6.1.2	Morphological Characterization of Scaffold Pieces . . . . .	52
6.2	Quantification at the Cell Level . . . . .	52
6.2.1	Nuclei Detection on histological sections . . . . .	53
6.2.1.1	Color Deconvolution . . . . .	53
6.2.1.2	Filtering . . . . .	54
6.2.1.3	Peak Intensity Detection . . . . .	54
6.2.1.4	Performance Assessment and Validation . . . . .	55
6.2.2	Cell Count and Tissue Cell Density . . . . .	55
<b>5</b>	<b>Results</b>	<b>57</b>
1	CODA . . . . .	57
1.1	Semantic Segmentation . . . . .	58
1.2	Image Registration . . . . .	60
1.3	Samples Reconstruction . . . . .	61
2	Quantification . . . . .	62
2.1	Quantification at the Tissue Level . . . . .	62

2.1.1	Tissue Content and Volume . . . . .	62
2.1.2	Morphological Characterization of Scaffold Pieces . . . . .	63
2.2	Quantification at the Cell Level . . . . .	65
2.2.1	Nuclei Detection on Histological Sections . . . . .	65
2.2.1.1	Color Deconvolution . . . . .	66
2.2.1.2	Filtering . . . . .	67
2.2.1.3	Peak Intensity Detection and Testing . . . . .	68
2.2.1.4	Validation . . . . .	70
2.2.2	Cellular Content . . . . .	71
<b>6</b>	<b>Discussion</b>	<b>73</b>
1	Quantification . . . . .	73
1.1	Quantification at the Tissular Level . . . . .	74
1.1.1	Tissue Content . . . . .	74
1.1.2	Morphological Characterization of Scaffold Pieces . . . . .	76
1.2	Quantification at the Cellular Level . . . . .	79
1.2.1	Cellular Content and Cellular Density . . . . .	79
2	Limitations and Key Contributions . . . . .	81
3	Future work . . . . .	81
<b>7</b>	<b>Conclusions</b>	<b>83</b>
<b>A</b>		<b>85</b>
1	Identified Tissue Subtypes . . . . .	85
2	Common Deep Learning Model Errors . . . . .	87
3	Labeled Digital Reconstructions . . . . .	89
4	Scaffold Characterization Results . . . . .	92
	<b>Bibliography</b>	<b>94</b>

# List of Figures

2.1	Osteoblast differentiation. (Taken from [1]) . . . . .	4
2.2	Osteoclast differentiation. (Taken from [1]) . . . . .	5
2.3	Diagram of compact bone. (Taken from [2]) . . . . .	6
2.4	Diagram of trabecular bone. (Taken from [2]) . . . . .	7
2.5	Metastatic invasion of cancer cells to the bone. (Taken from [3]) . . . . .	8
2.6	Interactions supporting breast cancer cell bone homing. (Taken from [4])	9
3.1	Diagram of typical algorithms used in intensity-based registration techniques. (Taken from [5]) . . . . .	16
3.2	Diagram of typical feature-based registration algorithms. (Taken from [5])	17
3.3	Global (top line) versus local (bottom line) registration model. (Taken from [6]) . . . . .	18
3.4	Definition of the Radon transform. (Taken from [7]) . . . . .	20
3.5	Computation of the Radon Transform by the <code>radon</code> built-in <code>Matlab</code> function. (Taken from [8]) . . . . .	22
3.6	Simplified structure of a neuron. (Taken from [9]) . . . . .	25
3.7	The one neuron perceptron model. (Adapted from [10] and [11]) . . . . .	25
3.8	Example of a multilayer perceptron (MLP) with 3 inputs, 2 hidden layers of 4 neurons each and 2 outputs. (Adapted from [12]) . . . . .	27
3.9	Simple convolutional neural network (CNN) architecture. (Adapted from [13]) . . . . .	29
3.10	Convolutional layer and formation of activation maps. (Taken from [12])	30
3.11	Implementation of the convolution operation as matrix multiplication (stride = 2). (Adapted from [13]) . . . . .	31
3.12	Functioning of the pooling layer. (Taken from [13]) . . . . .	31
3.13	Illustrative representation of a convolutional neural network (CNN) architecture for image classification. (Taken from [14]) . . . . .	32
3.14	<i>Bottleneck</i> building block for residual networks (ResNet)50. (Taken from [15]) . . . . .	37
4.1	CODA workflow adapted to tissue engineered bone samples. . . . .	41
4.2	Tissue engineering protocol schematic. (Taken from [16]) . . . . .	43
4.3	Set up for cancer cells infusion inside tissue engineered bones. (Courtesy of Laboratory for Stem Cells and Tissue Engineering, Columbia University)	44
4.4	Overview of the tissue semantic segmentation workflow. . . . .	45
4.5	Histological image registration workflow. . . . .	50
4.6	Effective tissue section thickness extrapolation. (Taken from [17]) . . . . .	55



5.1	Confusion matrix displaying predicted vs true class outcomes for all deep learning classes. Precision and recall per class (%) are in row beneath and to the right of matrix respectively. . . . .	59
5.2	Semantic segmentation of the histological sections. . . . .	60
5.3	Comparative overlays of successive images. . . . .	61
5.4	Fully labeled digital reconstruction of sample R3-T1. . . . .	61
5.5	Tissue composition [%] of the different tissue engineered bone models. . .	62
5.6	Zoom in on the lacunae inside the bovine bone scaffold in sample R3-T1. . .	63
5.7	Top view of the bovine trabecular bone scaffold pieces in samples R3-T1. . .	64
5.8	Morphological characterization of scaffold pieces inside each sample. . . .	65
5.9	Comparison of hematoxylin channel images obtained using color deconvolution with different staining matrices. (He : hematoxylin, s.t : staining matrix) . . . . .	67
5.10	Comparison of the results using different filtering combinations on the inverse of the hematoxylin channel image obtained with the visually determined staining matrix. . . . .	68
5.11	Visual representation of the manually and automatically detected cells on the testing image (150 cells). . . . .	70
5.12	Visual representation of the manually and automatically detected cells on the validation image (388 cells). . . . .	71
5.13	Detected cells inside sample R3-T1. . . . .	71
6.1	Percentage of tissue inside the samples in function of the cancer cell line. . .	74
6.2	Micrograph of woven bone. HE stained section of rabbit bone, from the histology slide collection of CAHID, University of Dundee. (Scale bar = 380 $\mu\text{m}$ , 10x) (Taken from [18].) . . . . .	75
6.3	K-means clustering analysis of the percentage of scaffold in function of the percentage of ECM inside the different samples. (2 clusters) . . . . .	76
6.4	Mean morphology of a scaffold piece in a sample in function of the cancer cell line used in the sample. . . . .	77
6.5	Bounding boxes. (Taken from [19]) . . . . .	78
6.6	Shapes and their respective solidity. (Taken from [19]) . . . . .	78
6.7	Cell counts in each sample in function of the cancer cell line used in the sample. . . . .	79
6.8	Cell densities in each sample in function of the cancer cell line used in the sample. . . . .	80
A.1	Semantic segmentation legend. . . . .	87
A.2	CNN model struggles at distinguishing extracellular matrix (ECM) and cartilage while it tends to label round or elongated cells as extracellular matrix (ECM). (Legend in FIGURE A.1) . . . . .	87
A.3	CNN model often mistakes whitespace and cartilage for extracellular matrix (ECM). (Legend in FIGURE A.1) . . . . .	88
A.4	CNN model tends to exaggerate fibroblasts boundaries in cartilage layer while it labels a lot of whitespace as extracellular matrix (ECM). (Legend in FIGURE A.1) . . . . .	88
A.5	Fully labeled digital reconstruction of sample R3-T2. . . . .	89
A.6	Fully labeled digital reconstruction of sample R3-T3. . . . .	89
A.7	Fully labeled digital reconstruction of sample R3-T4. . . . .	90

A.8 Fully labeled digital reconstruction of sample R4-T1. . . . .	90
A.9 Fully labeled digital reconstruction of sample R4-T2. . . . .	91
A.10 Fully labeled digital reconstruction of sample R4-T3. . . . .	91

# List of Tables

3.1	Examples of activation functions. (Adapted from [11]) . . . . .	26
3.2	Definitions of common hyperparameters examples in convolutional neural network (CNN)s. . . . .	34
4.1	Values and definitions of the options used during training of the deep neural network. [20] . . . . .	48
4.2	Cell subtypes and the corresponding mean nuclear diameter measured in <b>Aperio ImageScope</b> . . . . .	56
5.1	Samples, their dimensions [mm] and the cancer cell line they were infused with. . . . .	57
5.2	Tissue volume [ $10^{-3}\text{mm}^3$ ] of the different tissue engineered bone models. . . . .	63
5.3	Mean Scaffold porosity in each sample. . . . .	63
5.4	Morphological assessment of scaffold pieces in sample R3T1. . . . .	64
5.5	Percentage of correctly detected cells for each combination of staining matrix and filtering technique on the 150 cells of the testing image. [%] . . . . .	69
5.6	Percentage of false positive for each combination of staining matrix and filtering technique on the 150 cells of the testing image. [%] . . . . .	69
5.7	Cell count, total and for each cell subtype, in the different samples. . . . .	72
5.8	Cell densities [cells/ $10^{-3}\text{mm}^3$ ], in bulk and in the different tissue subtypes, inside the different samples . . . . .	72
A.1	Identified Tissue Subtypes. . . . .	86
A.2	Morphological assessment of scaffold pieces in sample R3T2. . . . .	92
A.3	Morphological assessment of scaffold pieces in sample R3T3. . . . .	92
A.4	Morphological assessment of scaffold pieces in sample R3T4. . . . .	92
A.5	Morphological assessment of scaffold pieces in sample R4T1. . . . .	92
A.6	Morphological assessment of scaffold pieces in sample R4T2. . . . .	93
A.7	Morphological assessment of scaffold pieces in sample R4T3. . . . .	93

# Acronyms

<b>ADAM</b>	adaptive moment estimation
<b>ANN</b>	artificial neural networks
<b>BMPs</b>	bone morphogenic proteins
<b>BMSCs</b>	bone marrow stromal Cells
<b>BSP</b>	bone sialoprotein
<b>CFU-M</b>	macrophage colony forming units
<b>CNN</b>	convolutional neural network
<b>CPs</b>	control points
<b>CXCL12</b>	C-X-C motif chemokine 12
<b>CXCR4</b>	C-X-C chemokine receptor type 4
<b>DL</b>	deep learning
<b>ECM</b>	extracellular matrix
<b>GDF15</b>	growth differentiation factor 15
<b>H&amp;E</b>	hematoxylin and eosin
<b>HSCs</b>	hematopoietic stem cells
<b>IL</b>	interleukin
<b>MCSF</b>	macrophage colony-stimulating factor
<b>MLP</b>	multilayer perceptron
<b>MSC</b>	mesenchymal stem cell
<b>MSE</b>	mean squared error
<b>OD</b>	Optical Density
<b>OPG</b>	osteoprotegerin
<b>OPN</b>	osteopontin

**PCL** poly( $\epsilon$ -caprolactone)  
**PTHrP** parathyroid hormone-related protein  
**RANK** receptor activator of nuclear factor  $\kappa$ - $\beta$   
**RANKL** RANK Ligand  
**ReLU** rectified linear unit  
**ResNet** residual networks  
**RGB** red green blue  
**RT** Radon Transform  
**SDF-1** stromal-Derived Factor  
**SGD** stochastic gradient descent  
**SVM** support vector machine  
**VEGF** vascular endothelial growth factor

# Chapter 1

## Introduction

### 1 Motivation

Breast cancer is the most common form of cancer (281,550 projected cases in 2021) and the second leading cause of cancer death (43,600 projected deaths in 2021) among American women. Among American men, the most common form of cancer and the second leading cause of cancer death is prostate cancer, with 248,530 cases and 34,180 deaths projected in 2021. [21]

In Belgium, breast and prostate cancers are respectively the first and the second most common types of cancer. Among the 70,468 cancer cases diagnosed in Belgium in 2018, 11,009 were breast cancers while 9,800 were prostate cancers. [22][23]

The major cause of death in patients diagnosed with either breast or prostate cancer is metastasis, the spread of cancer cells from an organ of origin to distant organs and tissues. [24][25] One of their most common sites for metastasis is the bone, especially bones rich in red marrow and trabecular bone. Seventy percent of patients with metastatic prostate or breast cancer have bone metastasis. [26]

So many patients die from bone metastasis because the mechanisms by which latent breast and prostate cancer evolve towards metastasis are still poorly understood, preventing the scientific community from finding effective and specific treatments options. Instead, current therapeutic strategies, including chemotherapy, target the highly proliferating primary tumor cells, allowing the low-proliferating metastatic ones to spread to other organs, where they resist conventional treatments, proliferate and eventually cause failure. In bones, metastatic cells can lead to important complications, known as skeletal-related events. They include hypercalcemia, pathological fractures, spinal compression and bone pain, often resulting in a poor prognosis. [27][4] There is not a single FDA-approved drug that specifically target metastatic disease. All current treatments reduce metastatic spread as a by-product of primary tumor shrinkage.

Another reason there are so few therapeutic options for patients with metastatic disease is the lack of good pre-clinical models, such a mice or non-human primates, that properly recapitulate the metastatic cascade. There is therefore a clear need for adequate experimental models enabling the search for effective treatments against metastasis.

Over the years, an important number of studies, making use of *in vitro* 2D cell cul-

ture or *in vivo* animal models, have been conducted with the aim of fulfilling this need. However, none of these models have proven to be suitable. Indeed, cancer cells cultured *in vitro* fail to express their cancer phenotype while mouse bone *in vivo* does not allow for cancer cell invasion.

In the last decade, tissue engineered models, presented themselves as ways of bridging the gap between conventional 2D cell cultures and animal models. Produced from stem cells inside 3D biomaterial scaffolds, their goal is to provide a predictive, inexpensive and low-time consuming substrate that faithfully reproduces bone microenvironment in order to study its impact on cancer biology.

Nonetheless, even current state-of-the-art tissue engineered constructs still face major challenges to fully recapitulate tumors features *in vitro*. There is thus a real need for improving current bioengineered solutions. [28]

## 2 Aims of the Thesis

This thesis aims at providing an in-depth characterization of bone tissue engineered models for the study of prostate and breast cancer metastasis at the cellular and tissular level using the recently introduced CODA method. [17] CODA allows to image large volumes of tumors and tissues at single-cell resolution. It is hoped that, by ultimately comparing their organization and cellular content with the ones of actual bone tissues harboring metastasis, new leads on how to make these models more accurate can be derived.

Our work applied CODA to serially sectioned bone tissue engineered models infused with either breast or prostate cancer cells. This allowed to create 3D maps of the different histological samples with single-cell resolution in which the different tissue sub-types were annotated through the use of deep learning approaches. These 3D maps were then used to accurately quantify cellular content and organization in the different samples.

## 3 Organization of the Thesis

This dissertation is divided in seven chapters.

The first chapter motivates the study and presents the key objectives of the thesis. The second chapter presents the overall background of the research. Therefore, it provides the reader with different insights about bone physiology, the formation of breast and prostate cancer bone metastasis as well as an introduction to the different possible models to study this phenomenon. The third chapter lays the theoretical bases of the different techniques used by CODA. It namely provides an introduction to image registration, deep learning techniques and color deconvolution. The fourth chapter provides a description of the materials and methods used in this work. Therefore, it begins by detailing the tissue engineering process and continues by explaining the different steps involved in the use of CODA. The fifth chapter accounts for presenting the results of the different computations while the sixth discusses them. Finally, the last chapter draws different conclusions and presents future perspectives.

# Chapter 2

## Background

This chapter provides the rationale and background of the study. We introduce healthy bone physiology followed by our current knowledge about bone metastasis. Finally, the most commonly used models of tumor metastasis are presented and compared.

### 1 Healthy Bone Physiology

The bone is a dynamic tissue that serves different physiological purposes, including providing support for locomotion and protection for vulnerable internal organs as well as forming a reservoir for calcium and phosphate ions. The implementation of these two functions is ensured by a crucial process, known as *bone remodeling*, which allows for the prevention of bone damage build-up but also the maintenance of bone mechanical resistance and calcium homeostasis. [1][29]

#### 1.1 The Bone at the Cellular Level

Bone remodeling is defined as the removal and replacement of old or damaged bone with new bone matrix. It mainly involves three types of cells: *osteoblasts*, *osteoclasts* and *osteocytes*. Osteoblasts are responsible for the formation and mineralization of the bone matrix while osteoclasts are bone-resorbing cells and osteocytes, influenced by mechanical cues and systemic hormones, oversee the overall remodeling process. Generally, bone remodeling is broken down in four sequential phases : [29]

1. The *activation phase* in which osteoclasts progenitors are drawn to the damaged bone surface
2. The *resorption phase* in which damaged bone is resorbed by mature osteoclasts
3. The *reversal phase* in which osteoclasts die and osteoblast progenitors are recruited
4. The *formation phase* in which new bone matrix is produced by mature osteoblasts and becomes mineralized



### 1.1.1 Osteoblasts

Osteoblasts, bone-lining cells and osteocytes share a same multipotent precursor of mesenchymal origin, called a mesenchymal stem cell (MSC), which can also give rise to chondrocytes, adipocytes, myocytes and fibroblasts (FIGURE 2.1).

The first step of the overall osteoblast differentiation process begins by the differentiation, under the control of the transcription factor SOX9, of a MSC into an osteochondroprogenitor. In turn, the osteochondroprogenitor, this time under the successive influences of two other transcription factors RUNX2 and Osterix, gives rise to an osteoblast. Osteochondroprogenitors can also differentiate into chondrocytes, hence their name. [1][29]

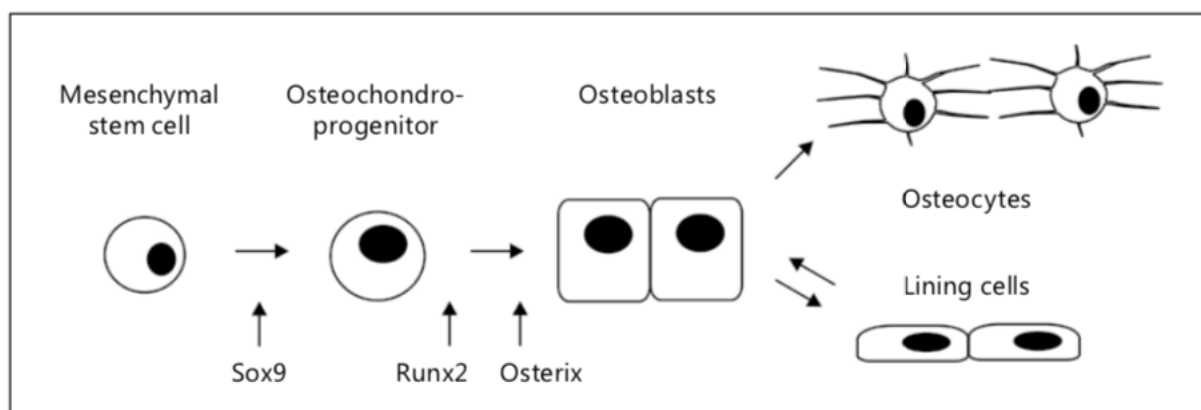


**Figure 2.1:** Osteoblast differentiation. (Taken from [1])

The main role of osteoblasts is to produce the mineralised extracellular bone matrix, which is first secreted as unmineralised osteoid. The osteoid is made up of over 90% of type I collagen while the remaining 10% include other molecules such as glycoproteins and proteoglycans. Other proteins contributing to mineralisation are also secreted, namely alkaline phosphatase, osteocalcin and osteopontin. The osteoid gets mineralised by accumulation of hydroxyapatite, a form of calcium phosphate. Nonetheless, the exact mechanisms enabling the mineralisation process are still poorly understood. [1][29]

### 1.1.2 Osteocytes and Bone Lining Cells

As osteoblasts form bone matrix, some undergo a final differentiation event in which they become osteocytes that get entrapped within lacunae in the osteoid. Osteocytes are closely connected through a network of dendritic cellular processes in canaliculi.

Once they stop producing bone, osteoblasts become bone lining cells that sit on the bone surface. However, once again, this transition is a poorly understood process.

Although osteocytes and bone lining cells represent the largest number of cells in mineralised bone, they are actually the least described and least understood of the cells making up this tissue. [1][29]

### 1.1.3 Osteoclasts

Osteoclast differentiation is illustrated in FIGURE 2.2. Osteoclasts arise from circulating hematopoietic stem cells of the monocyte/macrophage lineage. These hematopoietic precursors express receptors for the macrophage colony-stimulating factor (MCSF) and thus form macrophage colony forming units (CFU-M), the common precursor of osteoclasts and macrophages, after the release of MCSF by osteoblasts. MCSF has the effect of stimulating the production of receptor activator of nuclear factor  $\kappa$ - $\beta$  (RANK) at the surface of osteoclasts precursors. Therefore, the key regulator of osteoclastogenesis is the RANK Ligand (RANKL), also expressed by osteoblasts. Upon their activation by the RANKL-RANK bond, CFU-M further differentiate into mono nucleated osteoclasts that subsequently fuse to become multinucleated immature osteoclasts. Osteoblasts can also down regulate osteoclastogenesis by producing osteoprotegerin (OPG), a decoy receptor inhibiting the RANKL-RANK interaction. Multinucleated osteoclasts reach full maturity after their interaction with osteoblasts. [1][29]

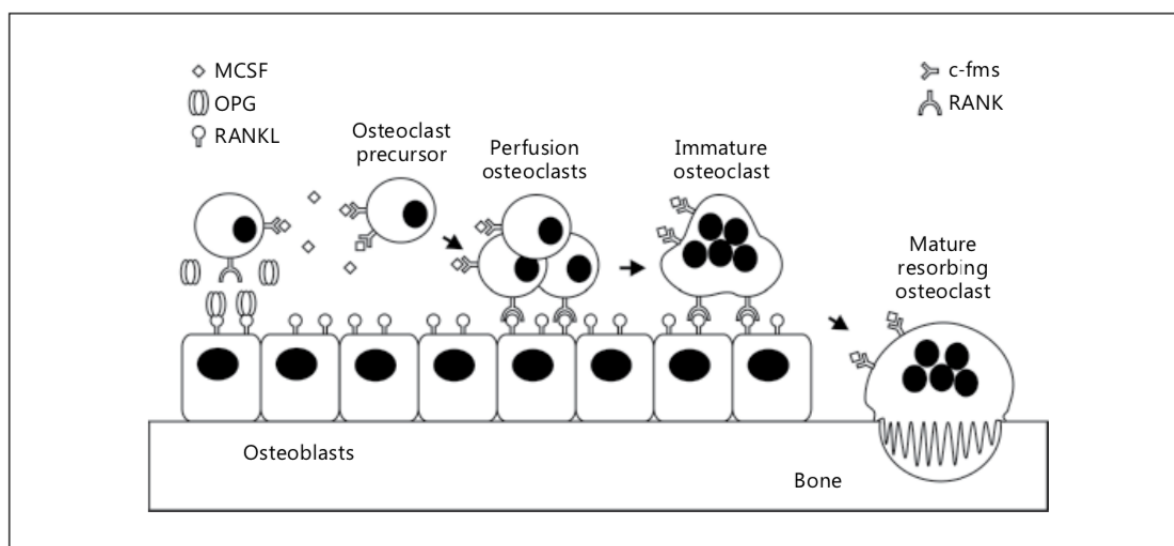


**Figure 2.2:** Osteoclast differentiation. (Taken from [1])

The main function of osteoclasts is to resorb the bone matrix. They perform this function by secreting acids, proteases and matrix metalloproteinases in the sealed compartment that is formed by the tight junction between the bone surface and the cell basal membrane. [1][29]

## 1.2 The Bone at the Tissue Level

At the macroscopic scale, bone tissue can either be *cortical* or *trabecular*. Both bone types are respectively illustrated in FIGURES 2.3 and 2.4. [1]

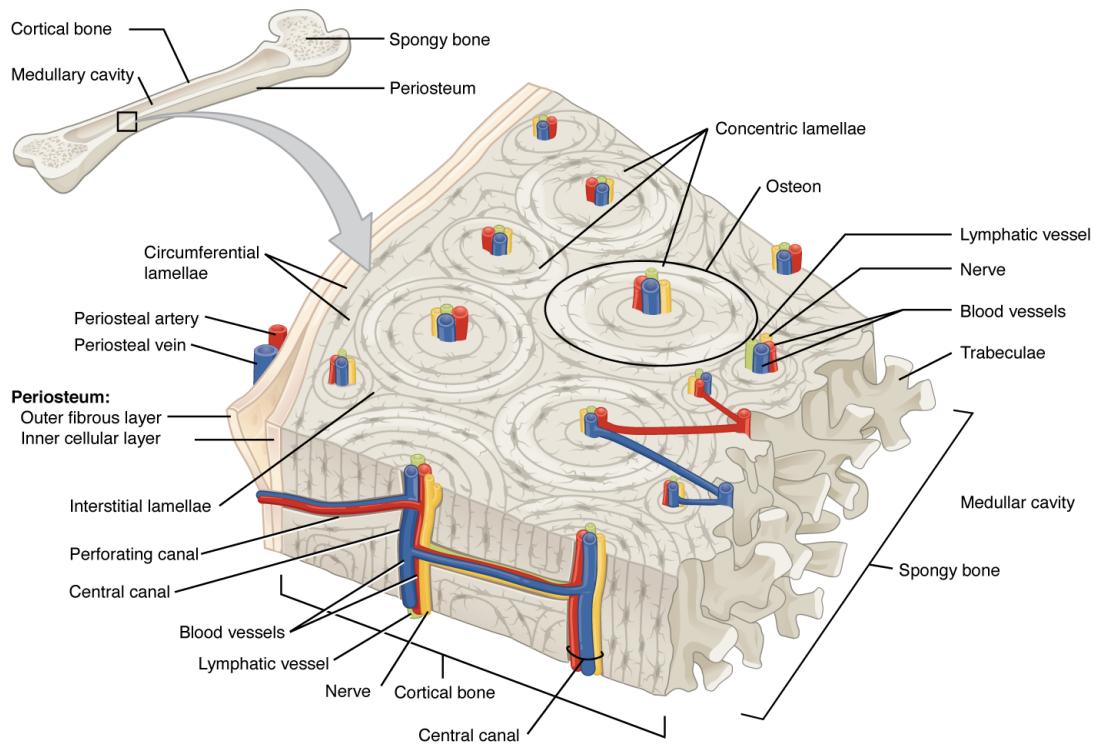


**Figure 2.3:** Diagram of compact bone. (Taken from [2])

Cortical bone, also known as compact bone, is described as a dense tissue most commonly located in the shafts of long bones. It contains blood vessels as well as the canaliculi surrounding osteocytes and their connecting cellular processes. [1]

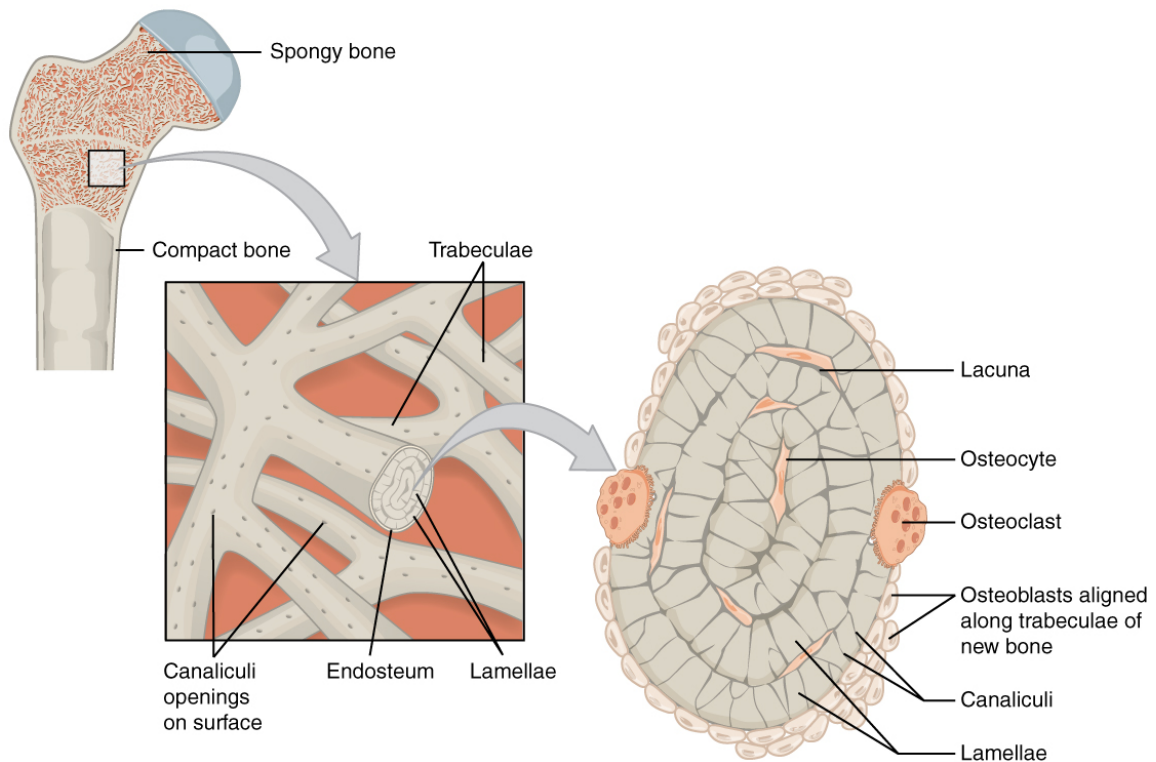


**Figure 2.4:** Diagram of trabecular bone. (Taken from [2])

Trabecular or *cancellous* bone is characterized by a complex network of thin plates and connecting struts, the *trabeculae*, surrounded by bone marrow. It is located at the ends of long bones, in the vertebrae or near joint surfaces. [1]

These two types of bone share a similar cellular and molecular composition but have fundamentally different functions and mechanical properties. [1]

## 2 Breast and Prostate Cancer Bone Metastasis

Metastasis is the first cause of death in breast and prostate cancer patients. It is defined as the process by which malignant cells leave the site of the primary tumour to spread to other tissues and organs. Between 65 and 70% of patients with metastatic breast or prostate cancer have metastasis to the bone, with a median survival rate of 3-5 years after diagnosis. This is due to the fact that, once they have spread to the bone, these cancers can rarely be cured. Instead, they are associated with different morbidities, also known as skeletal-related events, including pain, increased risks of fracture, hypercalcaemia or spinal compression. [3][4][30]

The high death rates induced by bone metastasis have motivated a large number of studies aiming at deepening our knowledge of metastatic spread. Although the mechanisms underlying bone metastatic formation and progression are yet to be fully understood, progress has recently been made in that direction. Indeed, they namely enabled the simplification of the metastasis phenomenon in a sequence of successive steps, which include *colonization*, *dormancy*, *reactivation and development*, and *reconstruction*. The overall process of bone metastatic invasion by cancer cells is summarized in FIGURE 2.5. [30]

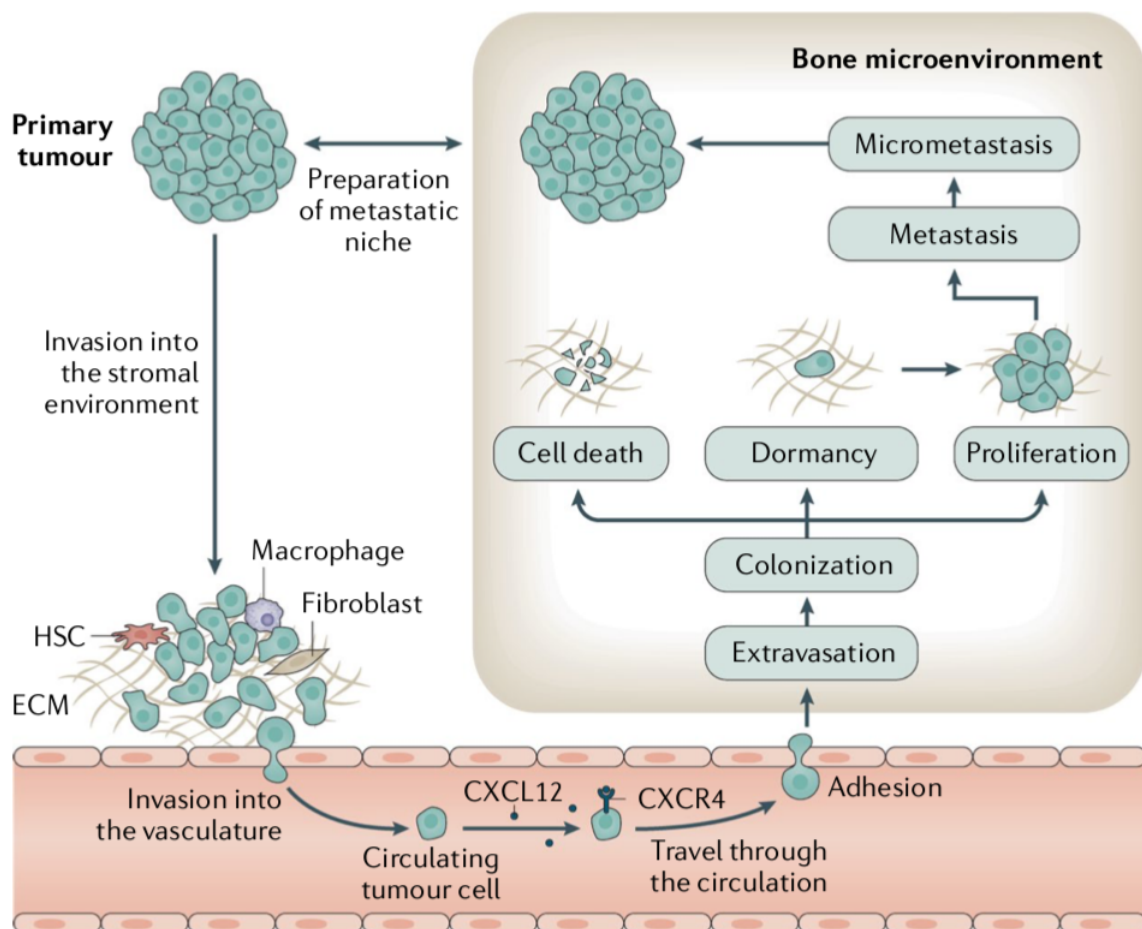


**Figure 2.5:** Metastatic invasion of cancer cells to the bone. (Taken from [3])

## 2.1 Colonization

Colonization can be defined as the entry of the bone marrow compartment by circulating cancer cells. [30]

In general, bones rich in red marrow and trabecular bone, such as the vertebrae or the ribs, are preferential targets for metastasis. The reason explaining this selectivity is still unknown, but it is assumed that the presence of trabecular bone, higher rates of bone turnover, and vascularization all contribute to the seeding of tumor cells. Not only does bone marrow enclose an important vasculature, but also the discontinuity in the bone endothelium makes this organ specially permissive to disseminated tumor cells. [31][4]

From a molecular point of view, C-X-C motif chemokine 12 (CXCL12), also known as the stromal-Derived Factor (SDF-1), is one of the key factors mediating cancer cell homing to bone. It has been shown that this molecule, produced by bone marrow stromal Cells (BMSCs) and osteoblasts, enhances the transendothelial migration of C-X-C chemokine receptor type 4 (CXCR4) expressing cancer cells, the CXCL12 receptor, and plays a crucial role in the homing and maintenance of a CXCR4-expressing hematopoietic stem cells (HSCs) niche. Indeed, this niche is the site where the cancer metastasis first occurs and cancer cells are clearly in competition with HSCs to occupy it. [30]

Though CXCL12 is an important mediator in cancer homing to bone, tumor cells use a myriad of other molecules. As illustrated on FIGURE 2.6, breast cancer cells in particular rely on the binding of different combinations of integrins with the bone's bone sialoprotein (BSP), fibronectin or osteopontin (OPN) and also rely on the association RANK-RANKL or different adhesion molecules, including E- and N-cadherin. [4]

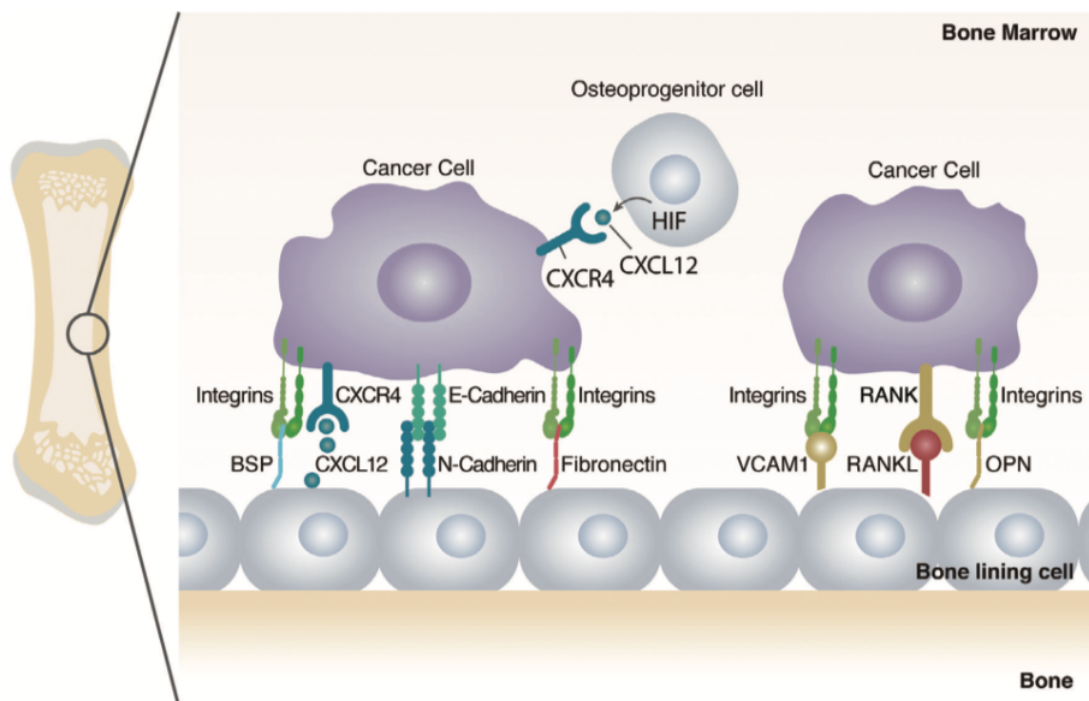


**Figure 2.6:** Interactions supporting breast cancer cell bone homing. (Taken from [4])

## 2.2 Dormancy

Dormancy can be defined as the phase in which cancer cells that have entered the bone compartment adapt to the bone microenvironment and remain dormant for many years. This state of dormancy is namely the explanation why the disease can resist treatment and reappear after asymptomatic periods up to decades. [4][30]

The dormant state of disseminated tumor cells is under the control of different mechanisms that can be cell-autonomous or between components of bone and tumoral stroma, which are under intensive study but still not fully understood. For example, the innate and adaptive immune systems are key regulators of dormancy but other exogenous factors such as hypoxia or bone morphogenic proteins (BMPs) are thought to intervene. Strategies aimed at eliminating the dormant cancer cell are an active field of study as they are thought to represent great opportunities for reducing cancer relapse. [3][4]

## 2.3 Reactivation and Development

During the reactivation and development step, cancer cells go from the latency state to a state of active proliferation. As one can expect, it is crucial for the metastatic process that dormant cancer cells reactivate. [30]

This reactivation is a complex process that is controlled by different mechanisms that are not fully understood. They include interactions between the cancerous cells and different non-tumorous processes, namely angiogenic factors, hematopoietic stem cells or osteogenic niches. The exit of dormancy can also be favored by genetic or epigenetic changes, but they are not fully characterized. [30]

## 2.4 Reconstruction

The last and final step of the metastatic formation process is reconstruction. This phase is characterized by a change of the original structure and function of bone, initiated by cancer cells. [3]

Different pathological factors can disrupt the normal bone resorption/bone formation balance between osteoclasts and osteoblasts. There actually exist two phenotypes of bone metastases : *osteolytic*, typically observed in breast cancers, and *osteoblastic*, typically observed in prostate cancers. This distinction is based on the characteristic appearance of lesions in the bone, with respectively either a predominance of lysis or of sclerosis. [3][30]

As their name implies, osteolytic bone metastases enhance osteolysis and therefore result in bone destruction. This namely happens by the release of osteolytic factors that activate bone-resorbing osteoclasts. Examples of osteolytic factors include molecules such as the parathyroid hormone-related protein (PTHrP), interleukin (IL)-11, IL-6, vascular endothelial growth factor (VEGF) and *Jagged 1*. The first four activate osteoblasts, which, as a result, release soluble RANKL and inactivate OPG. This leads to the binding of RANKL with the RANK receptor on osteoclasts' membrane. Activated as a result of ligand binding, multinucleated osteoclasts get attached to the bone surface and resorb the bone matrix, thereby releasing different growth factors. This stimulates tumor growth,

leading to the production of additional osteolytic and osteoblastic factors and resulting in a vicious cycle of bone metastasis. Jagged 1 promotes bone resorption by binding to monocytes, which promotes osteoclast precursors fusion. [3][4]

On the other hand, osteoblastic bone metastases are characterized by the production of osteoblastic factors, enhancing osteoblast proliferation and differentiation, such as Endothelin 1, growth differentiation factor 15 (GDF15) and BMPs. Although osteoblast precursors are thought to be the source of tumor-induced bone formation, tumour osteomimicry, defined as "*the ability of cancer cells or associated microenvironment cells to express bone-specific proteins which support cancer cell growth and survival in the bone microenvironment*", and tumor endothelial-to-osteoblast conversion have also been shown to play a role. The newly deposited bone is woven bone, whose collagen fibers are arranged in an irregular random network. [3][30] Note that osteoblastic bone metastases also present osteolysis, common to all tumour types. [3]



### 3 Models of Bone Metastasis

The deadliness of breast and cancer metastatic cells comes from their resistance to traditional cancer therapeutic strategies. Specifically targeting steps of the metastasis formation process thus appears as the most effective way of addressing this issue. However, as described in the previous section, bone metastasis occurrence and progression involve a wide variety of molecular pathways that, for most, are still poorly understood. Nonetheless, it clearly appears that they would not take place without cellular and non-cellular components of the bone microenvironment. This lack of characterization represents the major obstacle in the development of treatments that could potentially cure bone metastasis. Filling this gap would require the use of *in vitro* models that can faithfully mimic the different interactions between breast and cancer cells and the bone microenvironment. [28][32][33]

The two types of models historically used to evaluate therapeutic agents and anti-cancer drugs - simple cultures of cell monolayers and animal models - do not sufficiently replicate the bone microenvironment. This is the reason why only 5% of the many drugs with promising results in these models showed actual anti-tumor activity during clinical trials. [28][32][33]

Monolayers of cultured cancer cells have led to significant breakthroughs in cancer research. However, they have several important drawbacks, therefore limiting their potential contributions to the field. Indeed, although they are easily maintained with little resource consumption and great expansion possibilities, they are known to quickly lose their native features *in vitro* due to their lack of physiological extracellular matrix. Therefore, they cannot recapitulate realistic intercellular, intracellular and cell-matrix interactions. [28][34][33]

Animal cancer models have mainly been used to monitor the effectiveness and efficacy of new potential treatments. Animal models have important drawbacks : their generation is time consuming and costly and they do not faithfully translate pathogenic processes in patients. For example, studies have shown that, contrary to human bone, bone of genetically engineered mouse would not allow for prostate cancer cell invasion. Furthermore, the use of animals in research always raises ethical questions since it often requires inflicting suffering and pain to a living being, which might result in its death. [28][34][33]

In recent years, tissue engineered alternatives have gained in popularity because they provide a predictive, inexpensive and low time-consuming alternative to 2D *in vitro* cultures and *in vivo* animal models by culturing cells on 3D substrates, also called scaffolds, that try to replicate the microenvironment. [28][34]

#### 3.1 Tissue-Engineered Models

The goal of tissue engineered models is to mimic the *in vivo* environment as closely as possible. To do so, different materials and processing techniques have been explored over the years. Depending on the specific type of cancer and the mechanisms under study, a

material will be selected for its specific mechanical and chemical properties. [28][34]

### 3.1.1 Scaffold material

In the particular case of bone metastasis, tissue engineered models aim at faithfully recreating the bone microenvironment, that is a stiff matrix with specific local proteins and cells. Therefore, different materials have been investigated in order to reproduce the particular properties of the bone matrix. [34]

The first one is collagen type 1, which is the primary organic component of bone. However, because of its poor mechanical properties, collagen type 1 often requires to be crosslinked and used in combination with other materials, such as hydroxyapatite (the main inorganic component of bone). Thus 3D collagen-based scaffolds are usually prepared by first forming a slurry, made of blended collagen in which other components are incorporated, that is then lyophilized and crosslinked. The properties of the scaffolds, such as their microstructure and their mechanical properties, can be tuned in function of the crosslinking method and the concentration of the slurries. [34]

Another popular choice in tissue engineering is chitosan, a common polysaccharide derived from chitin found in shells. It is an interesting material because it is cheap, scalable, anti-microbial and biocompatible. Once again, depending on the manufacturing and processing conditions, chitosan-based models can be given specific properties. For example, by using physical, coordinated or chemical crosslinking, they can get the form of hydrogels or of porous sponges if mixed with other materials (such as alginate) and subsequently lyophilized. [34]

Tissue engineered scaffolds can also frequently be made of silk fibroin, a protein produced by silkworms and spiders. It presents an extreme toughness and a slow in vivo degradation rate. It is adapted to a wide variety of manufacturing techniques, such as casting, crosslinking, electrospinning, gas foaming and lyophilisation. [34]

However, using the materials described above also requires to shape them so that they accurately reproduce the complex architecture and mechanical properties of native bone matrix, which represents a major challenge, even using state-of-the-art manufacturing techniques. Therefore, this has led to the use of decellularized extracellular matrix (ECM). Besides the architectural and mechanical advantage, they also naturally enclose the different components of bone (e.g growth factors), which allows to mimic its microenvironment more closely. [34]

Besides these naturally occurring materials, synthetically derived materials have also been used successfully in tissue engineering. Their attractiveness comes from the fact that, in comparison to natural materials, they offer a lower batch-to-batch variability as well as a higher degree of controllability regarding the different components they might contain influencing cell behaviour, such as growth factors and other proteins. One of the most frequently used materials in scaffolds is poly( $\epsilon$ -caprolactone) (PCL). Since it has a low melting temperature, it is easily manipulated which makes it easily adjustable to specific needs of use. It has also been used successfully in combination

with other materials like calcium minerals such calcium phosphates and hydroxyapatite to better mimic bone microenvironment.

Other synthetic polymers, such as polyurethane, polystyrene or poly(lactic-co-glycolic acid), have also been used in 3D cancer models for the study of metastasis. [34]

### 3.1.2 Incorporating Growth Factors, Proteins or Minerals

Cell behavior is not only governed by the properties of the scaffold material such as its biodegradability or its density. It has been shown that adding elements such as growth factors, proteins or minerals into the models could enhance and guide the activity of the seeded cells. [34]

Among other examples, the incorporation of hydroxyapatite in 3D models has been shown to increase cell infiltration, adhesion and proliferation of both breast cancer cells and co-cultured cells like osteoblasts and human MSCs. [34]

### 3.1.3 Choice of co-cultured cells

The choice of co-cultured cells can also have an important impact on cancer cell behavior. Indeed, different cells (on identical scaffolds) will generate different culture environments namely through intercellular crosstalk and secretion of different growth factors and proteins.

For example, the co-culture of breast cancer cells with bone marrow cell lines led to an interruption in cell proliferation while the co-culture with bone marrow stromal cells led to a proliferation rate close to that of breast cancer monoculture. [34]

## 3.2 Current Challenges

Although tissue-engineered models have started to fill in the gap between 2D *in vitro* cultures and *in vivo* animal models, the field still needs to face major challenges. Among them is recapitulating metastasis features *in vitro* and doing so in a standardized and balanced way. [28][34]

There is therefore a real need for better bioengineered cancer models that are able to mimic the bone microenvironment. [28]

# Chapter 3

## Theoretical Bases

This chapter provides the key theoretical concepts and principles necessary to understand the work developed in this dissertation.

The first section is dedicated to an overview of *Image Registration* techniques while the second provides the reader with an introduction to basic deep learning (DL) architectures and objectives, with a focus on *Convolutional Neural Networks*. Finally, the third and last section presents the concept of *Color Deconvolution* of histological images.

### 1 Image Registration

Image registration is defined as : "*the process of spatially aligning two images of a scene so that corresponding points assume the same coordinates.*".[35] This process has a wide variety of applications, in areas ranging from art and astronomy to criminology and chemistry, and is particularly useful in biomedicine.[36] Indeed, image registration can be performed to overlay images for examination which may have been taken at different times, from different viewpoints or/and with different sensors (therefore having different modalities).[6]

In this dissertation, image registration is used to align serial hematoxylin and eosin (H&E) stained sections of the samples to create their respective 3D reconstructions.

#### 1.1 Generalities

Because of the wide range of applications requiring registration, it would not be possible to find a general registration method applicable to any image. However, most registration methods use the four following steps: [37]

1. *Feature Detection*: This consists in the manual or automated detection of distinctive objects in the image such as closed-boundary regions, contours, line intersections, etc. These elements are represented by their control points (CPs), or point representatives (centers of gravity, line endings, distinctive points).[37]
2. *Feature Matching*: Using different feature descriptors and similarity measures as well as spatial relationships among them, the correspondence between the features

detected in the moving image<sup>1</sup> and the ones detected in the reference image is made.[37]

3. *Transform Model Estimation*: Mapping functions are used to align the sensed image with the reference image. The functions parameters are estimated with the help of the established feature correspondence.[37]
4. *Image Resampling and Transformation*: By means of the mapping function, the sensed image is transformed and its values for non-integer coordinates are computed using an adequate interpolation technique.[37]

Although there exist different criteria to classify and differentiate image registration methods, the most commonly used one is the feature space image information.[5] Indeed, in current techniques, there exist mainly two types of approaches for feature understanding :

- *Area-based or Intensity-based methods*: In such methods, the feature detection step is merged with feature matching because no objects are actually detected. Instead, they use the raw voxels/pixels intensity, the intensity gradient or more generally, statistical information related to the voxel/pixel intensity of windows of predefined size or even of entire images. [37][5]
- *Feature-based methods*: These methods on the other hand use distinct and efficiently detectable structures in both images such as sets of points, edges, contours, graphs, surfaces and volumes. Therefore, they have a detection step. [37][5]

The differences between a typical intensity-based image registration algorithm and a typical feature-based one can be seen by comparing FIGURES 3.1 and 3.2 respectively.

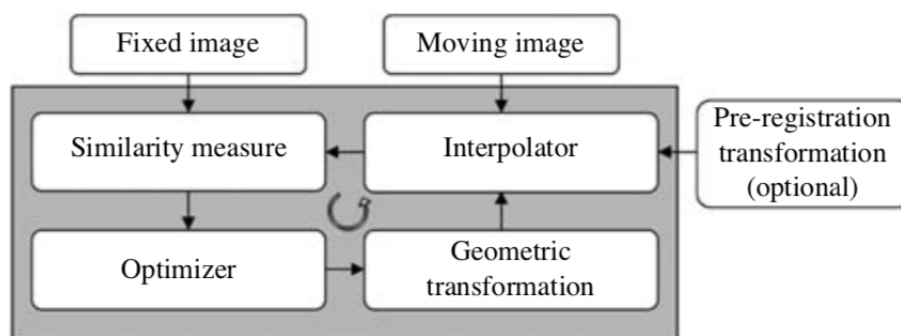


**Figure 3.1:** Diagram of typical algorithms used in intensity-based registration techniques. (Taken from [5])

<sup>1</sup>i.e the image to be registered

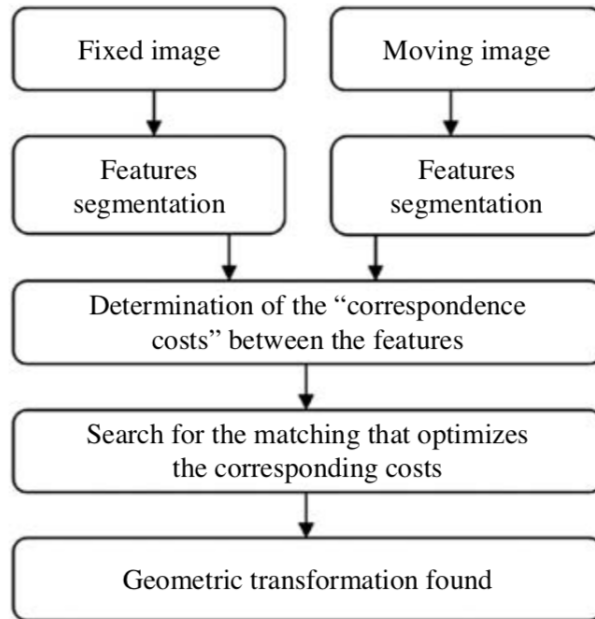


**Figure 3.2:** Diagram of typical feature-based registration algorithms. (Taken from [5])

Feature-based methods are particularly attractive in the case of images containing distinctive objects that are easily detectable. However, since most images used in biomedical applications are relatively poor in such details, area-based approaches are usually preferred. [6] Another interesting characteristic of area-based methods is that, unlike feature-based techniques, they show a certain robustness to slight content modification in the registration process although they also tend to be sensitive to noise present in the images. [38]

For the reasons described above, the approach that was chosen in this dissertation is an area-based one. Therefore, the remaining of this short review about image registration will focus on this type of techniques solely.

Nonetheless, let us note that another popular criteria to differentiate image registration techniques exists: the transformation domain, which can be global or local (also known as elastic). The parameters of the mapping function are defined for the whole image in the case of global methods while they are defined for small regions of the image in local methods. (FIGURE 3.3) [5][6]

## 1.2 Intensity-based Image Registration

As illustrated in FIGURE 3.1, the main idea behind an intensity-based registration method is to, via an iterative process, search for the optimal geometric transformation between the moving and the reference images. This optimal geometric transformation is defined as the one that minimises or maximises a similarity measure, related to voxel intensity, between the two images. The role of the optimizer is to define the search strategy while the goal of the interpolator is to resample the voxel intensity into the new coordinate system via the use of the geometric transformation. To obtain a faster convergence of

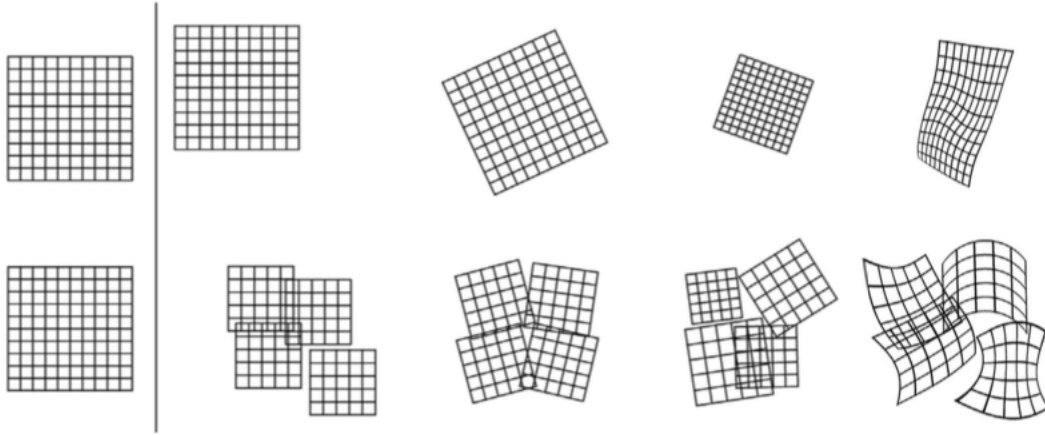


**Figure 3.3:** Global (top line) versus local (bottom line) registration model. (Taken from [6])

the optimizer and decrease the risk of converging to a local optimum, one can use a pre-registration transformation as an initial solution for the registration algorithm. It makes the similarity measure of the moving image closer to the one of the fixed image. [5]

### 1.2.1 Geometric Transformation

As its name implies, a geometric transformation is used to transform the geometry of the moving image to that of the reference image in order to spatially align them.[35] In other words, given the coordinates of  $n$  corresponding points in the two images:

$$\{(x_i, y_i), (X_i, Y_i) : i = 1, \dots, n\}, \quad (1.1)$$

a geometric transformation is a function with components  $f_x$  and  $f_y$  such that:

$$X_i \approx f_x(x_i, y_i), \quad i = 1, \dots, n \quad (1.2)$$

$$Y_i \approx f_y(x_i, y_i), \quad (1.3)$$

where  $f_x$  is a single-valued function that approximates 3-D points:

$$\{(x_i, y_i, X_i) : i = 1, \dots, n\}, \quad (1.4)$$

and  $f_y$  is also a single-valued function that approximates 3D-points:

$$\{(x_i, y_i, Y_i) : i = 1, \dots, n\}, \quad (1.5)$$

Each component of a transformation function therefore represents the coordinate of CPs in the reference image and the  $X$ - or the  $Y$ -component of these CPs in the moving image. [35]

Usually, geometric transformations can be classified in *rigid* and *non-rigid* classes. The rigid transformation is the simplest one. The non-rigid transformations include the similarity transformation (defined by a translation, a rotation and uniform scaling), the affine transformation (translation, rotation, scaling and shear), the projective and the

curved transformations. [5]

In this work, the geometric transformation that was used is a rigid one. The rigid or *euclidian transformation* corresponds to a translation and a rotation of the moving image with respect to the reference image. It therefore preserves the distance between points as well as the angles between lines.

Mathematically, this transformation can be written as:

$$X = x \cos \theta - y \sin \theta + h, \quad (1.6)$$

$$Y = x \sin \theta + y \cos \theta + k \quad (1.7)$$

where the parameter  $\theta$  measures the difference in orientation between the moving and the reference image in the counter-clockwise direction and the parameters  $h$  and  $k$  account for the translation of the former image with respect to the latter in the  $x$  and  $y$  directions respectively. [35]

In matrix notation, this becomes :

$$\begin{pmatrix} X \\ Y \\ 1 \end{pmatrix} = \begin{pmatrix} 1 & 0 & h \\ 0 & 1 & k \\ 0 & 0 & 1 \end{pmatrix} \begin{pmatrix} \cos \theta & -\sin \theta & 0 \\ \sin \theta & \cos \theta & 0 \\ 0 & 0 & 1 \end{pmatrix} \begin{pmatrix} x \\ y \\ 1 \end{pmatrix} \quad (1.8)$$

or :

$$\mathbf{P} = \mathbf{TRp} \quad (1.9)$$

### 1.2.2 Interpolation

Once a geometric transformation has been used to map a point from one space into another, it is usually allocated a non-grid position. In such a case, an interpolation method is used to estimate the intensity of the image at this new position. [5]

There exist different possible options for interpolation and the chosen method can have a significant impact on the accuracy and the speed of the registration process. A typical way of increasing the registration speed is to use a simple interpolation algorithm in the optimization step and then a more complex one to obtain the final registered image. [5]

### 1.2.3 Similarity Measure

There exist different intensity-based similarity measures, but the most commonly used ones rely on the computation of intensity differences, intensity cross-correlation or on information theory. [5]

In this dissertation, the similarity measure that was used is the cross-correlation. Its use relies on the assumptions that the intensities of corresponding structures in both images are linked by a linear relation and that the intensities from pixel to pixel are independent and stationary. Therefore, the better the registration, the larger the cross-correlation will



be. [5]

Among others, a method that has gained interest in recent years is the use of the Radon Transform (RT). Indeed, it is namely possible to find the rotational and translational alignment between two images through the use of the cross-correlation of their RT. [39]

However, before going into details about the latter procedure, used in this work, let us first introduce the RT and some of its properties.

### 1.2.3.1 Radon Transform

Let us consider, as it is shown in FIGURE 1.10, a straight line  $L$  in the x-y plane whose perpendicular distance to the origin is given by  $p$  and that is at an angle  $\phi$  with respect to the  $y$  axis, as well as an increment of length  $ds$  along that line.

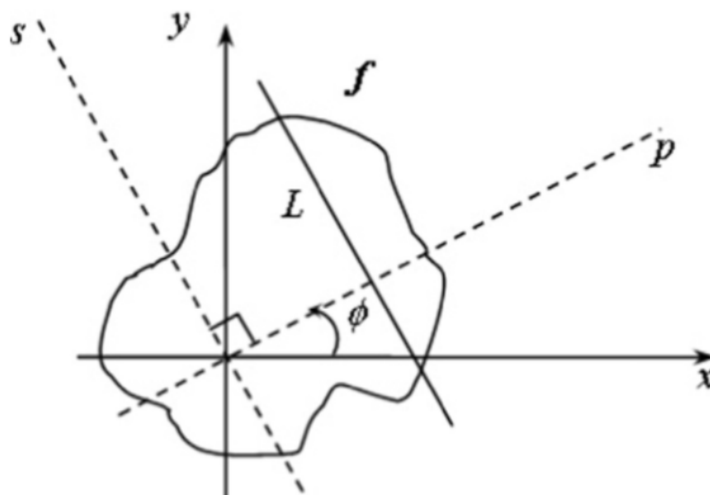


**Figure 3.4:** Definition of the Radon transform. (Taken from [7])

The RT of a real-valued function  $f$ , noted  $R_f$ , is determined by computing the line integral of  $f$  along the line  $L$  in the x-y plane:

$$R_f(p, \phi) = \int_L f(x, y) ds \quad (1.10)$$

where  $\phi \in [0, \pi]$  and  $p \in \mathbb{R}$ .

The equation of  $L$  is:

$$p = x \cos \phi - y \sin \phi \quad (1.11)$$

Therefore, if the  $s$  and  $p$  axes are chosen such that the former is parallel to  $L$ , one can express the  $x$  and  $y$  axis as:

$$x = p \cos \phi - s \sin \phi \quad (1.12)$$

$$y = p \sin \phi + s \cos \phi \quad (1.13)$$

By substituting these two expressions in EQUATION 1.10,  $R_f$  can be written as:

$$R_f(p, \phi) = \int_{-\infty}^{+\infty} f(p \cos \phi - s \sin \phi, p \sin \phi + s \cos \phi) ds \quad (1.14)$$

Determining the RT of  $f$  at any point  $(p, \phi)$  therefore requires to integrate  $f$  for all lines  $L_{p,\phi}$  in the x-y plane. [7][40]

The RT presents interesting properties, namely:

- The RT of a function  $h_r$  rotated by an angle  $\theta$  with respect to a reference function  $f$  is given by :

$$h_r(x, y) = f(x \cos \theta + y \sin \theta, -x \sin \theta + y \cos \theta) \Rightarrow R_{h_r}(p, \phi) = R_f(p, \phi - \theta) \quad (1.15)$$

- The RT of a function  $h_t$  translated by a vector  $\mathbf{u} = (x_0, y_0)$  is given by :

$$h_t(x, y) = f(x - x_0, y - y_0) \Rightarrow R_{h_t}(p, \phi) = R_f(p - x_0 \cos \phi - y_0 \sin \phi, \phi) \quad (1.16)$$

### 1.2.3.2 Problem Statement and Implementation

The rotational and translational parameters necessary to align two images can be found through the computation of the cross-correlation of their RT. [39]

Let us consider a moving image  $g$  in the x-y plane that is the result of a rigid transformation, composed of a rotation of angle  $\theta_0 \in [0, 2\pi]$  and a translation of vector  $(h_0, l_0) \in \mathbb{R}^2$ , applied to a reference image  $f$ . The following relation holds:

$$g(x, y) = f(x \cos \theta_0 + y \sin \theta_0 - h_0, -x \sin \theta_0 + y \cos \theta_0 - l_0) \quad (1.17)$$

Let  $R_f(p, \phi)$  be the RT of the reference image and  $R_g(p, \phi)$  be the one of the image to be aligned. The cross-correlation function of these two RT:

$$c(\theta, h, l) = \int \int \tilde{R}_f(p, \phi) \cdot R_g(p - h \sin \phi - l \cos \phi, \phi + \theta) dp d\phi \quad (1.18)$$

reaches its maximum value in  $(\theta_0, h_0, l_0)$ . [39]

The problem of aligning two images  $f$  and  $g$  will therefore consist in finding the values  $(\theta_0, h_0, l_0)$  that maximize the cross-correlation of their respective RT  $R_f$  and  $R_g$ . In mathematical notation, this writes:

$$(\theta_0, h_0, l_0) = \underset{(\theta, h, l)}{\operatorname{argmin}} c(\theta, h, l) \quad (1.19)$$

However, the last few relations hold for continuous functions. In practice, the intensities of the two images to be aligned are not continuous functions, they are discrete and so are their RT.

In this dissertation, the images RTs were computed using the Matlab function `radon(I, theta)`, which returns a matrix whose columns are the RTs of the grayscale image  $I$  for each of the angles specified by `theta`. The RTs are obtained by projecting the image intensity

along a radial line at each of these angles. The implemented algorithm computes the RT of an image as the sum of each individual pixel's RT. It works by first dividing the pixels in the image into four subpixels that are each projected separately, as shown in FIGURE 3.5. There are two ways in which the contribution of a subpixel can be taken into account:

1. If its projection arrives at the center of a bin, this bin gets the full value of the subpixel.
2. In the case where the projection hits the frontier between two bins, its value will be split uniformly between the bins. [8]

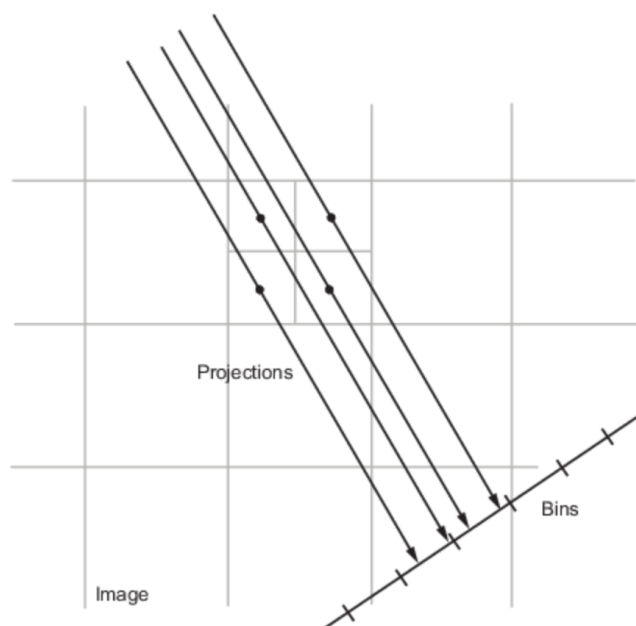


**Figure 3.5:** Computation of the Radon Transform by the `radon` built-in Matlab function. (Taken from [8])

The cross-correlation of the two RT matrices is then computed using another Matlab built-in function, `xcorr2` which outputs the cross-correlation of two matrices. For a matrix  $X$  of size  $M \times N$  and another matrix  $H$  of size  $P \times Q$ , their 2D cross-correlation is a matrix  $C$  of size  $M + P - 1 \times N + Q - 1$  whose elements are given by:

$$C(k, l) = \sum_{m=0}^{M-1} \sum_{n=0}^{N-1} X(m, n) \bar{H}(m - k, n - l), \quad \begin{array}{l} -(P - 1) \leq k \leq M - 1 \\ -(Q - 1) \leq l \leq N - 1 \end{array} \quad (1.20)$$

where  $\bar{H}$  is the complex conjugation of  $H$ .

As it can be seen the row and column indices of the matrix  $C(k, l)$  can be either negative or positive. A row index that is negative corresponds to an upward shift of the rows of  $H$  while a row index that is positive corresponds to a downward shift. On the other hand, a negative and positive column index will respectively correspond to a leftward or a rightward shift of the columns of  $H$ . [41]

#### 1.2.4 Optimisation

The goal of a registration process is to find the transformation that correctly aligns the input images. As it has been explained in the previous section, this transformation is assumed to be the optimum of the  $n$ -dimensional function that is the similarity measure, where  $n$  represents the number of degrees of freedom of the transformation. An optimisation algorithm is therefore used to find the maximum or minimum value of the selected similarity measure.

Different optimization algorithms have been employed in the context of medical image registration, among which: the Powell's method, the downhill simplex method, the Gauss-Newton, the Levenberg-Marquardt or the gradient ascent/descent. [5]

## 2 Deep Learning Classification

The expression machine learning is used to designate the ability of an artificial intelligence system to extract patterns from raw data in order to acquire its own knowledge. It allows computers to make decisions that appear subjective using knowledge of the real world. [42]

Machine-learning technologies therefore have an important number of applications, ranging from identifying objects in images and transcribing speech into text to content filtering on social networks and recommending products to customers on e-commerce websites. [43] They have also been increasingly used in the context of medical image analysis in different areas such as segmentation, detection of abnormalities, classification of diseases or computer-aided diagnosis. [44]

One of the major drawbacks of conventional machine-learning technologies is that their ability to process natural data in their raw form is limited. They are highly sensitive to the representation of the data they are given. This implies that most machine-learning systems cannot detect or classify patterns in the input without the careful design of a feature extractor that is able to transform the raw data into a suitable feature vector. The problem is that the design of this feature extractor often requires extensive engineering and domain expertise. [42][43]

To overcome this limitation, representation learning methods were introduced and developed. They are defined as a set of methods that can automatically find the representations required for detection or classification from the raw data that they are fed. Among representation-learning techniques, DL methods obtain multiple levels of representation by combining different layers of non-linear modules that each transform the representation at one level into a representation at a higher, slightly more abstract level. If enough layers are used, very complex functions can be learned. [43][45]

Most DL algorithms are in fact artificial neural networks (ANN). Their name comes from the fact that, since their functioning is inspired by the one of biological neurons, they make use of a simplified neuronal model. [42]

### 2.1 One Neuron Perceptron Model

A simplified version of the structure of a neuron can be observed in FIGURE 3.6. This cell can be described with four main parts. First, an important number of dendrites, that convey the electrical signals entering the cell from other neurons in its vicinity. Secondly, a cell body, also called the soma, which processes the information. Thirdly, a large axon that transmits the neuron response to the stimulation it has received and finally, an important number of synapses formed between the ends of an axon and a dendrite. [9]

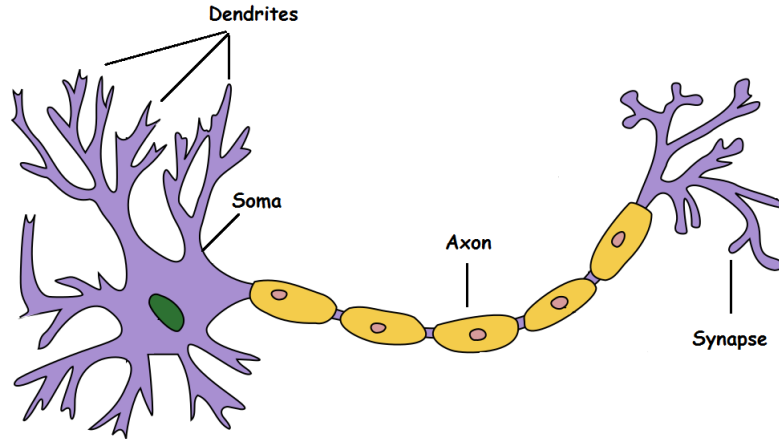


**Figure 3.6:** Simplified structure of a neuron. (Taken from [9])

In this simplified, and mostly biologically inaccurate, representation of the neuron, the cell functioning can be described according to three main principles:

1. it is either fully activated (i.e an action potential will propagate down the axon) if the stimulation coming from the other neurons is above a certain threshold otherwise, it is not activated at all.
2. it is under the cumulative influence of the other neurons connected to its dendrites.
3. each of the synaptic gaps may have more or less of an influence on its stimulation.

By following these three principles, one can build a mathematical model of a single neuron, also known as the *one neuron perceptron model*. [11] The graphical representation of such a model can be seen on FIGURE 3.7.

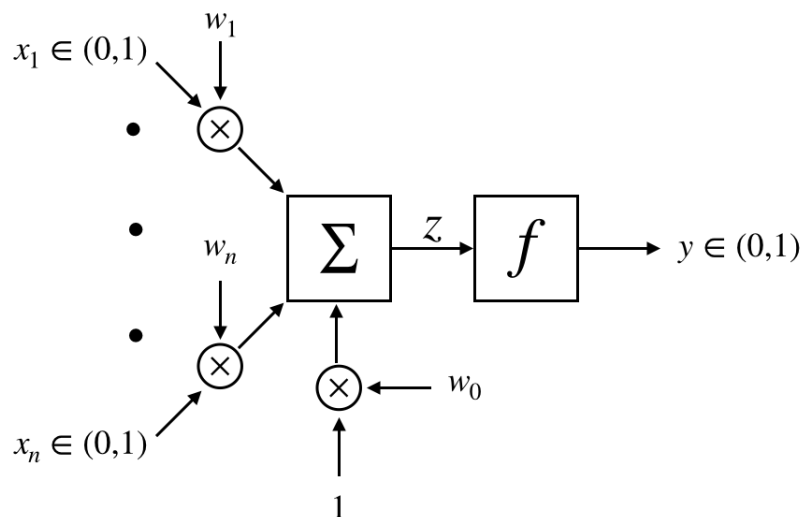


**Figure 3.7:** The one neuron perceptron model. (Adapted from [10] and [11])

The respective contributions of the  $n$  neurons connected to the main neuron's dendrites are represented by the  $n$  binary input features  $x_1, \dots, x_n$ . They are binary since it

is assumed that the surrounding neurons either send a signal or they do not. On the other hand, each input  $x_i$  with  $i = 0, \dots, n$  is also multiplied by its corresponding weight  $w_i$ , used to model the synaptic gaps between the axons and the dendrites. The weighted contributions of the different inputs are then summed. This gives:

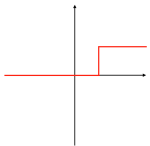
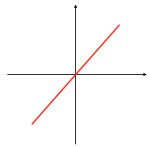
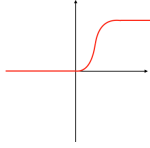
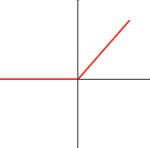
$$z = \sum_{i=0}^n w_i x_i \quad (2.1)$$

where  $x_0 = 1$  and  $w_0$  is the threshold or bias.

Finally, the binary output  $y$  is obtained by applying an activation function (also called a transfer function) to the weighted input sum  $z$ :

$$y = f(z) \quad (2.2)$$

This activation function can take various forms. Common examples can be found in TABLE 3.1.[10][12]

Activation function	Equation	2D graph
Unit step (Heaviside)	$f(z) = \begin{cases} 1 & \text{if } z \geq 0 \\ 0 & \text{if } z < 0 \end{cases}$	
Linear	$f(z) = z$	
Logistic (sigmoid)	$f(z) = \frac{1}{1+e^{-z}}$	
Rectified Linear Unit (ReLU)	$f(z) = \max(0, z)$	

**Table 3.1:** Examples of activation functions. (Adapted from [11])

By learning the appropriate weight vector and choosing the right activation function,

one neuron perceptron models are therefore able to approximate a desired function, just as other machine learning algorithms.[10] However, except for the fact that they can handle data in an online fashion, these models are actually not much more expressive than linear ones. Indeed, they can only learn linearly separable functions and are therefore not able to predict very complex non-linear functions. [11][12]

## 2.2 Multilayer Perceptron

ANN were introduced with the aim of potentially approximate more complex non-linear parametric models and to do so, they make use of several interconnected neurons. The most commonly used ANN structure is the multilayer perceptron (MLP), which is a feedforward neural network with different layers. An example of MLP is shown in FIGURE 3.8. [12]

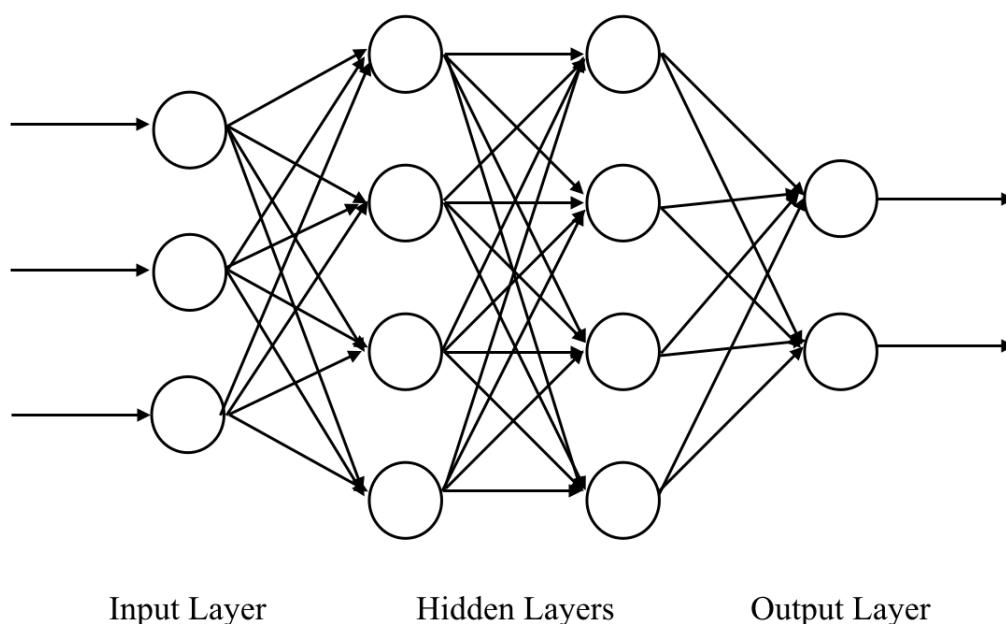


**Figure 3.8:** Example of a MLP with 3 inputs, 2 hidden layers of 4 neurons each and 2 outputs. (Adapted from [12])

An MLP is composed of an input layer (having as many neurons as there are inputs), a certain number of hidden layers as well as an output layer (with as many neurons as there are outputs). In the MLP, each neuron in a layer is fully connected to the neurons in the next. These models are qualified as feedforward because the information flows from the input layers, through all the hidden layers, to reach the output layer. There are no feedback connections where the model uses its own outputs. Even though each connection has its own weight, all neurons in a layer share the same activation function. Therefore, each layer can be seen as an ensemble of units working in parallel representing a vector-to-scalar function or as a single vector-to-vector function. With the latter representation in mind, a function is associated to each layer and the overall network can be seen as a



composition of these functions, many of which are non-linear. As it was originally aimed, this allows to form much more complex non-linear functions. [12][42][43] Usually, a sigmoid is used for the hidden layers while a linear or sigmoid function is used for the output layer, depending on the application. [11]

## 2.3 Convolutional Neural Networks

The convolutional neural network (CNN) architecture was first introduced by Lecun *et al.* in [46]. These networks are biologically-inspired<sup>2</sup> variants of MLP and were developed as a way to efficiently process data coming in the form of multiple arrays, in particular colored images composed of three 2D arrays containing the pixel intensities in each color channel. [43][44]

One of the main applications of CNNs is semantic segmentation. It can be defined conceptually as recognizing what is in an image at the pixel level or, in other words, as the process of attributing a class label to each pixel in a particular image. Contrarily to instance segmentation, semantic segmentation will attribute the same label to different occurring instances of an object. [48][49]

This is precisely for this type of applications that a CNN is employed in this work. Indeed, it identifies and labels different types of tissues on scanned H&E histological slides without the use of additional stains.

Though other neural networks can be very helpful for many applications, CNN were initially developed because their different layers are fully connected between each other which makes them difficult to scale to full images. In the case of an image of size  $200 \times 200 \times 3$  for example, each neuron would have  $200 \times 200 \times 3$  weights. Since neural networks have several layers themselves made up of several neurons, this would necessarily lead to a huge number of parameters which is a clear waste of resources and which could quickly lead to overfitting. [13]

### 2.3.1 Architecture Overview

A CNN transforms an original image from its original pixel values to class scores through the use of a sequence of layers. Each of them transforms a volume of neuron activations to another through the use of a differentiable function. [13]

---

<sup>2</sup>from the visual cortex of animals [47]

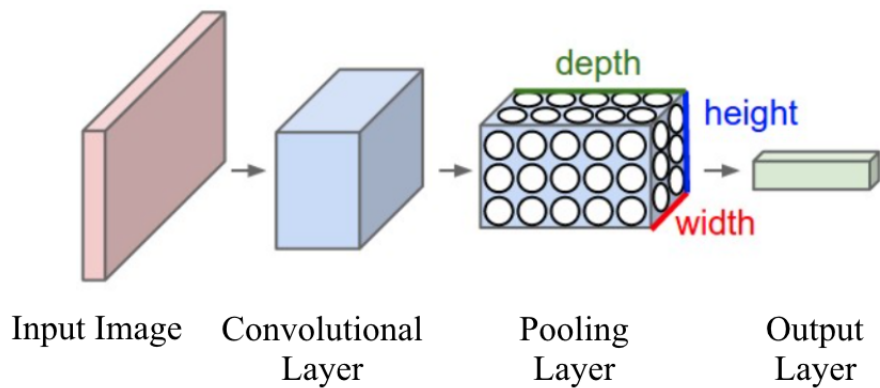


**Figure 3.9:** Simple CNN architecture. (Adapted from [13])

A simple CNN for image classification typically has the following architecture (FIGURE 3.9):

- an *input layer* holding the red green blue (RGB) image (*e.g* a volume of size  $32 \times 32 \times 3$  for a CIFAR-10 image)
- a *convolutional layer* computing the output of a series of neurons connected to specific and limited regions in the input volume (*e.g* in the case of the CIFAR-10 image and if we decide to use 12 filters, it will result in a  $32 \times 32 \times 12$  volume)
- a rectified linear unit (ReLU) layer applying an activation function, often  $\max(0, x)$ , and leaving the volume size unchanged
- a *pooling layer* performing a downsampling operation along the volume width and height (*e.g* resulting in a  $16 \times 16 \times 12$  volume)
- a *fully-connected layer* computing the class scores and in which each neuron is connected to all the neurons in the previous volume (*e.g* resulting in  $1 \times 1 \times 10$  volume if there are 10 classes such as for CIFAR-10 images)

To get a better sense of what each of these layers is doing precisely, let us now describe them in more details. [13]

### 2.3.1.1 Convolutional Layer

Its structure can be observed in FIGURE 3.10.

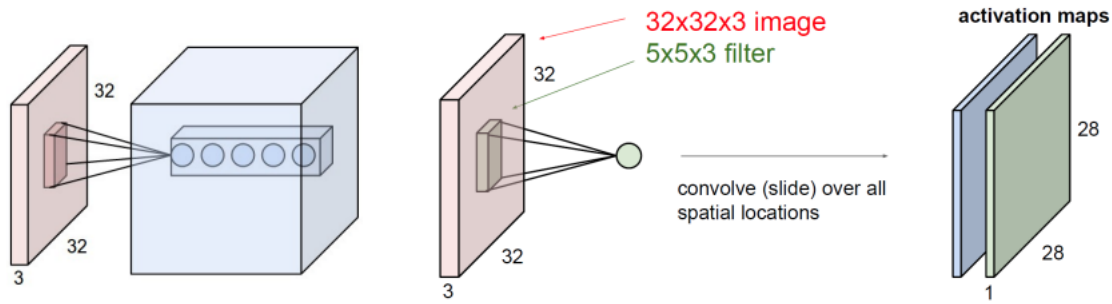


**Figure 3.10:** Convolutional layer and formation of activation maps. (Taken from [12])

In this layer, each neuron is connected to a local region of the input image, whose size is known as the receptive field of the neuron. Each neuron receives as an input a weighted sum of the pixels intensities (along the three colour channels) situated in its receptive field. The particularity of this layer is that all neurons at a same depth in the output volume have a receptive field of the same size and share the same weights. Therefore, this layer can be seen as *convolving* a filter (regrouping the weights of each pixel) across the width and height of the input image because it computes the dot product between the inputs and the entries of the filter at each position in the image. Passing such a filter on the image produces a 2D activation map that regroups the responses of the filter at any position. The *stride* of the filter is defined as the number of pixels that it jumps over in the input image. The higher the stride, the smaller the output volume is spatially. This convolving operation can be visualized more clearly on the example displayed in FIGURE 3.11. FIGURE 3.10 shows that the convolution layer can have multiple neurons along its depth that will all look at the same region in the image. However, these neurons do not use the same filter so they do not share the same weights.

The parameters of a convolutional layer therefore regroup a set of learnable filters. The network will learn filters that activate when they see some type of visual feature that will be simple for the first layers (like an edge or a blotch of some colors) and more complex for the higher ones (like an entire honeycomb for example). Thus, neurons at the same depth (but at different width and height) will detect the same feature at different locations in the image while neurons at the same width and height (but at different depths) will detect different features but at the same location. [13][12]

### 2.3.1.2 Non-Linear Layer

A non-linear layer is often placed directly after the convolutional layer to introduce non-linearity to the activation since the convolution operation is linear, which is far from being the case of images.

This layer can apply different types of non-linear activation functions. The most popular ones are listed in TABLE 3.1.

The ReLU is often preferred because it is more reliable and accelerates the convergence compared to other functions, such as the sigmoid. [50]

### 2.3.1.3 Pooling Layer

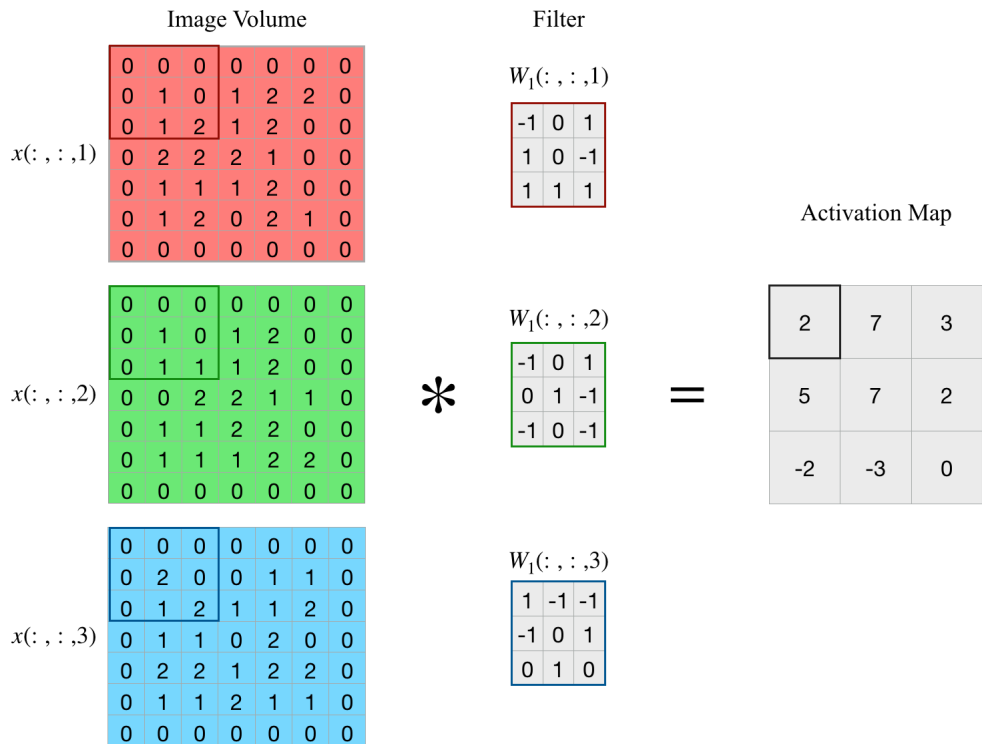


**Figure 3.11:** Implementation of the convolution operation as matrix multiplication (stride = 2). (Adapted from [13])

The main role of the pooling layer is to reduce the number of parameters and the computation time of the network, thereby controlling overfitting. It works independently on every depth slice of the input and reduces the spatial size of the representation by applying the max operation.

The most common form of pooling uses filters of size  $2 \times 2$  with a stride of 2 which therefore downsamples, along both width and height, every depth slice in the input, thus discarding 75% of the activations. An example of the application of such a filter can be observed in FIGURE 3.12.

Other pooling units have also been used historically, such as average pooling which was often employed. However, the max pooling operation has been shown to work better in practice so other operations have recently fallen out of favor. [13]

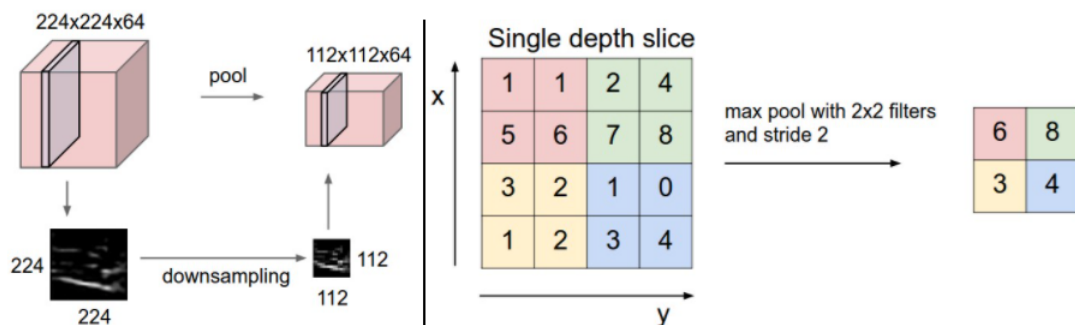


**Figure 3.12:** Functioning of the pooling layer. (Taken from [13])

### 2.3.1.4 Fully-connected Layer

In a CNN, fully-connected layers are usually located at the end (*i.e.* after the layers used for feature extraction) and are used for classification. Indeed, they output a vector of dimension  $k$ , where  $k$  is the number of classes that the network is able to predict, containing the probability of each class. [14]

In a fully-connected layer, each neuron is fully connected to the neurons in the previous layer, just as in other neural networks. [13]

An illustrative representation of a general CNN architecture for image classification can be found in FIGURE 3.13.

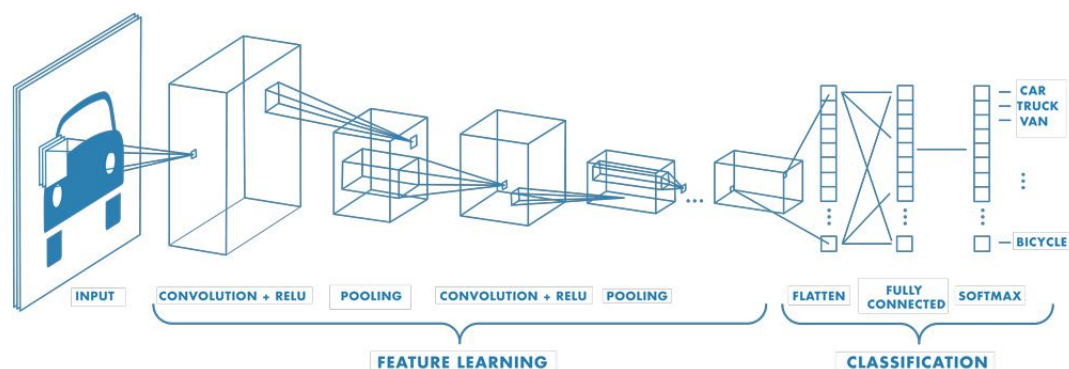


**Figure 3.13:** Illustrative representation of a CNN architecture for image classification. (Taken from [14])

## 2.3.2 Network Training

Training a network helps it tune its different weights in the aim of achieving better prediction accuracies.

### 2.3.2.1 Loss Function

In the context of *supervised learning*, as it is the case for CNNs, training is done by looking for the set of weights  $\mathcal{W}^*$  that minimizes the average *loss function*, also known as the *cost function* or the *objective*,  $\mathcal{L}$  over the training data.

The loss function helps assessing quantitatively the performances of the model by comparing the output vector predicted by the network  $\hat{\mathbf{y}}^{(i)} = \mathbf{g}(\mathbf{a}^{(i)}; \mathcal{W})$  for an example  $i$  with an attribute vector  $\mathbf{a}^{(i)}$  and the actual vector of values  $\mathbf{y}^{(i)}$  of this object, for all the examples in a *training set*. To get an improvement of the network's performances, the average cost function must decrease.

Mathematically, and for a training set with  $N$  examples, the problem of finding the optimal weights can be written as:

$$\mathcal{W}^* = \underset{\mathcal{W}}{\operatorname{argmin}} \quad \mathcal{L}(\mathcal{W}) = \underset{\mathcal{W}}{\operatorname{argmin}} \quad \frac{1}{N} \sum_{i=1}^N L(\hat{\mathbf{y}}^{(i)}, \mathbf{y}^{(i)}) \quad (2.3)$$

Different loss functions can be introduced depending on the learning problem. There exist two main loss functions subdivisions, corresponding to classifications and regressions

problems. For regression losses, the measure of performance that is most commonly used is the mean squared error (MSE) while for classification losses, the most commonly used are the *Cross Entropy* and the support vector machine (SVM) loss functions.

However, in classification problems with multiple classes such as the ones tackled by CNNs, Cross Entropy (also known as *log loss*) is often preferred. It measures performance by comparing the probability distribution outputted from the Softmax function with the true class label and takes the following mathematical expression:

$$\mathcal{L} = - \sum_{i=1}^N \sum_{j=1}^K t_{ij} \ln(\hat{y}_{ij}) \quad (2.4)$$

where  $N$  is the number of samples in the training set,  $K$  is the number of classes,  $t_{ij}$  takes the value 1 if  $j$  is the actual class of sample  $i$  and where  $\hat{y}_{ij}$  is the network's output probability distribution for the  $i$ th training example. [12][13][42][51]

### 2.3.2.2 Optimization Algorithm

Optimization algorithms are used to find the network's optimal weight values minimizing the loss function. Among the different algorithm options, the one that is mostly used in DL is stochastic gradient descent (SGD).

The first step of this method consists in carefully initializing the weights to a random and relatively small value. Indeed, the effects of the initialization choice on the training of the model can be considerable. Secondly, the direction in which the loss function will be reduced the most once the weights are changed is identified using a small batch of images in the training dataset, called a *mini-batch*. The weights are then perturbed by a small amount in that direction. To capture the correct directions in which to perturb the weights, the gradient of the loss function with respect to those weights is used. This leads to the following update rule:

$$\mathcal{W}_{(t+1)} = \mathcal{W}_{(t)} - \eta \frac{\partial \mathcal{L}(\mathcal{W}_{(t)})}{\partial \mathcal{W}_{(t)}} \quad (2.5)$$

where  $\eta$  is the learning rate. This parameter is presented as static in the update rule but can actually decrease when training progresses.

Once the weights have been updated, another mini-batch is selected and the process is repeated until the stopping criteria has been reached.

The stopping criteria can be that the loss has been sufficiently minimized but the loss on a *validation dataset* can also be used to stop iterating. Indeed, one can decide to end training when the validation loss has stopped improving or when the model starts showing signs of *overfitting* (*i.e* when the validation error curve starts to increase while the training error one continues to decrease).

Different variants of SGD have been developed, among which are : RMSprop, Adagrad, Adadelta and ADAM. [12][52]

In this dissertation, the optimization algorithm that was used is adaptive moment estimation (ADAM). The idea behind ADAM is to associate the definition of *Momentum* with

*Adaptive Learning Rates* in order to get a faster convergence. This algorithm uses moving averages of the gradient  $m_t$  and the squared gradient  $v_t$ , that are themselves estimates of the 1st and 2nd raw moment of the gradient. The moving averages are exponentially updated, with a decay rate controlled by the hyperparameters  $\beta_1$  and  $\beta_2 \in [0, 1]$ . For the parameters  $\mathcal{W}^{(t)}$  and a loss function  $\mathcal{L}^{(t)}$ , where  $t$  is used to designate the current iteration, ADAM's weight updating equations are given by:

$$\begin{cases} m_{(t+1)} \leftarrow \beta_1 * m_{(t)} + (1 - \beta_1) * \nabla L(\mathcal{W})_{(t)} \\ v_{(t+1)} \leftarrow \beta_2 * v_{(t)} + (1 - \beta_2) * (\nabla L(\mathcal{W})_{(t)})^2 \end{cases} \quad (2.6)$$

$$\begin{cases} \hat{m}_{(t+1)} = \frac{m_{(t+1)}}{(1 - \beta_1^{(t+1)})} \\ \hat{v}_{(t+1)} = \frac{v_{(t+1)}}{(1 - \beta_2^{(t+1)})} \end{cases} \quad (2.7)$$

$$\mathcal{W}_{(t+1)} \leftarrow \mathcal{W}_{(t)} - \eta * \frac{\hat{m}_{t+1}}{\sqrt{v_{(t+1)} + \epsilon}} \quad (2.8)$$

where  $\epsilon$  is small scalar parameter used to prevent dividing by zero. [53]

### 2.3.2.3 Hyperparameters

Hyperparameters can be defined as the configuration of the network structure. They are external to the model and their value cannot be estimated from the data. They are therefore set before the training begins.

There exist two types of hyperparameters : ones determining the network structure and ones determining the network training. Definitions of common hyperparameters can be found in TABLE 3.2. [54]

Hyperparameters determining network structure	Hyperparameters determining network training
<i>kernel size</i> : size of the convolutional layer filter	<i>learning rate</i> : parameter regulating the update of the weight at each iteration
<i>kernel type</i> : values used in the convolutional layer filter	<i>momentum</i> : parameter regulating the influence of the previous update on the current weight update
<i>stride</i> : number of pixels by which the filter is moved on the image	<i>number of epochs</i> : number of times the network goes through the entire training dataset during training
<i>padding</i> : addition of layers of zero values used to insure that filter goes over the edge of the input image	<i>batch size</i> : number of examples shown to the network at each training iterations

**Table 3.2:** Definitions of common hyperparameters examples in CNNs.

### 2.3.2.4 Network troubleshooting

Even though CNN models turn out to be very helpful to solve many problems, it is common that issues arise during training and that troubleshooting is required to solve them. [52]

Frequent issues calling for troubleshooting include:

1. *Training Performance*: Most often, very poor performance during training can be associated to a problem with data or with the training parameters. Different reasons can explain these problems: improper image normalization making images lose their informative features, errors in the code performing image augmentation or feeding the data into the training pipeline, etc ... If the training data is free of errors, effective ways to improve the model's performance include adjusting the learning rate and changing the model architecture to increase its capacity.
2. *Overfitting*: It is defined as the situation in which the model's learning is not something general that will work on real data but rather something unique to the training dataset. Different regularization techniques exist to reduce overfitting, among which are: batch normalization, dropout and early stopping. However, increasing the strength of  $L2$  normalization or the range of data-augmentation are also ways of mitigating overfitting.
3. *Class Imbalance*: Often in classification problems, the training dataset contains a different number of examples for each class. This can lead the model to perform poorly. There exist two main ways of overcoming class imbalance: resampling the data to get the same number of elements in each class (by downsampling or upsampling) or introducing a class weight term into the loss function that is written  $N_{\text{Total examples}}/N_{\text{examples in class } i} \times 1/N_{\text{classes}}$  for each class  $i$ .
4. *Assessing Performance*: When creating a DL model, being able to follow performance metrics during and after training is key. To do so while avoiding overfitting, the data can be split into three parts: the first for training, the second for validation during training and the third for testing real-world performance. Besides splitting the dataset, another issue consists in selecting a performance metric. Indeed, simple metrics can be misleading. For classification tasks, confusion matrix, which represent the frequency of each type of misclassification in each class, are a great way of assessing the model's performance.

### 2.3.3 Residual Networks

Deep convolutional neural networks have been successfully used in many image classification tasks and have led to breakthroughs in this field.

However, while the problem of vanishing/exploding gradients in deeper models has been largely addressed, there remains the issue of *degradation*. It is characterized by a progressive saturation followed by a rapid decrease of the model's accuracy as the depth increases. Surprisingly, the reason behind this degradation is not overfitting since it has been shown that adding more layers to an already deep model increases the training error.



This suggests that some networks are easier to optimize than others. Indeed, let us consider two models: one with a shallower architecture and the other its deeper counterpart. A solution *by construction* to the deeper model can be found using *identity* mapping in the added layers and copying the other layers learned for the shallower architecture. This implies that a deeper model's training error should not be higher than the shallower model's one. Regardless, it has been shown that current solvers are incapable of finding comparably good or better solutions, at least in feasible time, than the constructed one.

A way of addressing the degradation problem was introduced by He et al. in [15], the *deep residual learning* framework.

It makes use of the assumption that multiple nonlinear layers with inputs  $\mathbf{x}$  can asymptotically approximate sophisticated functions such as  $\mathcal{H}(\mathbf{x})$  so that, equivalently, they can asymptotically approximate residual functions  $\mathcal{F}(\mathbf{x}) := \mathcal{H}(\mathbf{x}) - \mathbf{x}$ . Thus, based on the intuition given by the degradation problem that solvers are not able to efficiently approximate identity mappings using multiple nonlinear layers, authors assume that it is less easy for these layers to approximate a function  $\mathcal{H}(\mathbf{x})$  directly rather than to first learn a residual function  $\mathcal{F}(\mathbf{x})$  and then the original function using  $\mathcal{F}(\mathbf{x}) + \mathbf{x}$ . Indeed, in the latter option, if using identity mappings is optimal, approaching them only requires the solver to drive the weights in the nonlinear layers toward zero.

Practically, residual networks (ResNet) make use of feedforward neural networks with *shortcut connections*. These connections skip one or more layers and perform identity mapping with their outputs that are then added to the outputs of the stacked layers. The advantage of these layers is that they do not introduce extra parameters or increase the computational complexity. SGD and backpropagation can still be used to completely train the entire network.

In this dissertation, the CNN that was used was a ResNet50. The building block of such a network has a so-called *bottleneck design*. It uses, for each residual function  $\mathcal{F}$ , three convolutional layers with filters of size  $1 \times 1$ ,  $3 \times 3$  and  $1 \times 1$  respectively. The name bottleneck comes from the reduction followed by a restoring of the input dimensions by the  $1 \times 1$  layers, which leaves the  $3 \times 3$  layer a bottleneck. The graphical representation of a bottleneck building block for ResNet50 can be found in FIGURE 3.14. [15]

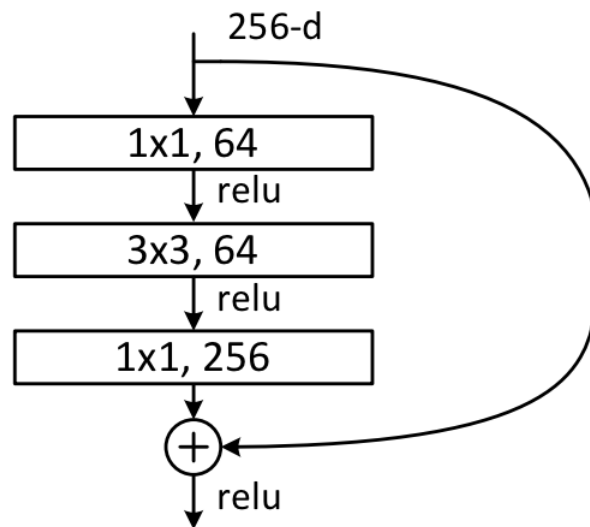


**Figure 3.14:** *Bottleneck* building block for ResNet50. (Taken from [15])

The overall ResNet50 is composed of different layers:

1. A convolutional layer with a  $7 \times 7$  kernel size and 64 different kernels that are passed over the input image with a stride of 2 and a max pooling layer whose stride is also 2.
2. Nine layers made of three bottleneck building blocks each using a first  $1 \times 1$  convolutional layer with 64 kernels followed by a  $3 \times 3$  convolutional layer with 64 kernels and finally a second  $1 \times 1$  convolutional layer with 256 kernels.
3. Twelve layers with four bottleneck building blocks with a  $1 \times 1$  layer with 128 kernels, a  $3 \times 3$  layer with 128 kernels and a  $1 \times 1$  layer with 512 kernels.
4. Eighteen layers with 6 building blocks having a  $1 \times 1$  layer and  $3 \times 3$  one with 256 kernels as well as a  $1 \times 1$  layer with 1024 kernels.
5. Nine layers made of three building blocks with a  $1 \times 1$  and a  $3 \times 3$  layer having 512 kernels as well as a  $1 \times 1$  layer with 2048 kernels.
6. One final average pooling layer followed by a 1000-way fully-connected layer with softmax.

At each change of building block, the shortcut performs an identity mapping but adds extra zeros entries via padding in order to increase the output dimensions. [55]

### 3 Color Deconvolution

When studying tissues, differential staining of the cytoplasm, cell nuclei and other organelles is crucial. Indeed, each dye has a specific light absorption factor and preferential affinity for a particular element. Therefore, when a dye binds to a cellular element, it will absorb a certain amount of light (proportional to the amount of dye) and make the element appear a specific color, allowing it to be distinguished from the other elements visible on the tissue section.

In the case of H&E staining, the staining of the cell nuclei in blue by the hematoxylin allows to differentiate them from the cytoplasm, stained in red-magenta by the eosin. However, since the two dyes are used successively, they will both have a contribution on the amount of light absorbed by a specific element.

This means that, if a user wants to focus solely on the cell nuclei (to quantify them for instance), he will need to perform what is called *stain separation* to isolate the contribution of the hematoxylin stain. Stain separation can be defined as: "*the process whereby a full colour histology section image is transformed into a series of single channel images, each corresponding to a given stain's expression*"[56].

One of the first and most powerful stain separation methods is the one presented by Ruifrok et al. in [57], called *color deconvolution*. It is based on the assumption that each of the RGB channels in the tissue section image is linear with the brightness or transmission  $T$ , with  $T$  defined as  $I/I_0$  ( $I_0$  being the incident light and  $I$  the transmitted light). Using the Lambert-Beer's law, they describe the detected intensities of light transmitted through a specimen and an amount  $A$  of stain with an absorption factor  $c$  as:

$$I_C = I_{0,C} \exp(-A \times c_C) \text{ with the subscript C being R, G or B} \quad (3.1)$$

As it can be seen from EQUATION 3.1, the transmission of light, and thus the intensities of each RGB channel, are expressed using a non-linear function of the concentration of stain. Therefore, this means that  $T_R$ ,  $T_G$  and  $T_B$  can not directly be used to separate the stains.

Nonetheless, one can define the Optical Density (OD) of each channel as:

$$OD_C = -\log_{10}(I_C/I_{0,C}) = A \times c_c \quad (3.2)$$

This expression being linear with the amount of stain, the OD of each channel can therefore be used to retrieve the contribution of a particular dye.

In the case of a combination of hematoxylin and eosin, EQUATION 3.2 for a particular pixel can be rewritten as the following matrix multiplication:

$$\begin{pmatrix} OD_R \\ OD_G \\ OD_B \end{pmatrix} = \begin{pmatrix} H_R & H_G & H_B \\ E_R & E_G & E_B \\ Bg_R & Bg_G & Bg_B \end{pmatrix} \cdot \begin{pmatrix} A_H \\ A_E \\ A_{Bg} \end{pmatrix} \quad (3.3)$$

$$\mathbf{OD} = \mathbf{M} \cdot \mathbf{A} \quad (3.4)$$

where  $\mathbf{OD}$  is the  $3 \times 1$  vector of OD-levels detected at that pixel,  $\mathbf{M}$  is the normalized OD matrix whose columns correspond to the normalized vector of OD levels in each RGB channel for each pure stain <sup>3</sup> and  $\mathbf{A}$  is the  $3 \times 1$  vector of amounts of each stain at that pixel. The notations  $H$ ,  $E$  and  $Bg$  are used here to respectively represent the hemotoxylin, the eosin and the background channels of the image.

This means that, by multiplying the OD image with the inverse of the OD matrix, one can get an orthogonal representation of the stains forming the image:

$$\mathbf{A} = \mathbf{D} \cdot \mathbf{OD} \quad (3.5)$$

where the matrix  $\mathbf{D} = \mathbf{M}^{-1}$  is defined as the deconvolution matrix.

In this dissertation, color deconvolution is used to extract the hemotoxylin channel from the scanned H&E sections.

---

<sup>3</sup>This matrix can also be called the mixing matrix [58]

# Chapter 4

## Materials and Methods

This chapter describes the overall workflow employed to create and analyze fully annotated 3D reconstructions of tissue engineered bone samples. Each step and method involved in this workflow are, in turn, further detailed and explained.

### 1 Development Environment

The programming and analysis were developed using the `Matlab` 2020 software and its *Image Processing*, *Parallel Computing*, *Statistics and Machine Learning*, *Signal Processing* and *Deep Learning* Toolboxes.

### 2 Overall Workflow

The overall workflow used in this dissertation is based on the CODA method presented by Kiemen *et al.* in [17]. The method, initially developed for pancreatic cancer samples, is adapted here for the study of tissue engineered bone constructs.

The employed workflow can be broken down into four main steps (FIGURE 4.1). In the first step, acquisition, samples are engineered, prepared, stained and scanned. The second step consists in the learning of a DL model from manual annotations of the scanned tissue sections. The model is used to label the different tissue subtypes present on the images. During the third step, the labeled tissue sections are aligned and stacked to create 3D reconstructions of the different samples. This is namely done by applying Image Registration, a method detailed in the first section of CHAPTER 3, to the samples histological sections. Finally, the fourth and last step uses the reconstructed and annotated volumes to perform quantification analysis at the tissue and at the cell level.

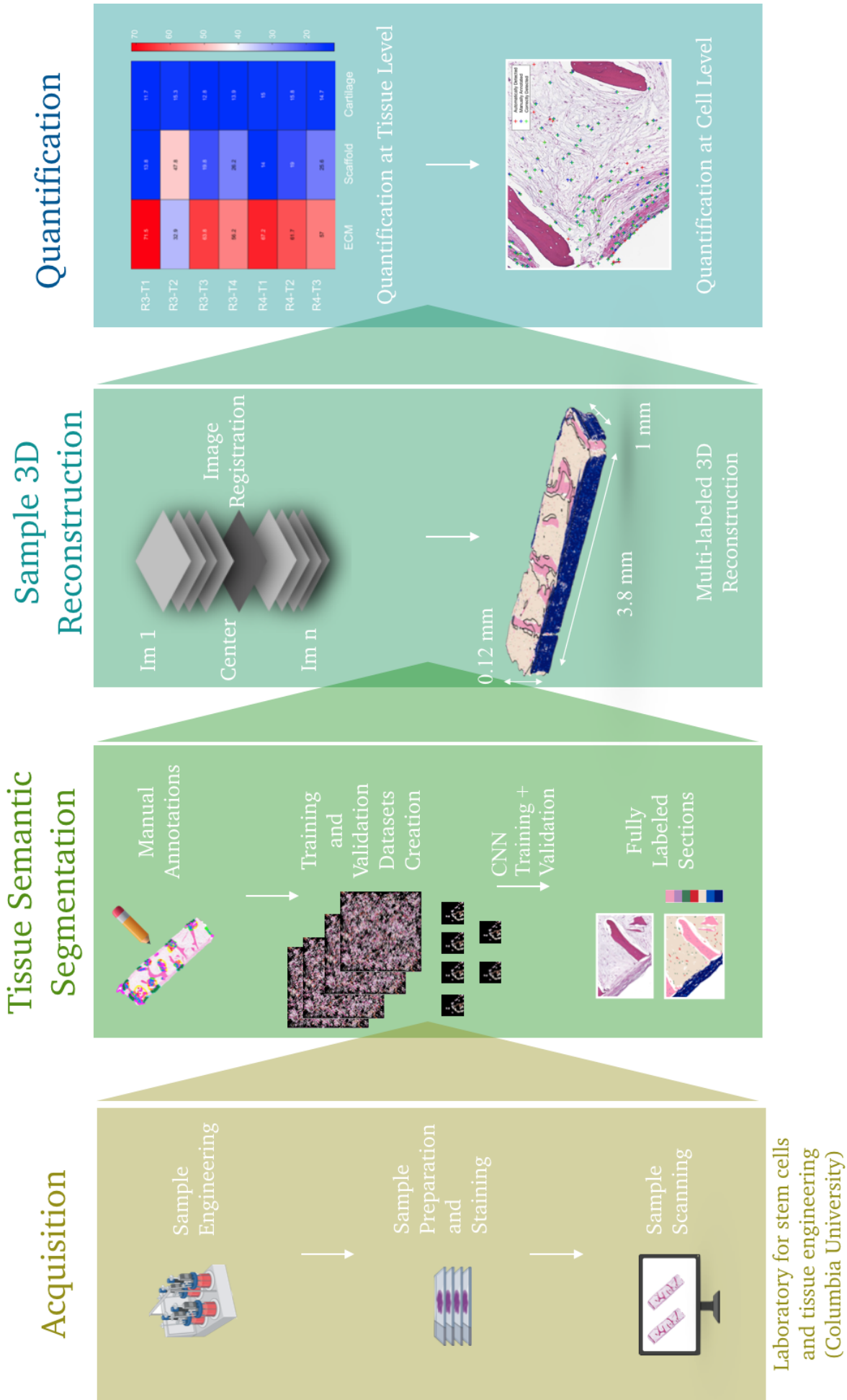


**Figure 4.1:** CODA workflow adapted to tissue engineered bone samples.

### 3 Sample Acquisition

The tissue engineered bone samples were grown, prepared, stained and scanned at the Laboratory for Stem Cells and Tissue Engineering in Columbia University, NY.

Pr.Gordana Vunjak-Novakovic is an award-winning scientist and a world leading expert in the field of tissue engineering and regenerative medicine. Along with her team, she has published 3 books and 415 journal articles on the development of innovative technologies for engineering functional human tissues and organs including bone, heart, lung and vasculature. [59]

#### 3.1 Tissue Engineering Process

First, seven bone scaffolds were prepared from decellularized bovine bone.

This was done by using a band saw to cut approximately 4cm tall trabecular bone cores from the distal end of bovine calf metacarpals that were previously purchased in bulk and stored at  $-40^{\circ}\text{C}$ . Bone cores with a section of  $4\text{mm} \times 8\text{mm}$  were then generated with a CNC milling machine while an IsoMet low speed wafering saw was used to cut 1mm thick sections.

Each of the 4 mm wide  $\times$  8 mm long  $\times$  1 mm thick sections was decellularized using a protocol established in [16], it allows to remove all cellular material while preserving the bone matrix composition and architecture. This was done by performing the following sequence of steps on an orbital shaker:

1. Phosphate buffered saline with 0.1 EDTA (w/v) for 1 hour at room temperature
2. 10mM tris, 0.1 EDTA (w/v) in deionized (DI) water overnight at  $4^{\circ}\text{C}$
3. 10 mM Tris, 0.5 sodium dodecyl sulfate (w/v) in DI water for 24 hours at room temperature
4. 100 U  $\text{ml}^{-1}$  DNase, 1 U  $\text{ml}^{-1}$ , 10 mM Tris in DI water for 6 hours at  $37^{\circ}\text{C}$

The resulting bone matrix scaffolds were lyophilized and weighted to verify that each piece had an adequate matrix density for cell seeding. They were then subjected to 70 ethanol treatment under ultraviolet light overnight as well as incubated overnight in Dulbecco's Modified Eagle Medium (DMEM) for sterilization.

Each scaffold was then seeded with  $4 \times 10^5$  expanded bone-marrow derived MSC (Lonza) or hiPSC-derived MSC suspended in 40  $\mu\text{L}$  of medium (DMEM supplemented with 10 (v/v) HyClone fetal bovine serum (FBS), 1 penicillin/streptomycin, and 1 ng  $\text{mL}^{-1}$  of basic fibroblast growth factor (bFGF)) by following established protocols. The STEMdiff mesenchymal progenitor kit (STEMCELL technologies, 0529) was used according to the manufacturer protocol to differentiate hiPSC (WT-11 cell line) into MSC. The cells were allowed to attach for two hours before being supplemented with additional medium (DMEM supplemented with 10 (v/v) HyClone fetal bovine serum (FBS), 1 penicillin/streptomycin, and 1 ng  $\text{mL}^{-1}$  of basic fibroblast growth factor (bFGF)) overnight. The medium was changed the following day to osteogenic media (low glucose DMEM supplemented with 1  $\mu\text{M}$  dexamethasone (Sigma-Aldrich), 10 mM  $\beta$ -glycerophosphate (Sigma-Aldrich), and 50  $\mu\text{M}$  L-ascorbic acid-2-phosphate (Sigma-Aldrich)) to initiate

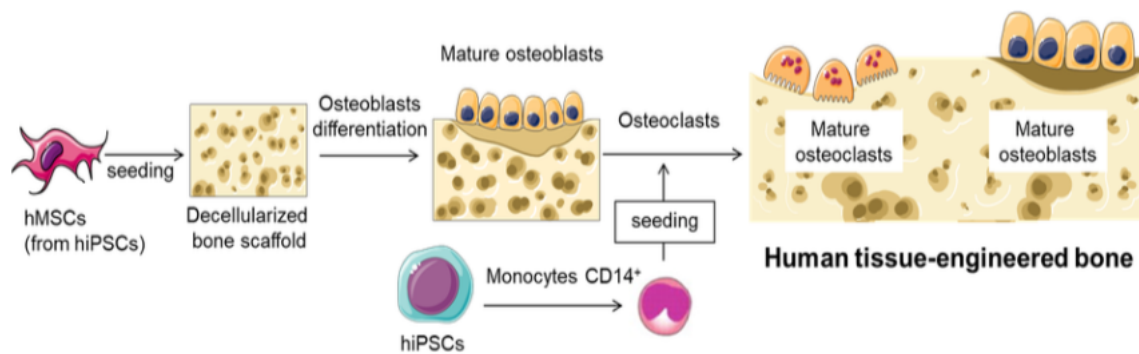


**Figure 4.2:** Tissue engineering protocol schematic. (Taken from [16])

osteogenic differentiation. Scaffolds were then incubated for three weeks in 4mL of osteogenic media with media changes three times a week. This allows for the differentiation of MSC into functional, maturing osteoblasts.

The scaffolds were then seeded with expanded primary monocytes and differentiated into functional and mature osteoclasts.

To do so, density gradient centrifugation with Ficoll-Paque PLUS (GE Healthcare, 17-1440-02) was first used to isolate peripheral blood mononuclear cells (PBMC) from buffy coats of human blood (fully deidentified samples obtained from the New York Blood Center). Immunomagnetic isolation of monocytes (Big Easy EasySep Magnet, Stem Cell Technologies, 180001) was performed according to manufacturers protocol using negative selection (EasySep Human Monocyte Isolation Kit, Stem Cell Technologies, 19359). In a humidified incubator at 37°C and 5 CO<sub>2</sub>, 8 × 10<sup>6</sup> monocytes were cultured for the following two days on 25 cm<sup>2</sup> ultralow attachment flasks (Corning, 3815) with 10 mL of maintenance medium (RPMI 1640, ATCC, 30-2001) supplemented with 10 heat-inactivated human serum (Corning, 35-060), 1 penicillin/streptomycin, and 20 ng mL<sup>-1</sup> recombinant human MCSF (M-CSF, PeproTech, 300-25). Inside each scaffold, 4 × 10<sup>5</sup> human CD14<sup>+</sup> monocytes were seeded using 40 μL of medium and allowed to attach for two hours at 37°C in a humidified incubator at 5 CO<sub>2</sub>. They were subsequently differentiated for two weeks into osteoclasts in Minimum Essential Medium Eagle Alpha modification (α-MEM, Sigma, M4526) supplemented with 10 (v/v) heat-inactivated HyClone FBS, 1 penicillin-streptomycin, 1-Glutamine (Gibco, 25030-081), 20 ng mL<sup>-1</sup> Recombinant Human MCSF (PrepoTech, 300- 25) and 40 ng mL<sup>-1</sup> recombinant human sRANK Ligand (PrepoTech, 310-01). Cells were maintained at 37°C in a humified incubator at 5 CO<sub>2</sub> while cytokines were replaced every three days.

The overall tissue engineering protocol to produce human bone is summarized in FIGURE 4.2.

The engineered bones were then placed into a microfluidic platform above a vascularized membrane. Inside the vascular channel, a 100K single cell suspension of cancer cells (Prostate: LnCaP and VCaP, Breast: MBA-MD-231) is injected and allowed to circulate for 4 weeks. The setup can be observed in FIGURE 4.3. Tracking of the metastatic colonization into the bone over time was performed using small animal imaging techniques (IVIS imager).



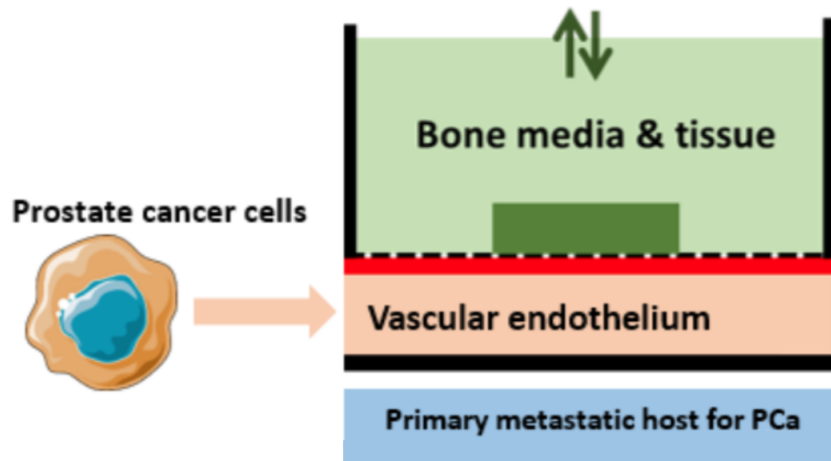


**Figure 4.3:** Set up for cancer cells infusion inside tissue engineered bones. (Courtesy of Laboratory for Stem Cells and Tissue Engineering, Columbia University)

### 3.2 Sample Preparation and Scanning

Upon harvest, the tissue constructs were fixed for 24 hours in paraformaldehyde (PFA), washed in PBS, and submitted to the Herbert Irving Comprehensive Cancer Center (HICCC) Molecular Pathology Lab at Columbia University for paraffin embedding and sectioning. Serial sections (4 $\mu$ m thick) were stained using H&E and imaged on an Olympus slide scanner.

## 4 Tissue Semantic Segmentation

The second step consisted in the learning of a DL model from manual annotations of the different samples which was then used to label the different tissue and cell types present on the histological H&E sections.

The steps involved in the creation of the model are summarized on FIGURE 4.4.

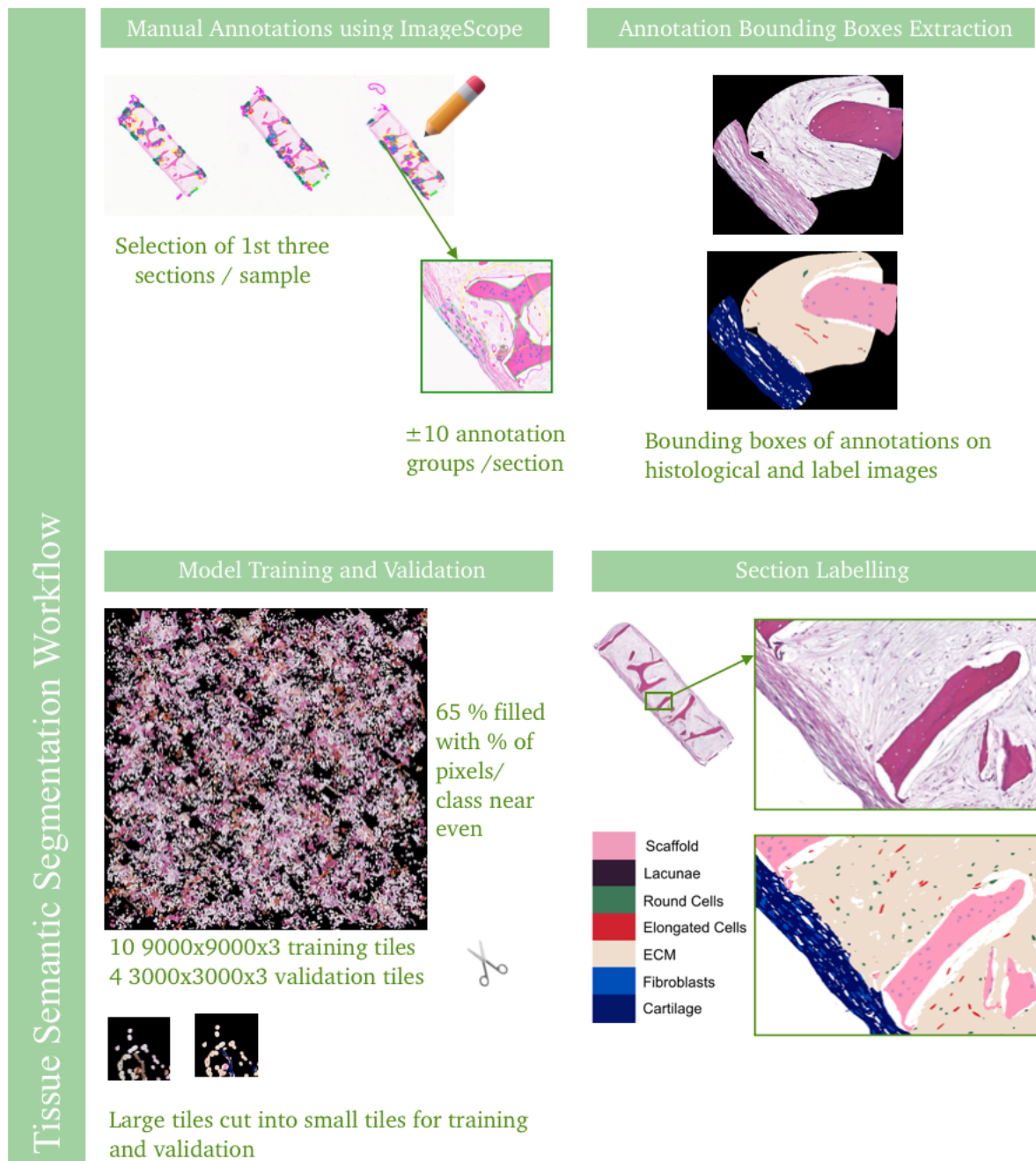


**Figure 4.4:** Overview of the tissue semantic segmentation workflow.

## 4.1 Training and Validation Datasets Creation

First, copies of the tissue images with a size corresponding to  $1\mu\text{m}/\text{pixel}$  were created using the `Openslide` software with nearest neighbor interpolation. Then, the first three images of each sample were selected and each image was annotated with approximately 10 annotation groups (*i.e.* grouped annotations of all the identified tissue subtypes). A description and an histological example of each identified subtype can be found in SECTION A, TABLE A.1. The annotations were made using `Aperio ImageScope`, which allows to create `.xml` files containing the coordinates of each annotation. These files were then loaded into `Matlab` and overlaid on the  $2\mu\text{m}/\text{pixel}$  images after being downsampled.

Secondly, the bounding boxes of all annotations were identified and used to extract the annotated RGB image regions that were then each saved as a separate image file. A matrix, in which each bounding box image was associated to its annotation tissue type, was simultaneously created.

The following step consisted in the creation of a large  $9000 \times 9000 \times 3$  black image tile that served as the basis for a first training image. The latter was built by randomly overlying annotation bounding boxes of the least represented deep learning class on the tile until it got  $> 65\%$  covered with annotations and in such a way that each deep learning class approximately shared the same number of pixels. A total of 10 training tiles were built.

Data augmentation can be very helpful when building a training dataset, since its size is of crucial importance in the training of a trustworthy and robust network. This process consists in generating more data by starting from an already existing set of examples. Here, it was performed on the images by applying different small transformations: rotation, scaling or hue augmentation. In general, this allows to avoid overfitting of the network since it introduces diversity in the training examples, making the network less sensitive to small changes in the data. However, here, the hue augmentation is also used to help the network deal with small color changes between images of histological samples that were possibly prepared and scanned in different conditions, thus having heterogeneous staining patterns.

Therefore, for half of the training tiles, the annotation bounding boxes were randomly augmented via rotations, scaling (by a random factor between 0.8 and 1.2) and hue augmentation (by a random factor between 0.8 and 1.2 in each RGB color channel). Each training tile was then sectioned in  $144\ 725 \times 725 \times 3$  training images. Four other  $3000 \times 3000 \times 3$  tiles were created following the same procedure and sectioned to form  $64\ 375 \times 375 \times 3$  validation images.

## 4.2 CNN Training and Validation

Once the training and the validation datasets were created, a CNN was trained in order to be used on the histological sections of the different samples.

The model’s architecture and hyperparameters were chosen to be the same as the ones employed in the original CODA method. [17] Therefore, `DeepLab v3+x` [60] was used to

create a ResNet50 <sup>1</sup> that was solved with the help of the ADAM optimization algorithm. The values of the different hyperparameters used to train the network, as well as their respective definitions, can be found in TABLE 4.1.

### 4.3 Section Labelling

Once the validation criterion was met, all tissue sections were semantically segmented and fully labelled tissue images with a pixel resolution of 2 $\mu$ m/pixel were created.

The overall quality of the semantic segmentation was assessed by visual inspection of randomly chosen images. If too many labelling errors were spotted, existing manual annotations were refined, new annotations were added and a new model was build and trained following the procedure just described. Once the performances of the model were judged satisfactory, its labelled 2 $\mu$ m/pixel images were selected and used for further manipulations.

---

<sup>1</sup>see SECTION 2.3.3 for further explanation about this architecture

Option Name	Definition	Value used for training
'MaxEpoch'	"Maximum number of epochs that can be used for training"	12
'MiniBatchSize'	"Size of the mini-batch that can be used at each iteration of the training algorithm "	3
'Shuffle'	"Option for data shuffling"	'every-epoch': "shuffle the training data before each training epoch and shuffle the validation data before each network validation"
'ValidationPatience'	"Number of times that the loss on the validation set can be larger than or equal to the previously smallest loss before network training stops"	6
'InitialLearnRate'	"Initial learning rate used for training. If the learning rate is too low, then training takes a long time. If the learning rate is too high, then training might reach a suboptimal result or diverge."	0.00025
'LearnRateSchedule'	"Option for dropping the learning rate during training."	'piecewise': "the software updates the learning rate every certain number of epochs by multiplying it with a certain factor."
'LearnRateDropPeriod'	"Number of epochs for dropping the learning rate"	1
'LearnRateDropFactor'	"Factor for dropping the learning rate"	256
'ExecutionEnvironment'	"Hardware resource for training network"	'gpu': "Use the GPU"
'Plots'	"Plots to display during network training"	'training_progress': "Plot training progress. The plot shows mini-batch loss and accuracy, validation loss and accuracy, and additional information on the training progress."

**Table 4.1:** Values and definitions of the options used during training of the deep neural network. [20]

## 5 Sample 3D Reconstruction

The labelled tissue sections created by following the procedure described in the previous section are then aligned into the same coordinate system and stacked to create a 3D matrix for each sample. This is done through the use of Image Registration results on down-sampled versions of the original scanned histological sections.

The steps involved in the creation of these 3D renderings are summarized on FIGURE 5.3.

### 5.1 Image Registration

`Openslide` software was, once again, used to save reduced-size copies of the original tissue images having a resolution of approximately  $0.5\mu\text{m}/\text{pixel}$ . Thus, images with a resolution of  $8\mu\text{m}/\text{pixel}$  were created using nearest neighbor interpolation. These down-sampled versions of the high-resolution histological sections were also smoothed by conversion to greyscale, removal of non-tissue objects in the image, intensity complementing and Gaussian-filtering.

Next, by taking the center image of each sample as the reference point, global and elastic registration were used to align all the other pre-processed images of the different samples.

First, the rigid transformation parameters necessary for global registration were found through maximization of cross-correlation.

This was done by calculating the RT of the images at discrete angles between 0 and 359 degrees. Then, the maximum of the RT cross correlations was used to obtain the registration angle while the maximum of the cross-correlation of the rotated images yielded the translation. As explained in SECTION 1.2.3, the RTs and the cross-correlations were respectively computed via the `radon` and the `xcorr2` build-in `Matlab` functions.

Each image  $\text{image}_{n+/-m}$  was sequentially registered to the three images that were closest to the center,  $\text{image}_{n+/(m+1)}$ ,  $\text{image}_{n+/(m+2)}$  and  $\text{image}_{n+/(m+3)}$  using rigid global registration. The registration leading to the highest pixel-to-pixel correlation between the moving and the reference image was selected while the two others were forsaken.

Secondly, elastic registration was performed on the moving image with respect to the chosen reference image and it led to a nonlinear displacement map between these images. To do so, cropped tiles at 1.5mm intervals across the globally registered  $8\mu\text{m}/\text{pixel}$  images were used. Rigid registration was calculated for each tile, which lead to local rigid registration fields that were then interpolated and smoothed. This created a nonlinear, elastic registration transformation.

The overall elastic registration process described above was then repeated for all images in the sample such that they all shared the coordinate system of the center image  $\text{image}_n$ . This was then applied to all 7 tissue engineered bone samples independently.

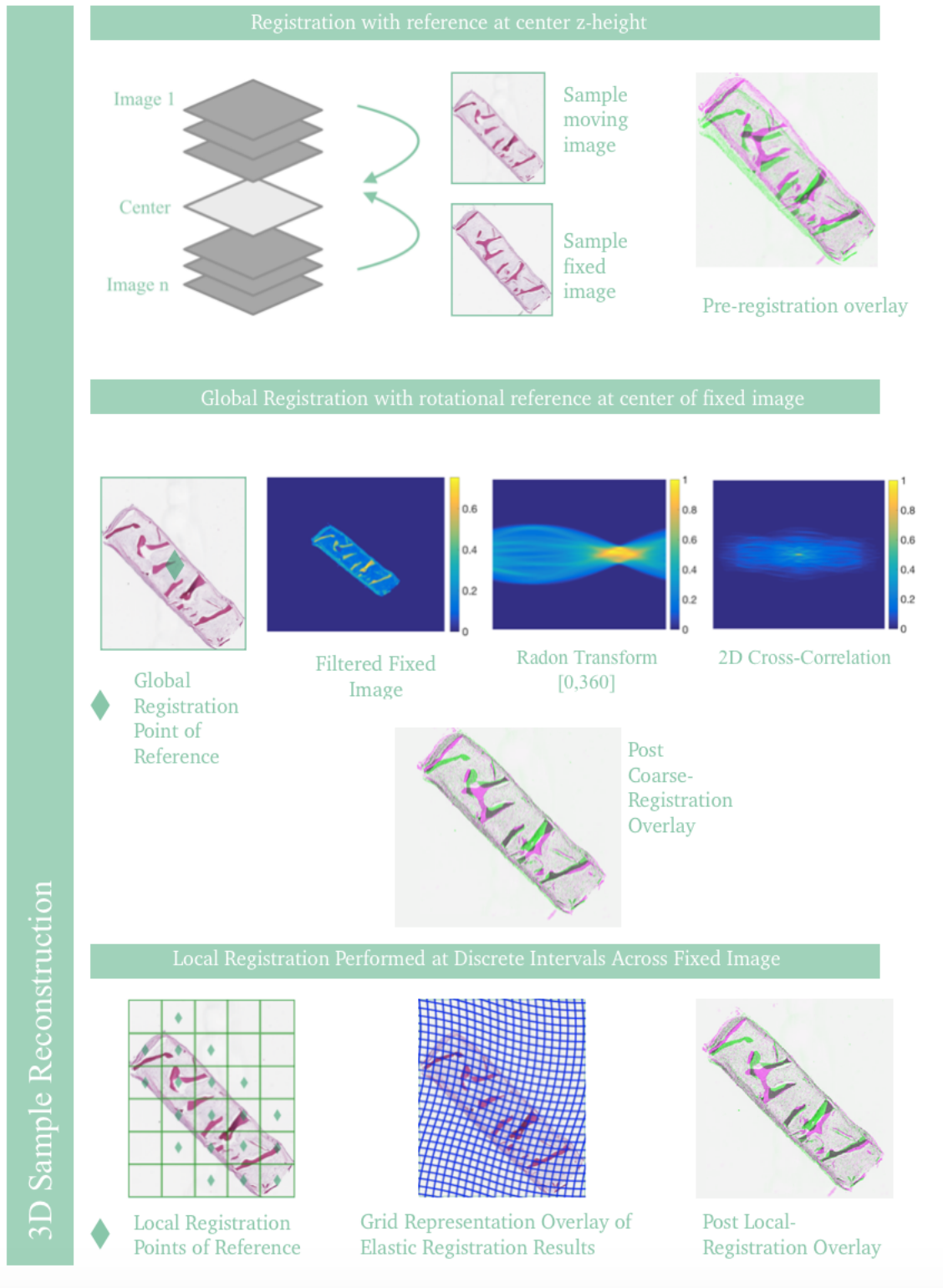


**Figure 4.5:** Histological image registration workflow.

## 5.2 Creation of 3D Renderings

The results of the image registration process on the H&E sections were used to consolidate the semantically segmented images into a 3D matrix. Using the `patch` and `isosurface` `Matlab` commands as well as assigning a unique RGB color triplet to each tissue class allowed for the construction of 3D renderings of the different samples, labelled with single-cell precision.

These different 3D renderings had a resolution of  $2\mu\text{m}/\text{pixel}$  in  $xy$  and a resolution of  $4\mu\text{m}/\text{pixel}$  in  $z$  (all tissue sections were used in this analysis). Nonetheless, they were sub-sampled for all calculations using nearest neighbor interpolation such that their voxel went from  $2 \times 2 \times 4\mu\text{m}^3/\text{voxel}$  to an isotropic  $4 \times 4 \times 4\mu\text{m}^3/\text{voxel}$ .



## 6 Quantification

The 3D labelled matrices of each sample were then used to perform some quantification, at the tissular and at the cellular level.

### 6.1 Quantification at the Tissue Level

First, quantification at the tissue level allowed to obtain information about the total tissue volume, the respective proportion of the different tissue subtypes but also the volume of the different tissue subtypes. More refined insight on the morphology of the scaffolds used in the samples was computed as well.

#### 6.1.1 Calculation of Tissue Content and Volume

The different percentages of tissue content were each computed, in the isotropic 3D matrix, as the total number of voxels occupied by their corresponding tissue subtype divided by the total number of voxels identified as tissue in the 3D matrix. This was done, in turn, for each tissue subtype in each sample.

The total volume of tissue was computed as the total number of voxels in the tissue region of the 3D matrix multiplied by the corresponding volume of a voxel, that is  $4\mu\text{m} \times 4\mu\text{m} \times 4\mu\text{m}$ . The volume of each tissue subtype was then computed by multiplying the corresponding tissue content percentage with the total volume of tissue. Once again, this was done for each tissue subtype of each sample.

The mean scaffold porosity for each scaffold was also computed as the number of voxels occupied by the lacunae divided by the sum of the number of voxels occupied by the scaffold and the number of voxels occupied by the lacunae.

#### 6.1.2 Morphological Characterization of Scaffold Pieces

A morphological assessment of the different pieces of scaffold present in the samples was performed. A piece of scaffold was identified, in the 3D isotropic matrix, as a group of over 15 625 connected voxels having the scaffold label. Indeed, groups of less than 15 625 connected voxels, therefore having a volume of less than  $1 \times 10^{-3}\text{mm}^3$ , were considered to be noise rather than real scaffold pieces. The morphological assessment of the pieces was performed using a build-in `Matlab` function, `regionprops3`. It was used to compute the extent, the solidity and the volume of each scaffold piece. The extent was calculated as the ratio of the number of voxels in the piece to the number of voxels in its total bounding box. The solidity was computed as the number of voxels in the piece divided by the number of voxels in its convex hull. Finally, the volume was computed as the number of voxels in the scaffold piece multiplied by the volume of a voxel.

### 6.2 Quantification at the Cell Level

Secondly, quantification at the cell level allowed to obtain information about the overall cellular content.

However, instead of computing cellular content only with the 3D labelled matrices, the results obtained using DL are refined and validated by detecting the cell nuclei on the H&E sections. Therefore, a method to accurately and reliably detect the nuclei on the histological sections is first tested and implemented. Then, the results of this technique are combined with the results of the CNN classification to compute the cellular content of the different samples.

### 6.2.1 Nuclei Detection on histological sections

Different techniques were implemented and their results were compared to count the cells nuclei present on the reduced-size copies of the histological sections.

#### 6.2.1.1 Color Deconvolution

First, a color deconvolution algorithm<sup>2</sup> was implemented. The goal here was to obtain gray level intensity images of the hematoxylin channel by starting from reduced-size copies of tissue sections with a resolution of  $2\mu\text{m}/\text{pixel}$ .

The first step in color deconvolution requires to determine a staining matrix corresponding to the combination of dyes used on the samples. To do so, three types of staining matrices were used and their results on a randomly chosen test image were compared:

1. **Obtained with Kmeans clustering:** The first staining matrix was obtained using a method similar to the one presented by Kiemen et al. in [17]. Regions of the images with low green intensity and high RGB standard deviation were first found and identified as the tissue regions. Then, the OD values in each RGB channel at each pixel were computed. Next, the image OD values were reduced to a 1000 clusters using kmeans clustering. The hematoxylin channel was thus set to be the most common blue-favored OD channel while the eosin channel was set as the most common red-favored one. Finally, the background channel was chosen as the OD values of the most commonly found intensities in each of the three RGB channels.
2. **Given by the *Color Deconvolution 2* plugin in Image J :** The second option consisted in using the *Color Deconvolution 2* plugin available in Image J [61]. This plugin comes with a series of built-in vectors, determined experimentally, for common dyes combinations. In the case of H&E, there are two available stain vectors : H&E and H&E2. Both vectors were extracted and tested as staining matrices.
3. **Determined with visual inspection:** The third staining matrix was determined via visual inspection. Therefore, a  $50 \times 3$  RGB intensity values vector for 50 pixels that were visually associated to cell nuclei was first built. The hematoxylin channel was then set as the OD values corresponding to the mean of this vector. A similar process was used to set the eosin channel. However, the vector of RGB values was

---

<sup>2</sup>based on the one introduced by Ruifrok et al. in [57], and whose theoretical basis was detailed in SECTION 3

built using 25 dark pixels that belong to the edge of scaffold pieces and 10 others that belong to the core of the cartilage layer. Finally, the background channel was built using the default values of the H&E2 staining matrix.

The second step therefore consisted in using the different staining matrices previously obtained as well as computing the OD levels to solve EQUATION 3.4 at each pixel.

### 6.2.1.2 Filtering

The second step in order to detect the nuclei present on the histological sections consisted in the filtering of the hematoxylin channel image. This was done to smooth the images and reduce their noise.

Once again, different methods were implemented and their results on the test image were compared in order to select the most effective one.

Based on the literature, three combinations of filters were used:

1. **Gaussian Filtered Image - Average Filtered Image:** As described in [62], this method consists in first convolving the image with an average 2D filter whose window size is two times larger than the apparent radius of a cell to obtain the background image,  $I_B$ . The original image is then convolved with a spatial Gaussian smoothing filter that has the same size as the average filter previously used and a standard deviation equivalent to  $\sqrt{2}$ , resulting in the image  $I_C$ . Finally, the reduced-noise, no background image  $I_N$  is obtained by subtracting  $I_B$  from  $I_C$ .
2. **Median Filter then Gaussian Filter:** This filter combination was inspired by [63]. As suggested, a median filter is first used on the image to get rid of salt and paper noise. Then, a Gaussian filter is used to smooth the image. Both the median and the Gaussian filter were used with a size two times larger than the apparent radius of a cell and the Gaussian filter standard deviation was also equivalent to  $\sqrt{2}$ .
3. **Gaussian Filtered Image - Average Filtered Image then Gaussian Filter:** The method was once again based on [17]. It consists in using the same combination of filters as the first one but, this time, a Gaussian filter is also used on the  $I_N$  image. The latter Gaussian filter standard deviation was 1.

### 6.2.1.3 Peak Intensity Detection

The cell nuclei positions were then determined as the local intensity maxima in the filtered images. The `Matlab` function used for this purpose is the `pkfnd.m` function implemented in 2005 by Eric R. Dufresne at Yale University.

The function was used with a threshold of 50 and a `sz` variable of 6.

### 6.2.1.4 Performance Assessment and Validation

Performance assessment was done for each combination of hematoxylin channel image and each filtering technique. This was performed by counting the number of cells that were correctly detected by the algorithm, with the reference being the positions of the 150 cell nuclei manually detected and annotated on a random  $501 \times 821$  testing image. A nuclei was considered as being correctly classified if it was within 5 pixels from the manually annotated nuclei. This gave a percentage of correctly classified positions while a percentage of false positive was computed by dividing the number of falsely detected nuclei (computed as the difference between the total number of nuclei automatically detected in the image and the number of correctly detected cells) by the total number of nuclei in the image.

The method with the best performance was then validated on another  $501 \times 821$  random image with 388 cells.

### 6.2.2 Cell Count and Tissue Cell Density

Cell count for each cell subtype (*i.e.* elongated cells, round cells or fibroblasts) were computed by combining the cell subtype data in the multilabelled 3D matrix with cell coordinate data in the cell 3D matrix: for example, if the coordinates of the detected cell were located in a region labelled as fibroblast by the deep learning model, the cell was thus labelled as a fibroblast.

True 3D cell counts were estimated from the 2D cell coordinates using nuclear diameters measured in situ. This was done based on the assumption that the algorithm could detect cells if any part of their nucleus touched the tissue section, which implies that effective tissue section thickness corresponds to the true thickness of the tissue section plus the diameter of the cell.

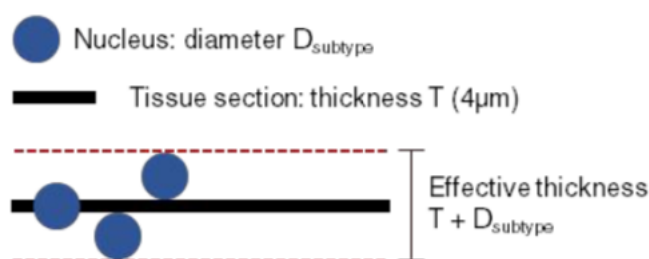


**Figure 4.6:** Effective tissue section thickness extrapolation. (Taken from [17])

Therefore, the estimated 3D cell count ( $C_{3D}$ ) was obtained by the multiplying 2D cell counts with the true tissue section thickness using the formula:

$$C_{3D} = \sum_{images} \sum_{subtypes} C_{image} \frac{T}{T + D_{subtype}} \quad (6.1)$$

where  $C_{image}$  is the cell count for a given tissue image,  $T$  is the thickness of the histological section, and  $D_{subtype}$  is the measured diameter of a nucleus for a cell subtype.

Cell Subtype	Nuclear Diameter [ $\mu\text{m}$ ]
Fibroblasts	20
Round Cells	4
Elongated Cells	14

**Table 4.2:** Cell subtypes and the corresponding mean nuclear diameter measured in *Aperio ImageScope*.

Cell diameters for each cell subtype were computed as the mean value of 10 nuclei diameter measures for each cell subtype using *Aperio ImageScope*.

For each tissue subtype, bulk 3D cell density was computed by dividing the 3D extrapolated cell count of a particular subtype by the total volume of tissue. Therefore, the bulk 3D density of fibroblasts in the cartilage was computed as the ratio between the 3D cell count of fibroblasts and the total volume of cartilage in the sample while the bulk 3D density of elongated cells in the ECM was computed as the ratio between the 3D cell count of elongated cells and the total volume of ECM in the sample.

# Chapter 5

## Results

This chapter is used to present the results of the use of CODA on the bone tissue engineered models and of the different computations that were performed, which were previously detailed in CHAPTER 4.

### 1 CODA

We used a total of seven tissue engineered bone samples infused with either prostate or cancer cells that were fixed in formalin, embedded in paraffin and subsequently serially sectioned every  $4\mu\text{m}$ . H&E was used to stain the sections, which were then scanned at  $20\times$  magnification. The resulting images had a resolution of  $0.5\mu\text{m}$  in the x-y plane and a resolution of  $4\mu\text{m}$  in the z direction.

Sample Name	MDA-MB-231 Cell Line	LnCaP Cell Line	VCaP Cell Line	Dimensions (H×W×T) [mm×mm×mm]
R3T1	×			$3.8 \times 1 \times 0.12$
R3T2	×			$3.7 \times 1.1 \times 0.12$
R3T3		×		$3.8 \times 0.9 \times 0.12$
R3T4	×			$3.6 \times 1.2 \times 0.12$
R4T1	×			$4.1 \times 1.1 \times 0.12$
R4T2			×	$4.8 \times 1.4 \times 0.12$
R4T3	×			$3.8 \times 1.1 \times 0.12$

**Table 5.1:** Samples, their dimensions [mm] and the cancer cell line they were infused with.

CODA was then used to digitally reconstruct the serial tissue images of each sample into multi-labelled volumes with single-cell resolution.

## 1.1 Semantic Segmentation

A pre-trained ResNet50 network was used to label 7 different types of tissular or cellular components on the H&E stained sections of the different samples, without the use of any additional molecular probes. These components include: decellularized scaffold of trabecular bovine bone, lacunae inside the scaffold, new osteogenic ECM, two cell phenotypes encountered in the ECM (round and elongated cells), fibroblasts, and cartilage. These components are detailed in APPENDIX 1, TABLE A.1.

The network was trained using manual annotations of the different elements on histological sections. The training dataset was created by semi-randomly overlaying annotated regions on large image tiles that were then cut into many training and validation images. This allowed to control the heterogeneity in class appearance, which increased the model accuracy.

Once trained, the deep learning model precision and recall for each class on independent testing images were assessed.

		Predicted Class								
		Scaffold	ECM	Round Cells	Cartilage	Whitespace	Elong. Cells	Lacunae	Fibroblasts	
True Class	Scaffold	60 977	495	20	138	364	19	1171	16	96.5
	ECM	676	58 288	479	416	2880	435	6	20	92.3
	Round Cells	393	6580	54 915	19	167	1006	0	120	86.9
	Cartilage	168	2171	46	53 340	1613	33	1	5829	84.4
	Whitespace	340	3935	83	1001	57 593	78	2	168	91.1
	Elong. Cells	85	7192	701	166	336	53 975	0	745	85.4
	Lacunae	1543	10	0	0	48	0	61 599	0	97.5
	Fibroblasts	125	66	176	3784	196	193	0	58 660	92.8
		94.8	74.0	97.3	90.6	91.1	96.8	98.1	89.5	

**Figure 5.1:** Confusion matrix displaying predicted vs true class outcomes for all deep learning classes. Precision and recall per class (%) are in row beneath and to the right of matrix respectively.

It was observed that the precision for the ECM was rather low. However, after inspection of the confusion matrix displayed in FIGURE 5.1, it appeared that the low precision was due to the model often mistaking round or elongated cells, whitespace and cartilage for ECM. This could be explained by the fact the ECM is mainly composed of thin tendrils of collagen that can look more or less condensed, making hard for the model to distinguish them either from the whitespace behind it or from the cartilage layer at the edges of the sample. Round and elongated cells are also often predicted as ECM by the model. These errors are thought to be due to the presence of extremely small scaffold bits resembling cell nuclei in the ECM. Therefore, it is possible that the model associates certain cells to those small bits, therefore classifying them as ECM.

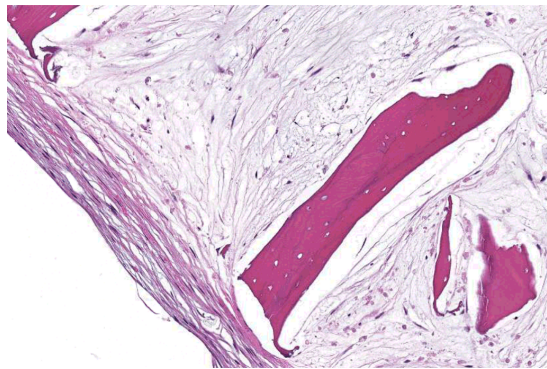
Recall for cartilage also appeared low. It was observed on the confusion matrix that the main reason for this was that the model often labelled cartilage as fibroblast. This can be explained by the fact that fibroblasts in the cartilage layer have poorly defined cytoplasm, which makes them hard to outline precisely for the model.

Different comparative figures supporting these hypothesis can be found in APPENDIX 2.



Nonetheless, considering the complexity of distinguishing the ECM from the cells, the whitespace and the cartilage as well as delimiting fibroblasts in the cartilage layer even for a trained eye, the performances of the model were judged satisfactory. Furthermore, the model showed precision and recall  $> 85\%$  for all the other class.

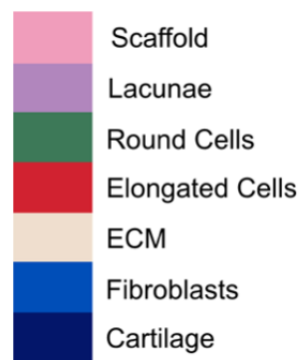
It was then used to create  $2\mu\text{m}/\text{pixel}$  labelled versions of the serial histological sections.



(a) Histological section with  $2\mu\text{m}/\text{pixel}$  resolution.



(b) Multi-labelled version of the histological section. (Legend in FIGURE 5.2c)



(c) Semantic segmentation legend.

**Figure 5.2:** Semantic segmentation of the histological sections.

## 1.2 Image Registration

Image registration was used to map the independent serial images to a common coordinate system.

Coarse rigid registration was first performed on the tissue sections. However, because of their malleability, tissues on histological sections have the tendency to stretch, fold, and split, which can lead to nonuniform deformation between z-planes. To compensate for these local tissue warpings, elastic registration was applied.

The registration were first performed on down-sampled versions of the original  $20\times$  images to limit computation time.

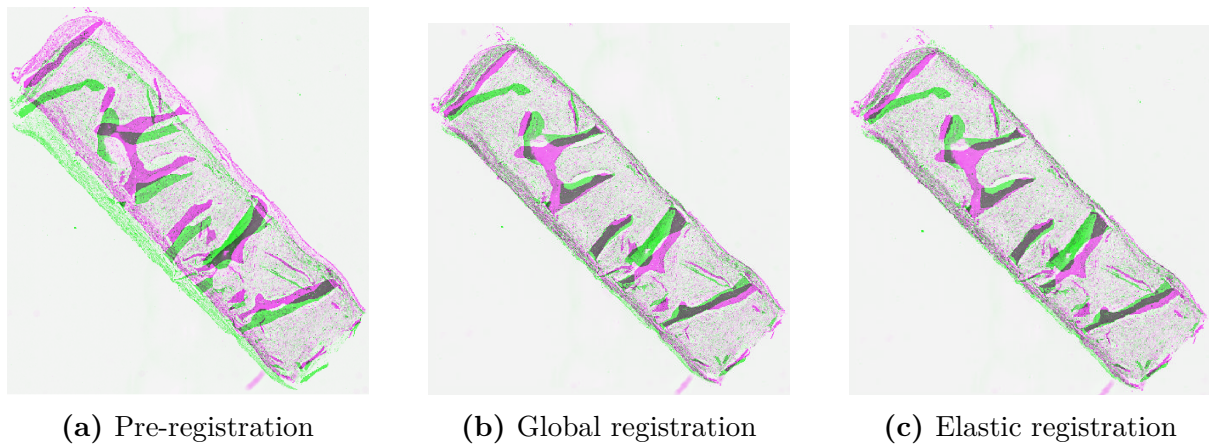


**Figure 5.3:** Comparative overlays of successive images.

### 1.3 Samples Reconstruction

The results of image registration on the lower resolution images were used to register the semantically segmented images. The latter were then stacked to create fully-annotated digital versions of the different samples, with single-cell resolution.

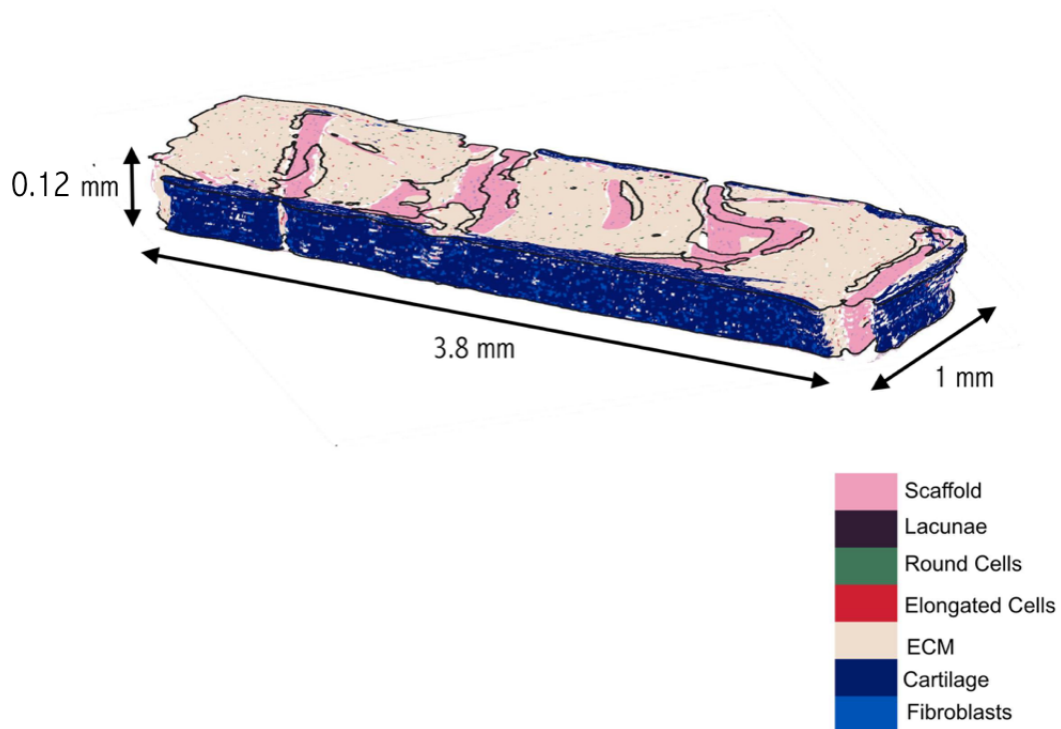


**Figure 5.4:** Fully labeled digital reconstruction of sample R3-T1.

Fully labeled digital reconstructions of the other samples can be found in APPENDIX 3.

## 2 Quantification

The fully-annotated digital versions of the samples obtained with CODA were then used to perform some quantification at both the tissular and the cellular level.

### 2.1 Quantification at the Tissue Level

First, they were used to compute the overall tissue composition and volume of the different samples as well as an in-depth morphological characterization of the scaffolds pieces.

#### 2.1.1 Tissue Content and Volume

The tissue composition of the different scaffolds was computed. To this end, the volume percentage occupied by each of the three tissue types (ECM, Scaffold and Cartilage) inside the different samples was computed.

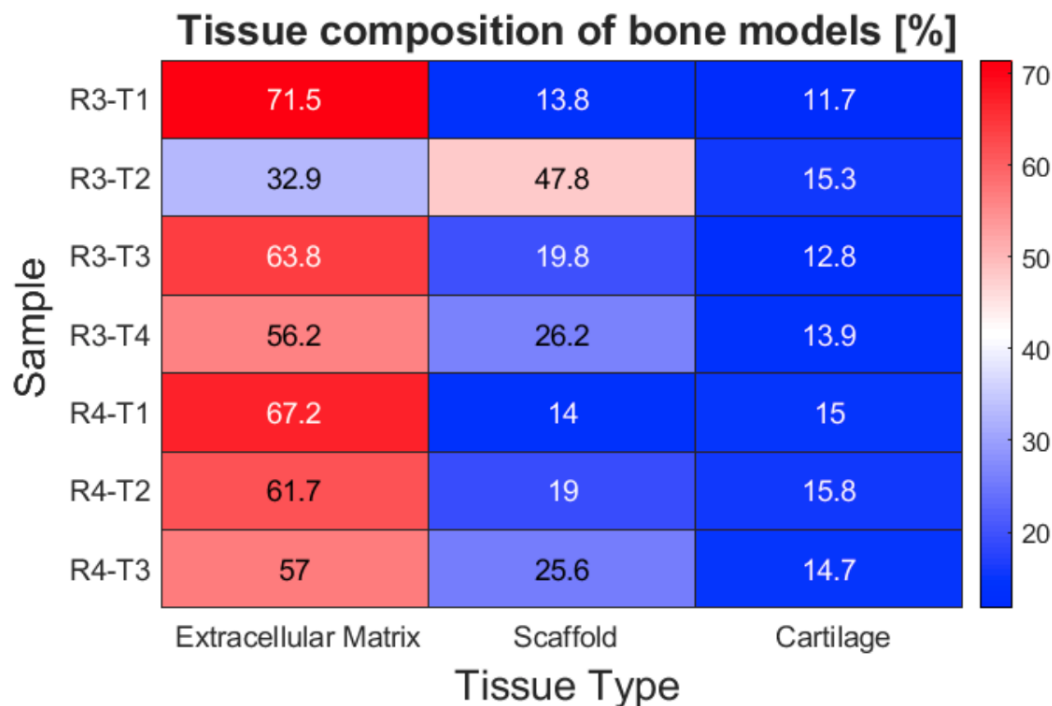


**Figure 5.5:** Tissue composition [%] of the different tissue engineered bone models.

The absolute volume occupied by each tissue type inside each scaffold as well as their overall volume were also calculated.

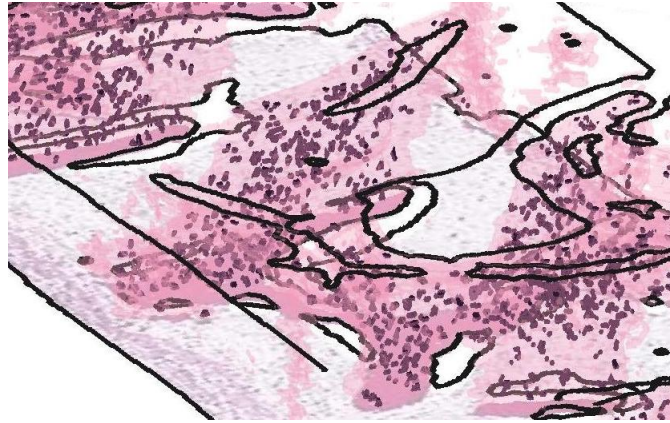


**Figure 5.6:** Zoom in on the lacunae inside the bovine bone scaffold in sample R3-T1.

	R3T1	R3T2	R3T3	R3T4	R4T1	R4T2	R4T3	Mean Value
ECM Volume	258	102	191	195	296	331	219	227
Scaffold Volume	50	149	60	91	61	102	98	87
Cartilage Volume	42	47	39	48	66	85	56	55
Total Volume	360	311	299	346	440	536	384	382

**Table 5.2:** Tissue volume [ $10^{-3}\text{mm}^3$ ] of the different tissue engineered bone models.

Cartilage content seems to be rather consistent across samples in comparison with ECM and scaffold contents. Indeed, there is only a 25% change between the highest and the lowest values of cartilage content while there are respectively a 54% and a 71% change between the highest and the lowest values of ECM and scaffold content.

On the other hand, in terms of absolute value, the total tissue volume also seems to be quite steady across samples: its mean value is  $382 \times 10^{-3} \text{ mm}^3$  with a normalized standard deviation of 22%.

Then, the mean porosity of the scaffolds inside each sample was computed.

	R3T1	R3T2	R3T3	R3T4	R4T1	R4T2	R4T3
Scaffold Porosity [%]	3.8	3.9	2.7	3.8	3.5	3.6	3.7

**Table 5.3:** Mean Scaffold porosity in each sample.

Scaffold porosity is very consistent across samples, with a mean value of 3.57% and a normalized standard deviation of 11.40%. The only exception seems to be the third sample whose scaffold porosity is largely below this mean value.

### 2.1.2 Morphological Characterization of Scaffold Pieces

A morphological characterization of the different pieces of scaffold inside the samples was also performed. To this end, the volume, solidity and extent of each scaffold piece in

each sample were computed.

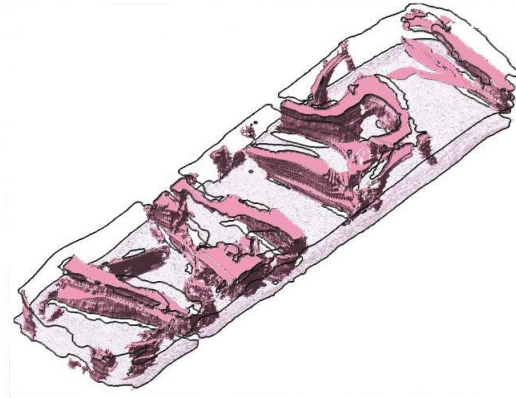


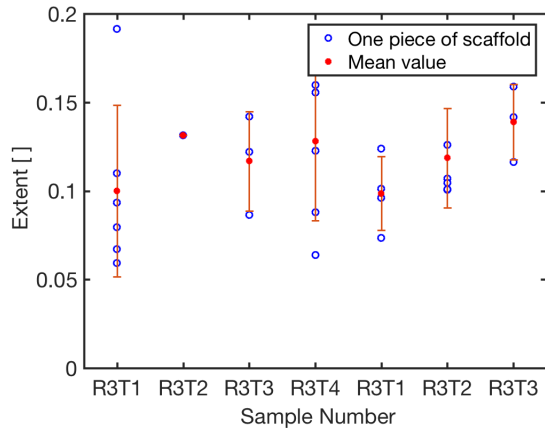
**Figure 5.7:** Top view of the bovine trabecular bone scaffold pieces in samples R3-T1.

Results for the first sample can be found in TABLE 5.4, while results for the other samples can be found in APPENDIX 4.

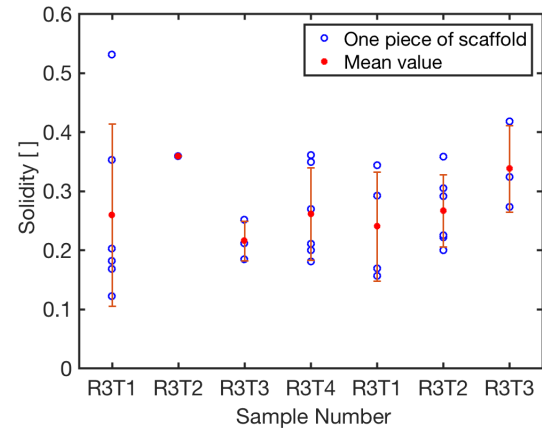
Scaffold Piece	Volume [ $10^{-3}\text{mm}^3$ ]	Extent [%]	Solidity [%]
1	1	7.9	35.3
2	14	9.3	16.8
3	15	11.0	20.2
4	9	6.7	12.1
5	3	5.9	18.1
6	3	19.2	53.1

**Table 5.4:** Morphological assessment of scaffold pieces in sample R3T1.

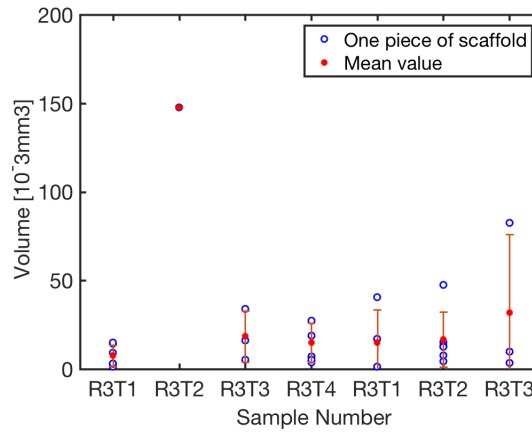
The morphological characterization results for each sample are summarized in FIGURE 5.8.



(a) Extent of the scaffold pieces and the mean extent value of a scaffold piece in each sample.



(b) Solidity of the scaffold pieces and the mean solidity of a scaffold piece in each sample.



(c) Volume of the scaffold pieces and the mean volume of a scaffold piece in each sample.

**Figure 5.8:** Morphological characterization of scaffold pieces inside each sample.

## 2.2 Quantification at the Cell Level

Secondly, their respective digital annotated volumes were used to quantify cellular content inside the different samples.

However, in order to refine and validate the cell detection performed by the CNN model, a method to accurately and reliably detect cell nuclei on H&E histological sections was first tested and implemented.

### 2.2.1 Nuclei Detection on Histological Sections

The detection method relies on the extraction and the filtering of the hematoxylin channel from original H&E images using color deconvolution. Peak intensity detection is then used to find the nuclei positions, corresponding to the intensity maximums in the

filtered hematoxylin channel images.

Different ways of implementing this method were tested and compared on a first testing image. The technique that provided the best outcome was then selected and its results were validated on another validation image.

### 2.2.1.1 Color Deconvolution

A color deconvolution algorithm was implemented for a random  $501 \times 821$  testing H&E histological section with 150 cells.

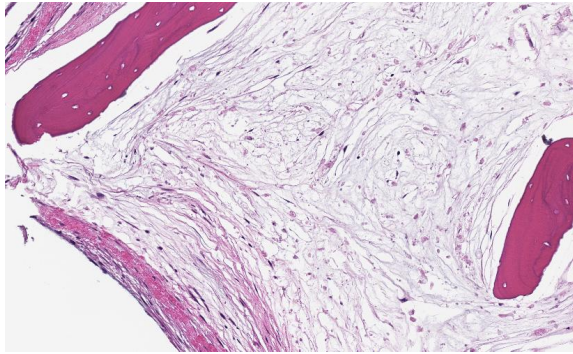
Different ways of choosing the staining matrix were investigated: using kmeans clustering, using either one of the two default matrices from the *Color Deconvolution 2* plugin in Image J or using visual inspection.

The gray-level intensity hematoxylin channel images obtained with the four different staining matrices can be observed in FIGURE 5.9.

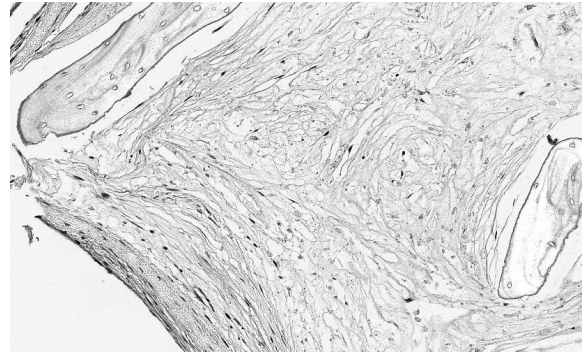
The best image seems to be the one produced with the staining matrix obtained by visual inspection. Indeed, in comparison with the others, FIGURE 5.9e seems the closest to what would actually be the hematoxylin channel of the image. Nuclei appear more contrasted with the ECM while the scaffold and the cartilage layer are less visible.<sup>1</sup> However, results with the second H&E default staining matrix also appear to be suitable so detection results of each method will need to be compared to make the appropriate choice.

---

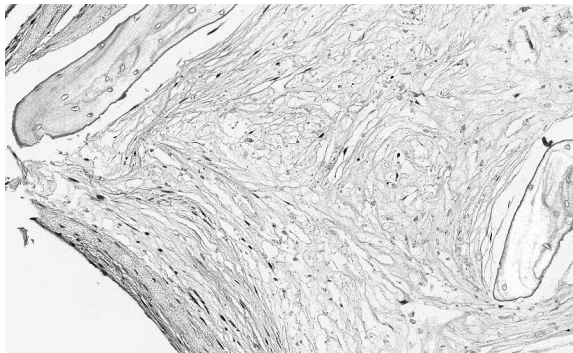
<sup>1</sup>In H&E, hematoxylin stains the cell nuclei in blue and eosin stains the ECM and the cell cytoplasm in pink, while other structures take different shades resulting from the combination of the two stains[64]



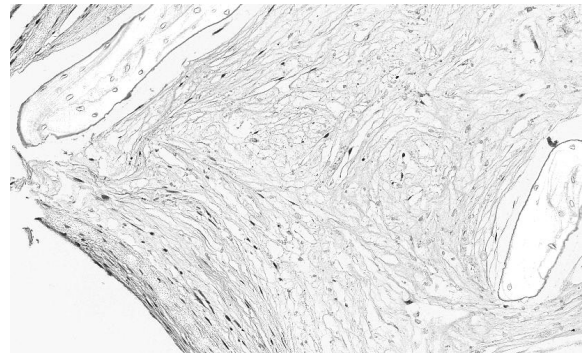
(a) Original RGB tissue section image



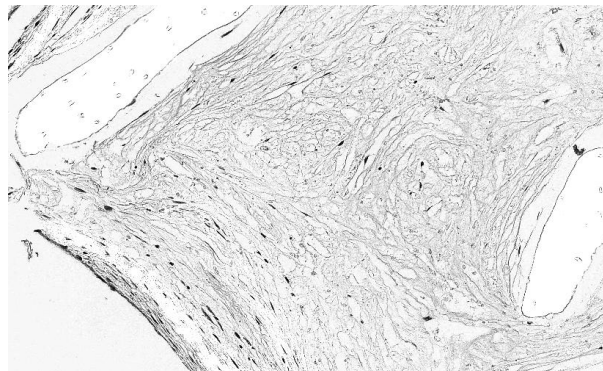
(b) He channel image using kmeans s.m



(c) He channel image using H&E default s.m



(d) He channel image using H&E2 default s.m



(e) He channel image using visually determined s.m

**Figure 5.9:** Comparison of hematoxylin channel images obtained using color deconvolution with different staining matrices. (He : hematoxylin, s.t : staining matrix)

### 2.2.1.2 Filtering

Filtering of the hematoxylin channel images was then used to smooth the images and reduce their noise.

Once again, different techniques were used : subtraction of the average filtered image from the Gaussian filtered image (technique 1), a median filter followed by a Gaussian



filter (technique 2) or the same filtering as combination 1 but followed by a Gaussian filter (technique 3).

FIGURE 5.10 regroups the results of the different filtering techniques on the inverse of FIGURE 5.9e.

It appears that the filtering combination with the most interesting outcome is the first one. Indeed, with the second technique, it is impossible to distinguish what would resemble actual cell nuclei while nuclei seem to have a smaller intensity in the image resulting from the third technique in comparison with the image from the first. Therefore, it seems like the best filtering choice would be the first combination, but once again, quantitative results will be used to verify this intuitive choice.

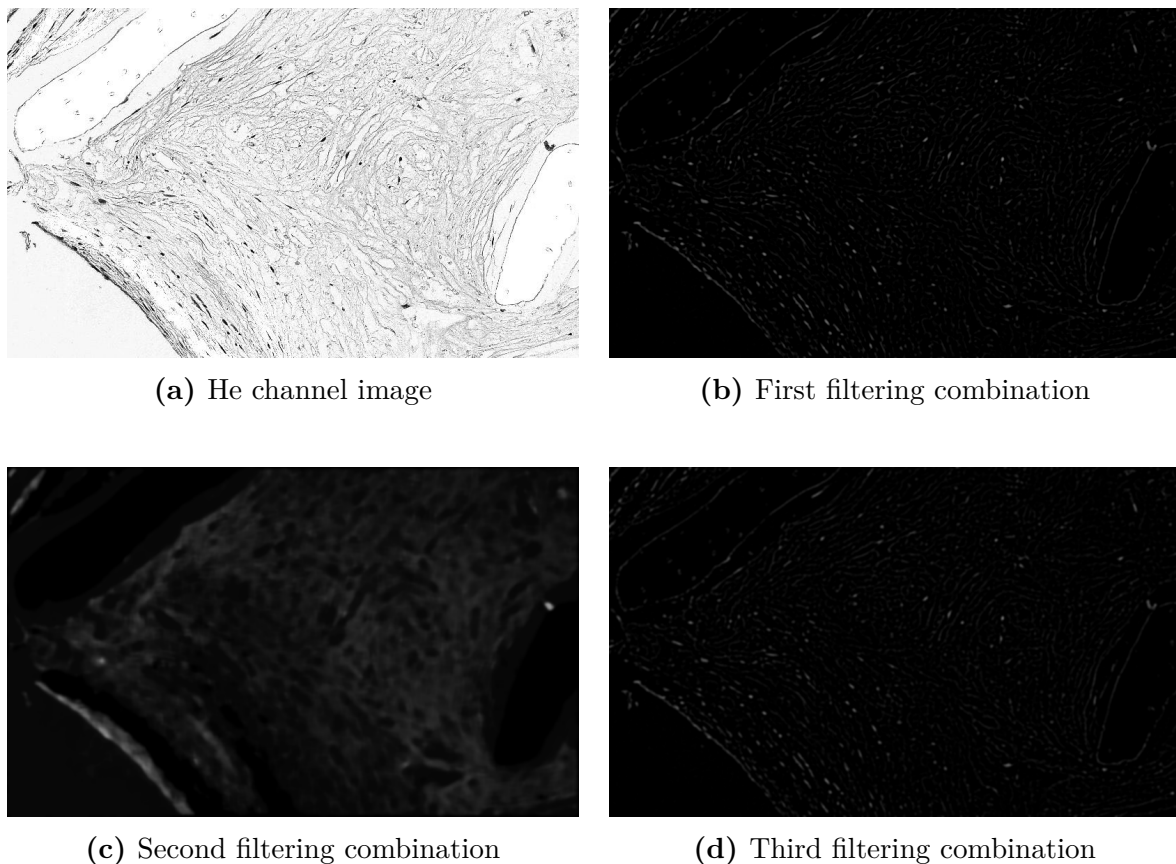


**Figure 5.10:** Comparison of the results using different filtering combinations on the inverse of the hematoxylin channel image obtained with the visually determined staining matrix.

### 2.2.1.3 Peak Intensity Detection and Testing

Cell nuclei positions were then determined as the local intensity maxima in the filtered images.

This was done for each hematoxylin channel image and each filtering technique. Two performance measures, the percentage of correctly detected nuclei and the percentage of false positive, were computed for each of these combinations. Results can be found in

TABLES 5.5 and 5.6.

	Kmeans s.m	H&E default s.m	H&E2 default s.m	Visually determined s.m
Filtering Technique 1	74	69.33	58.67	88.67
Filtering Technique 2	12.67	14.67	4.67	9.33
Filtering Technique 3	44.67	39.33	30	53.33

**Table 5.5:** Percentage of correctly detected cells for each combination of staining matrix and filtering technique on the 150 cells of the testing image. [%]

	Kmeans s.m	H&E default s.m	H&E2 default s.m	Visually determined s.m
Filtering Technique 1	54.67	54	10	11.33
Filtering Technique 2	20	18.67	6.67	4.67
Filtering Technique 3	8.67	6.67	0	3.33

**Table 5.6:** Percentage of false positive for each combination of staining matrix and filtering technique on the 150 cells of the testing image. [%]

With a percentage of correctly detected cells of 88.67% and a rate of false positive of 11.33%, the combination of color deconvolution using the visually determined matrix and the first filtering technique is, as expected, the combination giving the most interesting results.

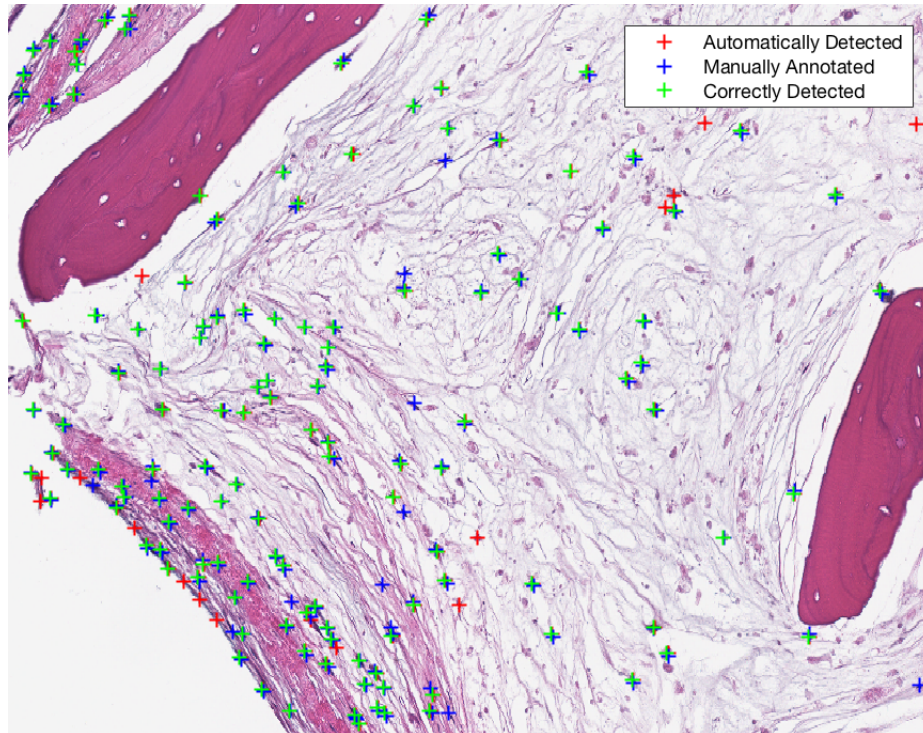


**Figure 5.11:** Visual representation of the manually and automatically detected cells on the testing image (150 cells).

#### 2.2.1.4 Validation

The method previously determined (that is color deconvolution performed via a staining matrix determined by visual inspection in combination with the first filtering technique) performed correctly on the testing image. However, to verify its reliability on other images, its performances were evaluated on another randomly selected image. On a random  $501 \times 821$  image with 388 cells, the method was able to automatically detect 85.19% of the cells correctly with a false positive rate of 12.73%. Taking into account the difficulty of detecting the cells even for the trained eye and the large presence of noise in the images, these results were judged satisfactory.

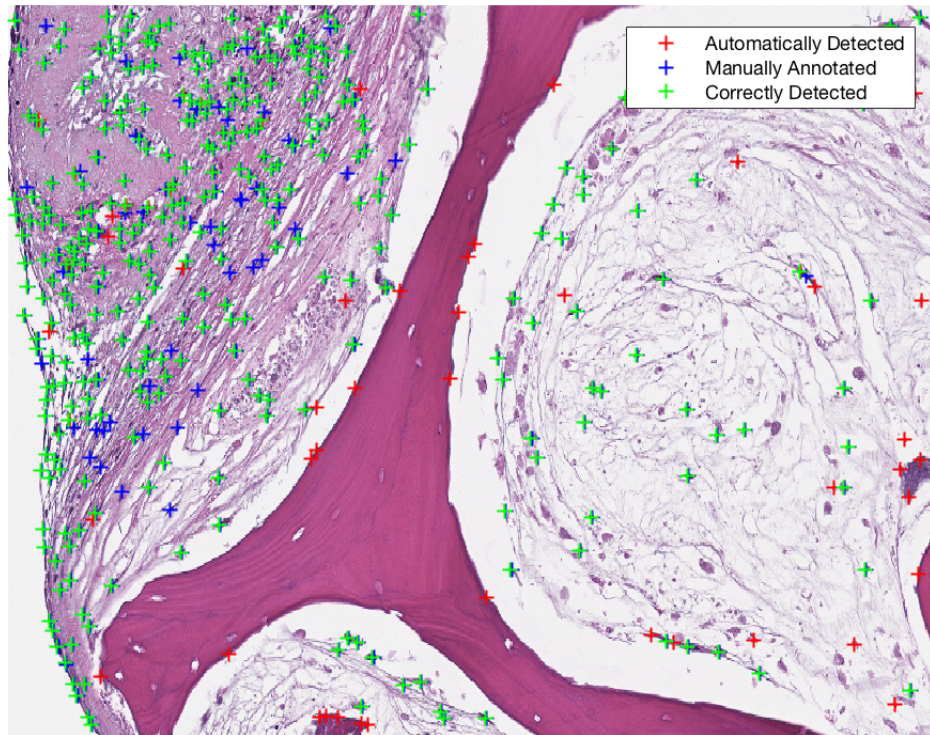


**Figure 5.12:** Visual representation of the manually and automatically detected cells on the validation image (388 cells).

### 2.2.2 Cellular Content

Once the cell detection method had been developed and tested, it was combined with the CNN classification to compute cellular content in the different samples.

Cell count for each cell subtype were computed by combining the cell subtype data from the multiballed 3D versions of the samples with the coordinates obtained via the cell detection algorithm.

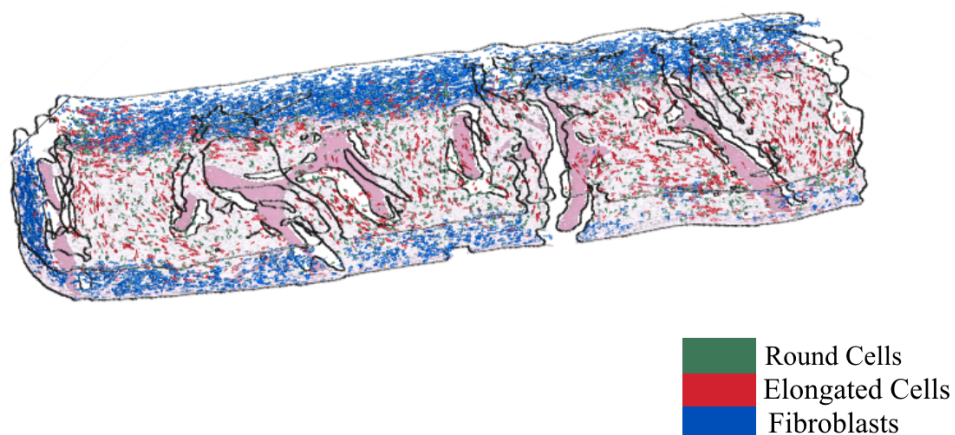


**Figure 5.13:** Detected cells inside sample R3-T1.

For each cell subtype (*i.e* fibroblasts, elongated cells and round cells) in each sample, a total bulk cell count was computed.

Sample	Total Count	Fibroblasts Count	Round Cells Count	Elongated Cells Count
R3T1	10 237	2 663	5 784	1 790
R3T2	9 667	3 907	4 317	1 443
R3T3	12 399	5 368	5 602	1 429
R3T4	11 302	5 968	4 477	857
R4T1	17 327	5 983	8 166	3 178
R4T2	19 631	6 739	9 728	3 164
R4T3	20 413	7 134	10 034	3 245

**Table 5.7:** Cell count, total and for each cell subtype, in the different samples.

The bulk cell density and cell densities in the ECM and the cartilage were also computed in the different samples.

Sample	Bulk	Fibroblasts in Cartilage Layer	Round Cells in ECM	Elongated Cells in ECM
R3T1	28	63	22	7
R3T2	31	83	42	14
R3T3	41	138	29	7
R3T4	33	124	23	4
R4T1	39	91	28	11
R4T2	37	79	29	10
R4T3	53	127	46	15

**Table 5.8:** Cell densities [cells/ $10^{-3}\text{mm}^3$ ], in bulk and in the different tissue subtypes, inside the different samples

Fibroblasts are generally less in absolute number (mean value of 5395 cells) than round cells (mean value of 6873 cells) although they are actually much more densely present in their corresponding tissue subtype ( $100.83\text{ cells}/10^{-3}\text{mm}^3$  on average compared to  $31.40\text{ cells}/10^{-3}\text{mm}^3$  on average). On the other hand, elongated cells have the least average count (2158 cells) and the least average density ( $9.73\text{ cells}/10^{-3}\text{mm}^3$ ) out of the three cell subtypes.

It also appears that the total cell count varies more across samples (mean value of 14 425 cells and normalized standard deviation of 31.69%) than the bulk density (mean value of  $37.54\text{ cells}/10^{-3}\text{mm}^3$  and normalized standard deviation of 22.08%) that is more stable.

# Chapter 6

## Discussion

In this chapter, quantification results about the tissular and cellular content of tissue engineered bone models for the study of breast and prostate cancer metastasis obtained and presented in the previous section are discussed with respect to the literature. This is done with the ultimate goal of deriving new leads in the development of more accurate tissue engineered bone models.

However, although its key contributions are highlighted, the study at its current state presents important limitations, which are presented and summarized in this chapter. In this context, the chapter ends on the introduction of perspectives for future work.

### 1 Quantification

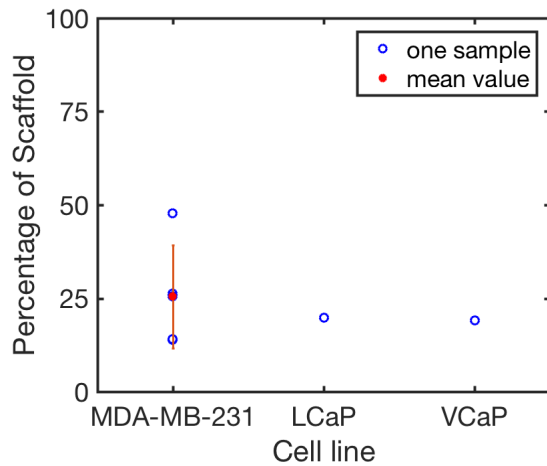
Quantification results about the tissular and cellular content of tissue engineered bone models for the study of breast and prostate cancer metastasis were obtained and presented in the previous section. They include information about the content in each tissue subtype of each sample, a morphological characterization of the different scaffold pieces in each sample as well as information about the cellular contents and densities in each detected cell subtype for each sample.

All samples were obtained using a standardized procedure (detailed in SECTION 3) developed in the Laboratory for Stem Cells and Tissue Engineering from Columbia University. The main difference between samples lies in the choice of the infused cancer cell line. Indeed, five out of the seven samples were infused with the MDA-MB-231 cell line (breast cancer) while one was infused with the LnCaP cell line (prostate cancer) and one was infused with the VCaP cell line (prostate cancer). In the literature, each type of cancer is associated with a different metastatic phenotype. As it has been explained in SECTION 2.4, breast cancer metastasis tend to be *osteolytic* (mainly associated with bone destruction) while prostate cancer metastasis tend to be *osteoblastic* (mainly associated with woven bone formation). Therefore, it has been decided to display the quantification results of the different samples in function of the cell line they were infused with. It is hoped that by doing so, results on the tissue engineered models would be in accordance with what has been reported in the literature with other metastasis models.

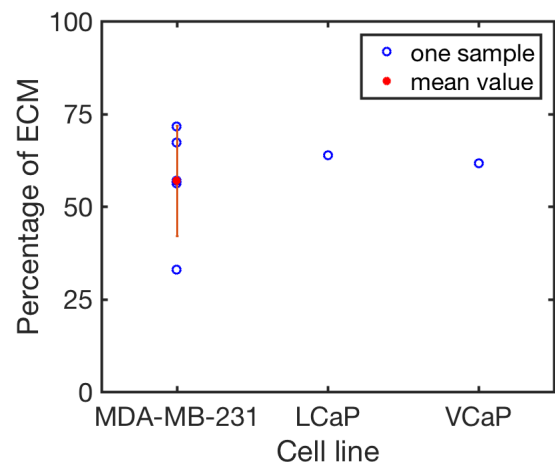
## 1.1 Quantification at the Tissular Level

### 1.1.1 Tissue Content

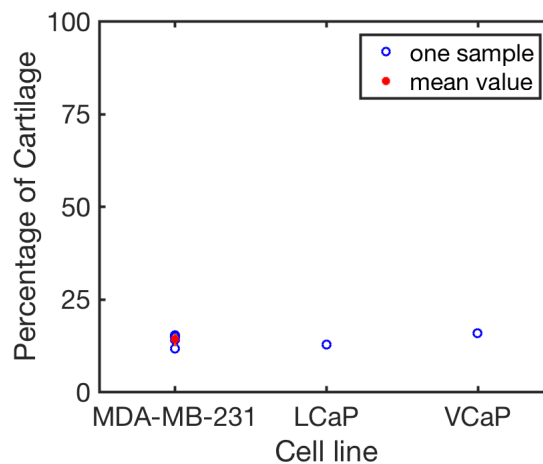
Therefore, we began by displaying the content in each tissue subtype in function of the cancer cell line for each sample.



(a) Percentage of scaffold inside samples in function of cancer cell line.



(b) Percentage of ECM inside samples in function of the cancer cell line.



(c) Percentage of cartilage in function of the cancer cell line.

**Figure 6.1:** Percentage of tissue inside the samples in function of the cancer cell line.

It appears that, on average, the five samples infused with breast cancer cells are associated with a higher percentage of scaffold than the two other samples infused with either one of the two prostate cancer cell lines while the percentage of ECM is higher in the samples with prostate cancer cells than in the samples with breast cancer cells. On the other hand, the percentage of cartilage appears relatively stable across samples, regardless of the cancer cell line they were infused with.

These observations seem to be in contradiction with what can be found in the literature.

Indeed, prostate metastasis in the bone have been associated with the osteoblastic phenotype, which is characterized by the formation of woven bone.[3][30] This immature form of bone is characterised by a network of randomly arranged collagen fibers.[65] An histological section containing woven bone can be observed in FIGURE 6.2.

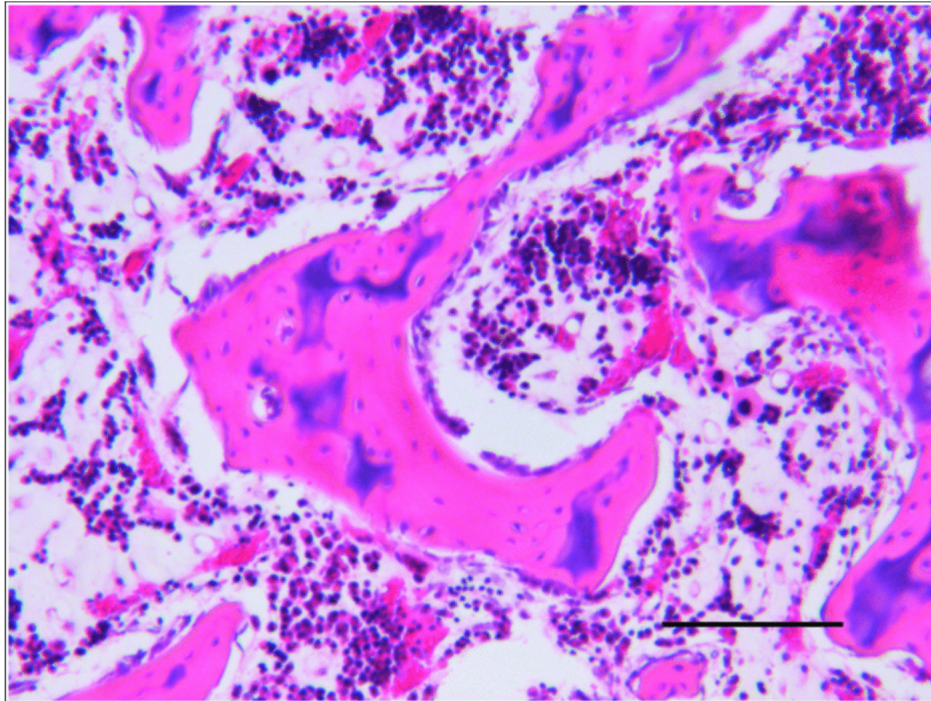
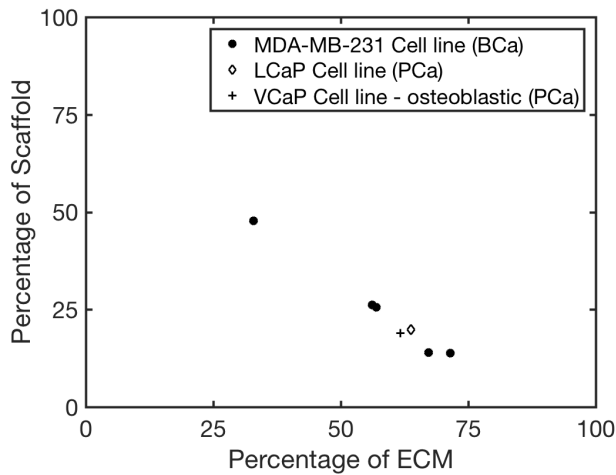


**Figure 6.2:** Micrograph of woven bone. HE stained section of rabbit bone, from the histology slide collection of CAHID, University of Dundee. (Scale bar = 380  $\mu\text{m}$ , 10x) (Taken from [18].)

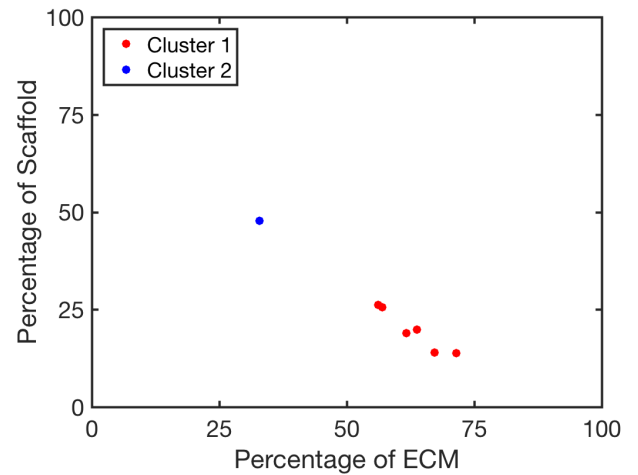
Considering its appearance that is close to the one of trabecular bone, woven bone (if ever present in the samples) would be classified as bovine bone scaffold by the deep learning model. Therefore, one would expect the scaffold percentage to be higher in the samples infused with prostate cancer cells. Especially since breast cancer metastasis is associated with the osteolytic phenotype, which is characterized by bone destruction. [4] These samples infused with breast cancer cells would be also expected to present higher contents of ECM. Indeed, it is likely that the destructed bone matrix would be classified as ECM by the deep learning model.

Although no trend could be directly derived from the tissue percentage graphs, it was hoped that a clustering analysis could help deriving interesting relations between tissue contents. Therefore, the percentage of scaffold in function of the percentage of ECM was displayed for each sample and a k-means clustering analysis with two clusters was performed, as shown in FIGURE 6.3.





(a) Percentage of scaffold in function of the percentage of ECM inside the samples of different cancer cell lines.



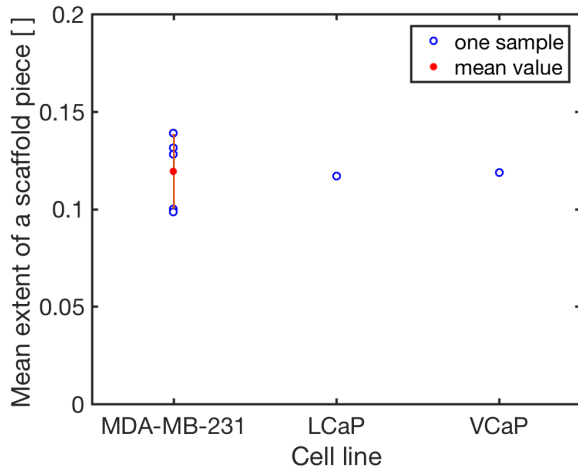
(b) Clusters in the percentage of scaffold in function of the percentage of ECM inside the samples.

**Figure 6.3:** K-means clustering analysis of the percentage of scaffold in function of the percentage of ECM inside the different samples. (2 clusters)

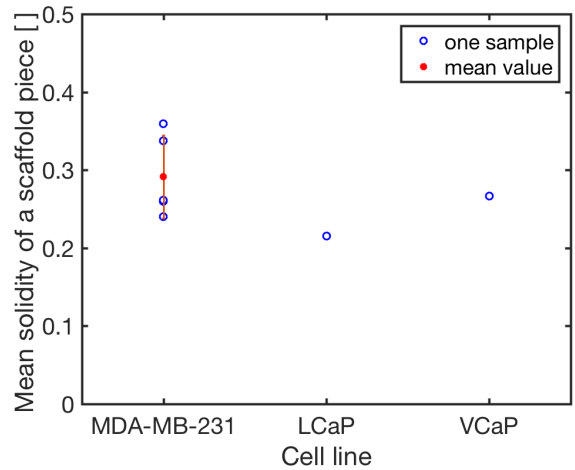
Unfortunately, as expected, it is not possible to draw a parallel between the 2 clusters obtained (respectively associated with high scaffold content and low ECM content and low scaffold content and high ECM content) and any type of cancer cell line.

### 1.1.2 Morphological Characterization of Scaffold Pieces

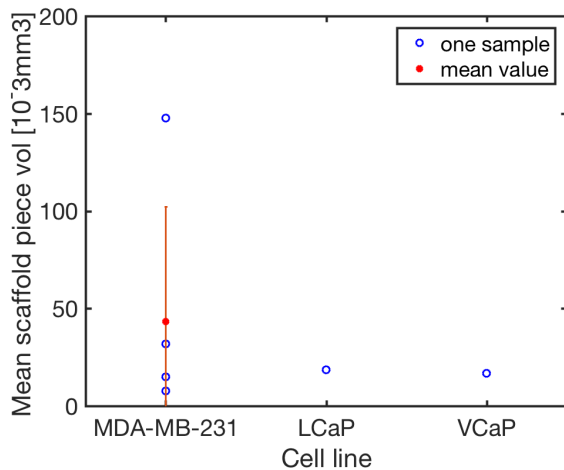
Next, results of the morphological characterization of the scaffold pieces inside the samples were displayed in function of the cancer cell line used. To do so, figures of the mean value of each morphological properties for a scaffold piece inside each sample in function of the cancer cell line used in the sample were created.



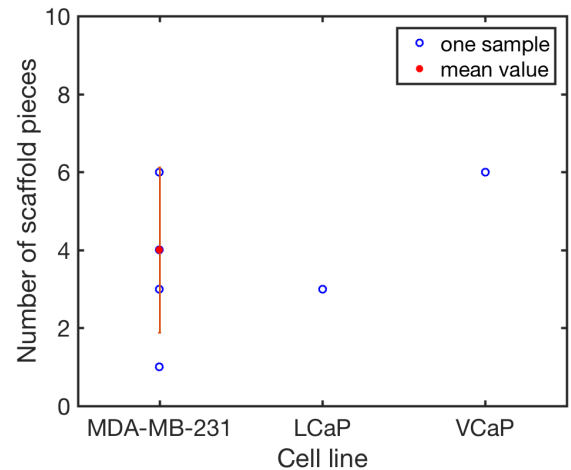
(a) Mean extent of a scaffold piece in a sample in function of the cancer cell line used in the sample.



(b) Mean solidity of a scaffold piece in a sample in function of the cancer cell line used in the sample.



(c) Mean volume of a scaffold piece in a sample in function of the cancer cell line used in the sample.



(d) Mean number of scaffold pieces in a sample in function of the cancer cell line used in the sample.

**Figure 6.4:** Mean morphology of a scaffold piece in a sample in function of the cancer cell line used in the sample.

First, it appears that the mean extent of a scaffold piece is rather constant across samples regardless of the cancer cell line they were infused with. Let us recall that the extent of an object is computed as the ratio between the volume of the object and the volume of its bounding box. This means that, out of the two objects whose bounding boxes are visible in FIGURE 6.5, the more elongated one will have the higher extent.

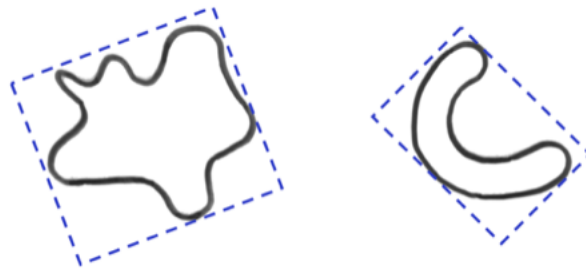


**Figure 6.5:** Bounding boxes. (Taken from [19])

Secondly, the mean solidity of a scaffold piece seems higher in the samples infused with breast cancer cells than in the samples infused with prostate cancer cells. If we recall that solidity of an object is measured as the ratio between its volume and the volume of its convex hull. Therefore, this means that "*solidity measures the extent to which a shape is convex or concave*"[66]. Thus, if solidity is close to one, this means that the object is solid, while if the solidity is less than one, this means that the object has holes or an irregular boundary.



**Figure 6.6:** Shapes and their respective solidity. (Taken from [19])

Considering this definition, the fact that scaffold pieces in samples with breast cancer cells have higher solidity values seems in contradiction with the literature. Indeed, breast cancer metastasis is normally associated with bone destruction. This means that it would thus be associated with scaffold pieces having more irregular boundaries and shapes, as a result of osteoclasts' actions. However, this is not the case here.

The mean volume of a scaffold piece as well as the number of scaffold pieces in each sample have been computed. It appears that samples with breast cancer cells are associated with higher volume on average than samples infused with prostate cancer cells while the presence of cancer cells does not seem to have a particular impact on the number of scaffold pieces. Once again, this seems to be the opposite of what one would expect based on the literature. Indeed, bone formation would be expected to result in less scaffold pieces with a higher volume while bone destruction would produce more pieces with a small volume.

## 1.2 Quantification at the Cellular Level

### 1.2.1 Cellular Content and Cellular Density

Results about cellular content and cellular density in each sample can also be displayed as a function of the cancer cell line infused in the sample.

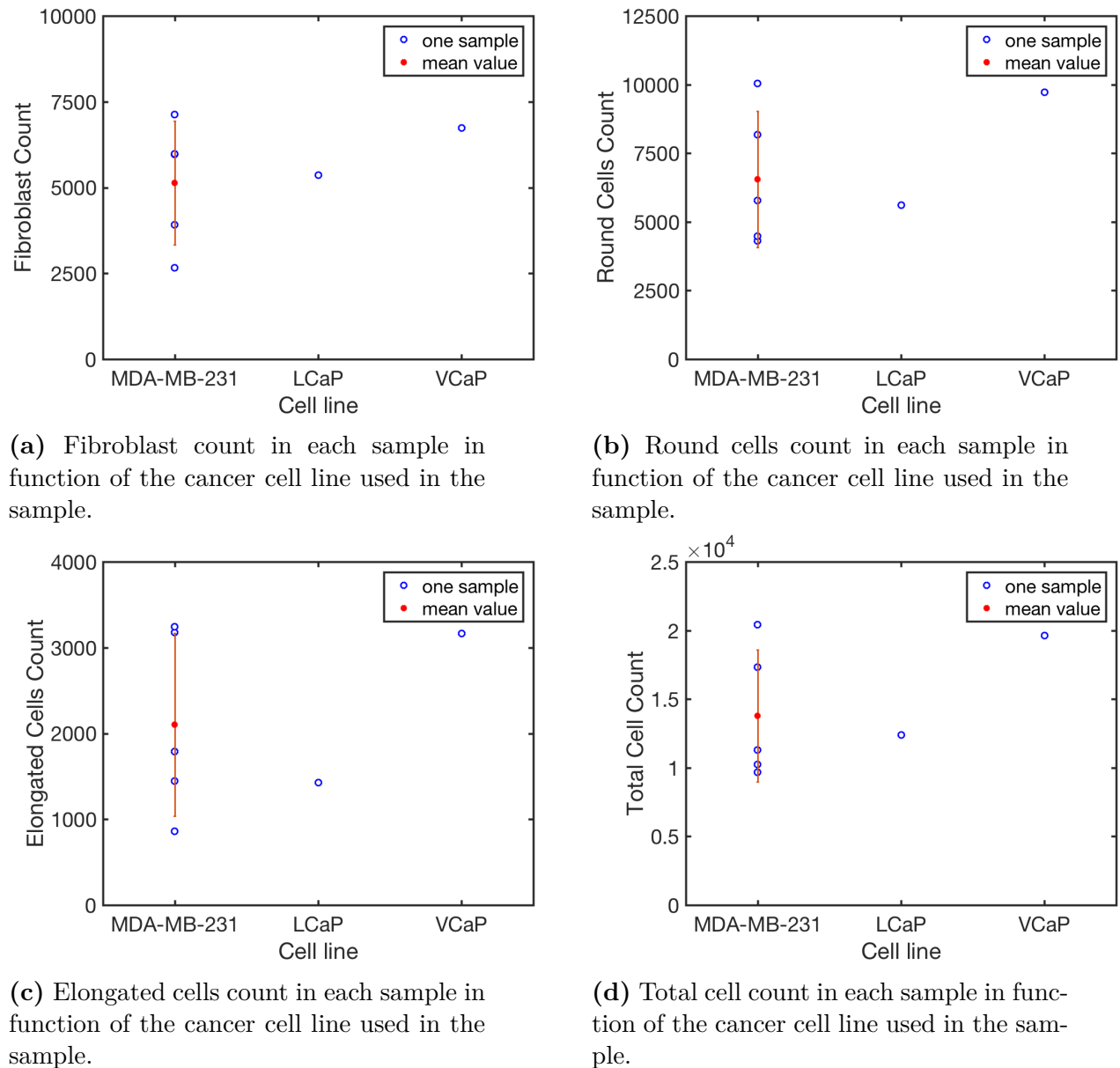
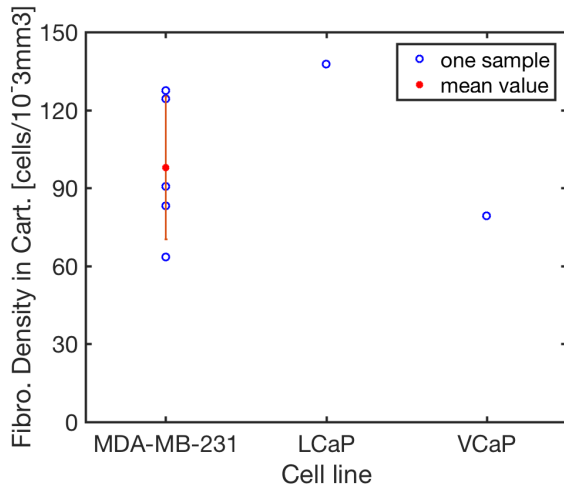
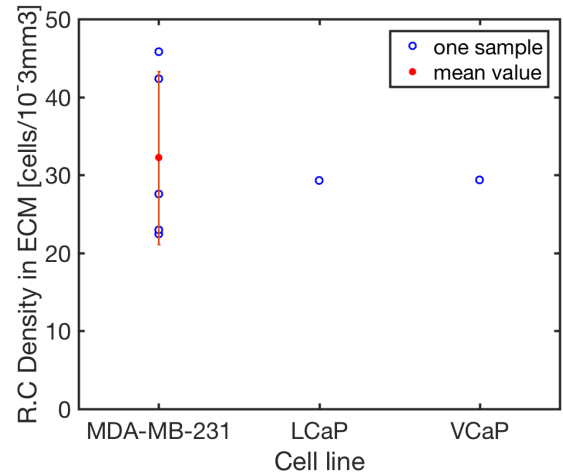


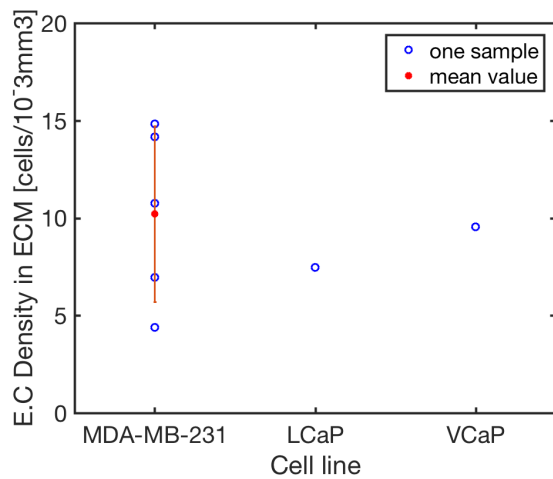
**Figure 6.7:** Cell counts in each sample in function of the cancer cell line used in the sample.



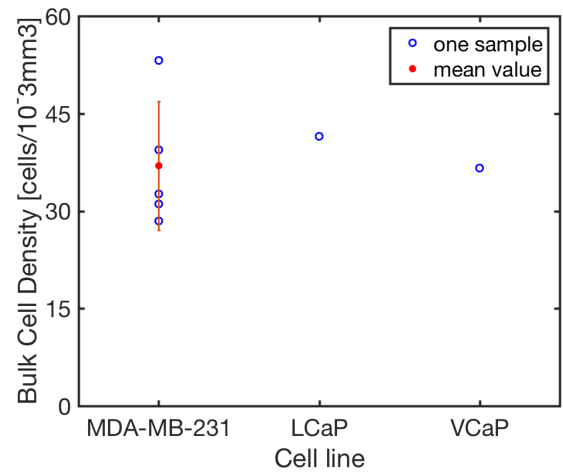
(a) Fibroblast density in the cartilage layer of each sample in function of the cancer cell line used in the sample.



(b) Round cell density in the ECM of each sample in function of the cancer cell line used in the sample.



(c) Elongated cell density in the ECM of each sample in function of the cancer cell line used in the sample.



(d) Bulk cell density in each sample in function of the cancer cell line used in the sample.

**Figure 6.8:** Cell densities in each sample in function of the cancer cell line used in the sample.

These different figures do not seem to contain clear trends in cellular content or density inside samples containing either breast or prostate cancer cells. In particular, samples with breast cancer cells are neither necessarily associated with higher or lower contents in round or elongated cells nor with higher or lower cell densities in round or elongated cells in the ECM in comparison with samples containing prostate cancer cells.

## 2 Limitations and Key Contributions

The different tissular contents and organization results presented throughout the previous sections of this chapter have been shown to contradict what can currently be found in the literature regarding prostate and breast cancer metastasis.

However, there exists a reason that could explain these discrepancies, that is the limited number of samples used in this study. Indeed, a total of seven samples have been used, five of which were infused with the MDA-MB-231 cancer cell line while one was infused with the LCaP cancer cell line and the other with the VCaP cancer cell line. Rigorous conclusions can therefore not be made on such a small batch of samples, especially since there seems to be great variability in between results in samples with breast cancer cells and that only one sample is available for each of the two prostate cancer cell lines. The results presented in this study should therefore be taken for what they are : preliminary results destined to be corroborated by further investigations.

On the other hand, cellular content and cellular density results did not allow for interesting observations. Besides once again the insufficient number of samples, another reason can explain the lack of trend in the data. Indeed, one of the major limitations of this work is that the deep learning model is only capable of distinguishing three types of cells : fibroblasts, elongated cells and round cells. Two of which, elongated and round cells, are not actual cell types but rather cell phenotypes. This is due to the fact that, as non-specialists, we have not been able to reliably distinguish the three bone cell types (*i.e* osteoclasts, osteoblasts and osteocytes) or the three types of cancer cells on the histological sections that we were given. It seems extremely likely that, with the right number of samples and a deep learning model that can distinguish all the different cell types, this type of cellular quantification will provide valuable insight on the behaviour of prostate and breast metastatic cells in these tissue engineered models.

However, these two important limitations should not undermine the fact that this work is the first to attempt such an in-depth characterization of tissue engineered bone models, at the mm scale and with single-cell resolution as well as a three dimensional perspective. Indeed, until now, such samples would mainly be studied by visual inspection in two dimensions and in the range of a hundred  $\mu\text{m}$ . No actual tissular or cellular quantification has ever been performed before on these models. [28][16] That is the use of CODA that made it possible to do so. [17]

## 3 Future work

Therefore, overcoming the limitations introduced in the previous section is a first perspective for future work.

This would thus imply using a more important number of samples in order to make statistically significant conclusions about their tissular and cellular contents.

This would also imply training a new deep learning model that is actually capable of distinguishing the different cell types that are present in the samples. Since it can be challenging to differentiate them solely on the H&E sections, one could combine the information given by these sections with immunohistochemistry, like it has been done in [67].

However, as it has been explained in the introduction, the ultimate goal of this work was to derive new leads on the development of more accurate models for the study of breast and prostate cancer metastasis formation in bones by the comparing the three dimensional structural organization and tissular and cellular contents of state-of-the-art models to the ones of *in vivo* bone tissues harboring metastasis. For now, this dissertation only steps a foot in the right direction by analyzing the tissue engineered models. Nonetheless, for the study to be most complete and insightful, it would be necessary to perform the same quantification on actual human bone tissues.

# Chapter 7

## Conclusions

Bone and prostate cancers are very common and deadly forms of cancer, particularly because of the formation of metastasis in the bone tissue. Their deadliness comes from the fact that the metastasis formation process is still poorly understood, which prevents from finding effective treatments that can limit the spread of the disease. Over the years, different models for the study of metastasis formation have been used, including 2D cultures of cancer cells *in vitro* and *in vivo* animal models, but none of them succeeded at faithfully recapitulating the particularities of human bone microenvironment. Therefore, deriving new insights on the formation of bone metastasis and eventually finding drugs that specifically target this phenomenon would require the development of new biomimetic models. In the last ten years, tissue engineered models have presented themselves as interesting alternatives to conventional 2D cell cultures and animal models. However, even current state-of-the-art tissue engineered constructs still need major improvements to be considered as truly recapitulating tumor features *in vitro*.

In this context, the work developed here aimed at ultimately deriving new leads in the creation of improved tissue engineered models for the study of breast and prostate cancer metastasis by comparing their 3D tissular and cellular contents with the ones of human bone tissues harboring metastasis.

This study made use of CODA [17] to create fully-annotated 3D digital versions of seven tissue engineered bones infused with either breast or prostate cancer cells. Each of these 3D maps had single-cell resolution and a scale ranging over several millimeters. They were then used to perform an in-depth characterization of the samples at the tissular and the cellular level. This characterization namely included the computation of contents in the different identified tissue subtypes and in the different identified cell subtypes as well as a morphological assessment of the trabecular bone matrix.

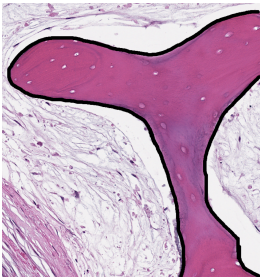
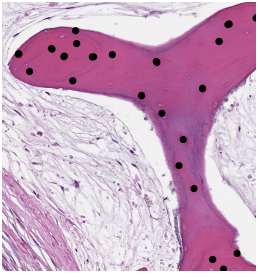
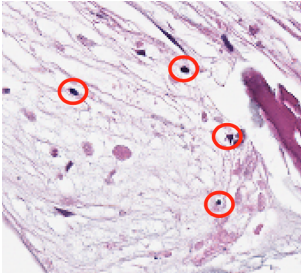
Putting the results of these computations in perspective with the cancer cell line used in the samples, it was possible to make preliminary observations that seemed to be in contradiction with what can be currently found in the literature. However, exploring the different limitations of the study allowed to find potential reasons explaining these discrepancies. Therefore, limitations will need to be investigated and overcome in future work to verify that results are actually in accordance with previous findings.

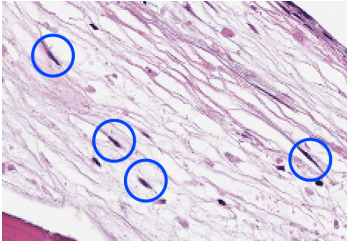
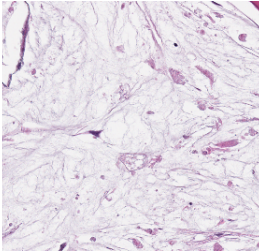
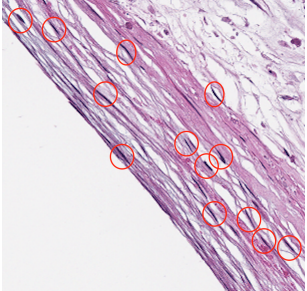
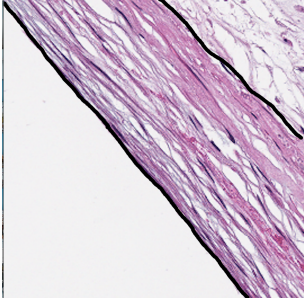


Thus, although this dissertation presents the first attempt ever at an in-depth characterization of tissue engineered bone models at the millimeter scale and with single-cell resolution, it is only a step in the right direction. Indeed, its ultimate goal will only be fulfilled once its limitations will be overcome and the same study is performed on human bone tissues harboring breast and prostate metastasis.

# Appendix A

## 1 Identified Tissue Subtypes

Name	Description	Example on H&E section
Scaffold	Decellularized bovine trabecular bone, used as a scaffold. [68]	
Lacunae	Small cavities inside the scaffold in which the bovine bone cells were sitting before decellularization. [69]	
Round Cells	First phenotype identified among differentiated stem cells.	

Elongated Cells	Second phenotype identified among differentiated stem cells.	
ECM	New osteogenic ECM, rich in type I collagen and bone sialoprotein. [68]	
Fibroblasts	Spindle-shaped cells. [70]	
Cartilage	Connective tissue composed of cartilage cells scattered inside a glycoprotein matrix strengthened with collagen fibers. [71]	

**Table A.1:** Identified Tissue Subtypes.

## 2 Common Deep Learning Model Errors

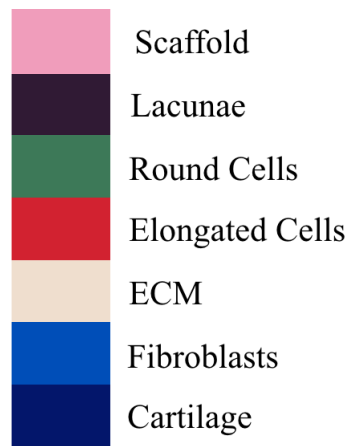
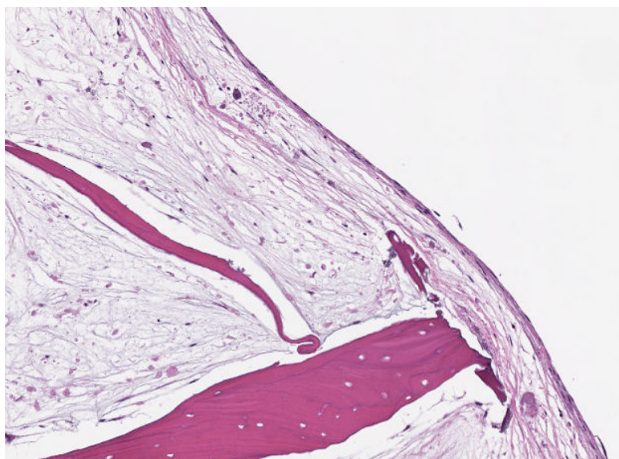
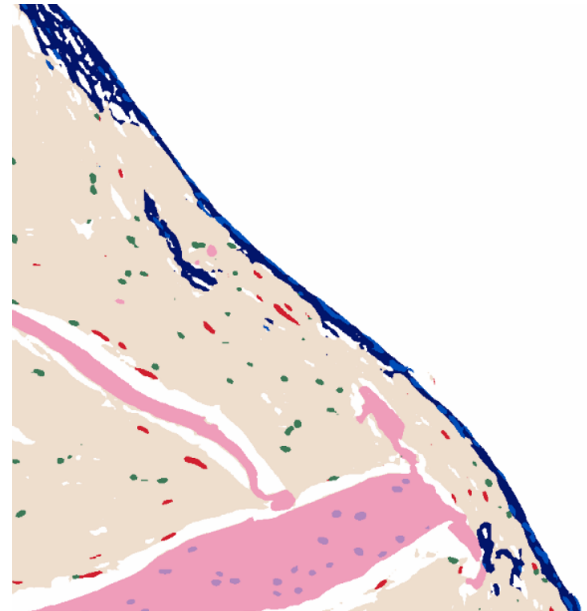


**Figure A.1:** Semantic segmentation legend.

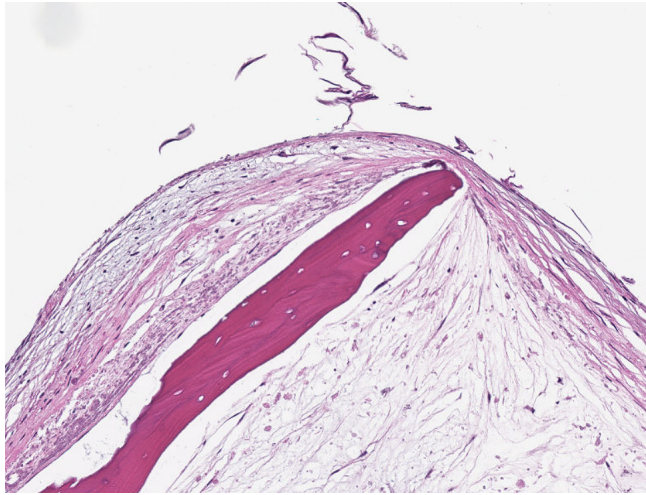


(a) Histological section.

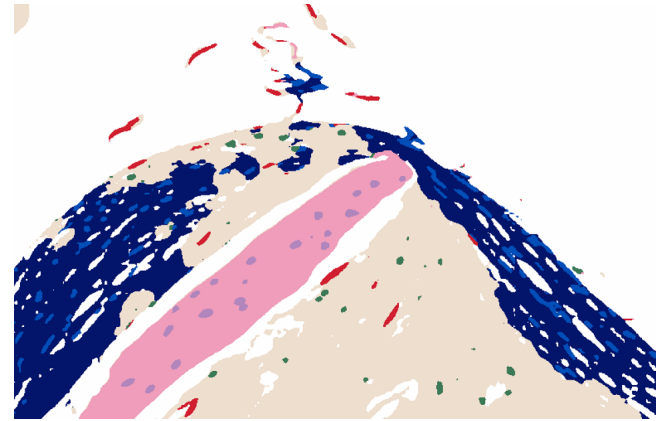


(b) Semantically segmented section.

**Figure A.2:** CNN model struggles at distinguishing ECM and cartilage while it tends to label round or elongated cells as ECM. (Legend in FIGURE A.1)

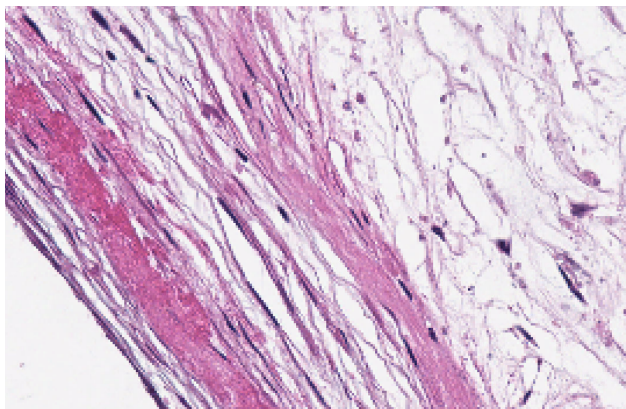


(a) Histological section.

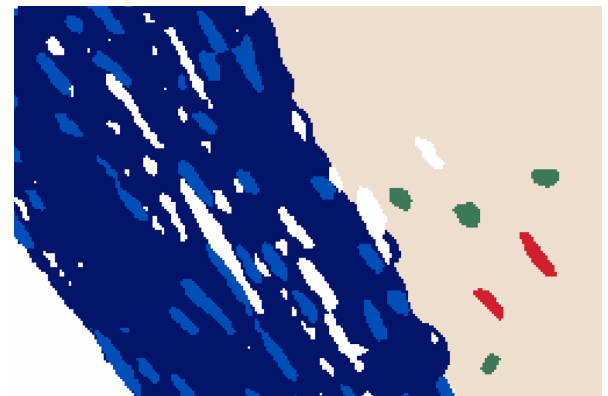


(b) Semantically segmented section.

**Figure A.3:** CNN model often mistakes whitespace and cartilage for ECM. (Legend in FIGURE A.1)



(a) Histological section.



(b) Semantically segmented section.

**Figure A.4:** CNN model tends to exaggerate fibroblasts boundaries in cartilage layer while it labels a lot of whitespace as ECM. (Legend in FIGURE A.1)

### 3 Labeled Digital Reconstructions

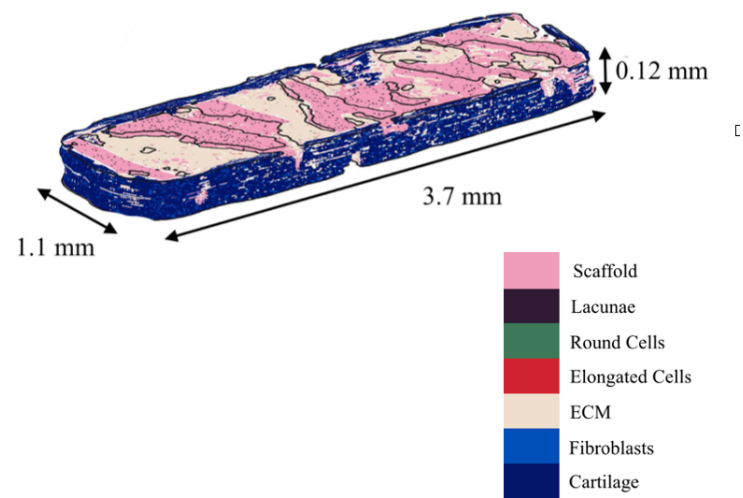


**Figure A.5:** Fully labeled digital reconstruction of sample R3-T2.

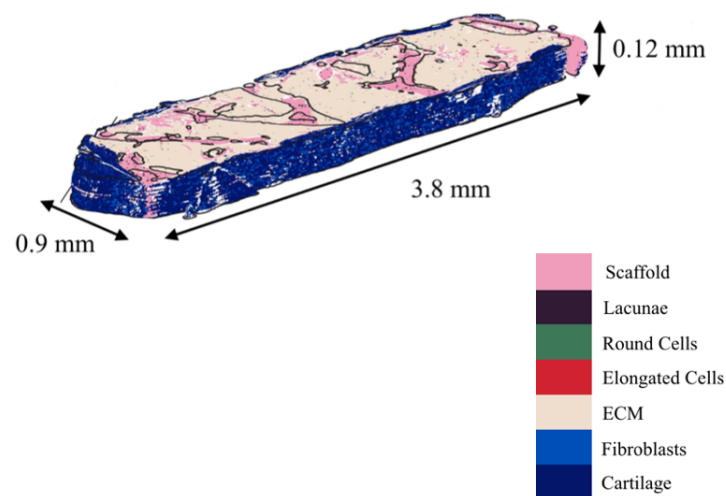


**Figure A.6:** Fully labeled digital reconstruction of sample R3-T3.

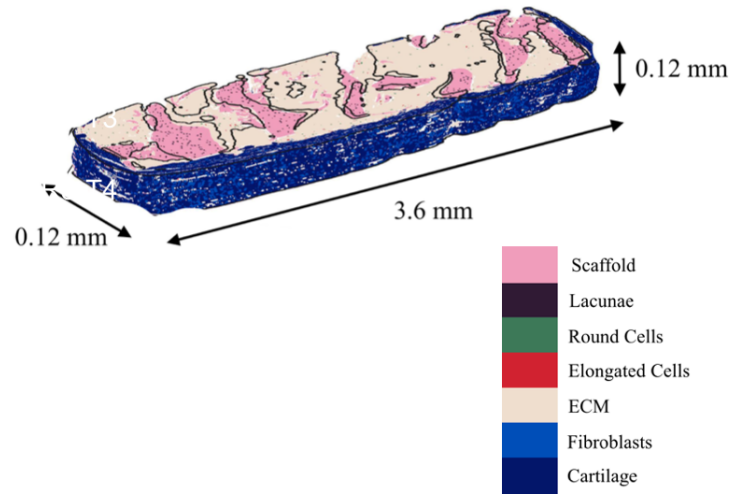


**Figure A.7:** Fully labeled digital reconstruction of sample R3-T4.

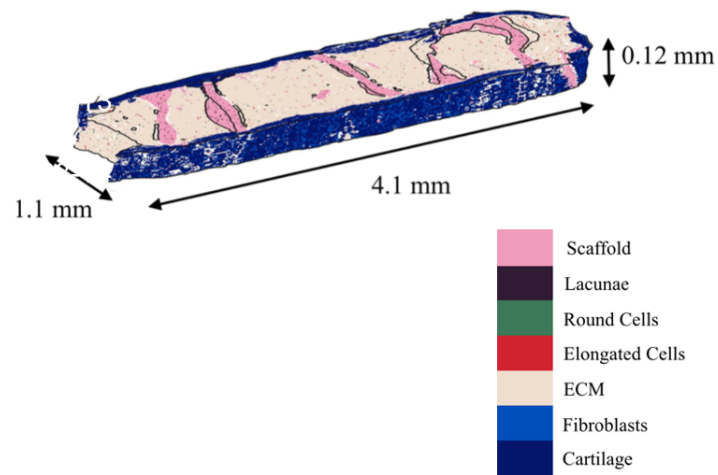


**Figure A.8:** Fully labeled digital reconstruction of sample R4-T1.

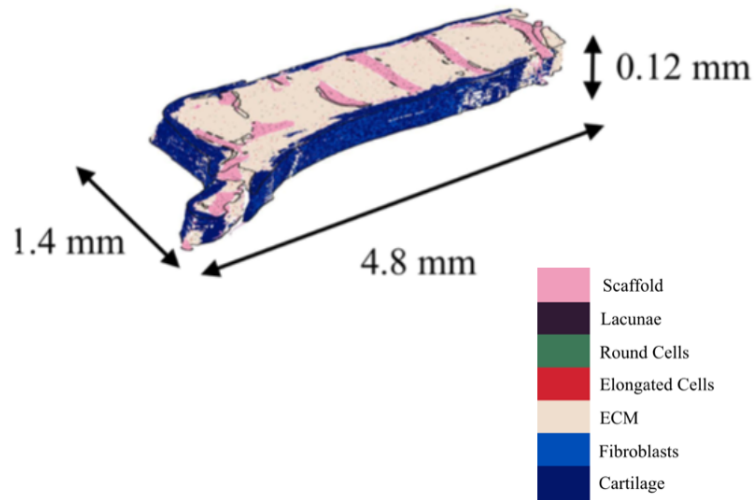


**Figure A.9:** Fully labeled digital reconstruction of sample R4-T2.

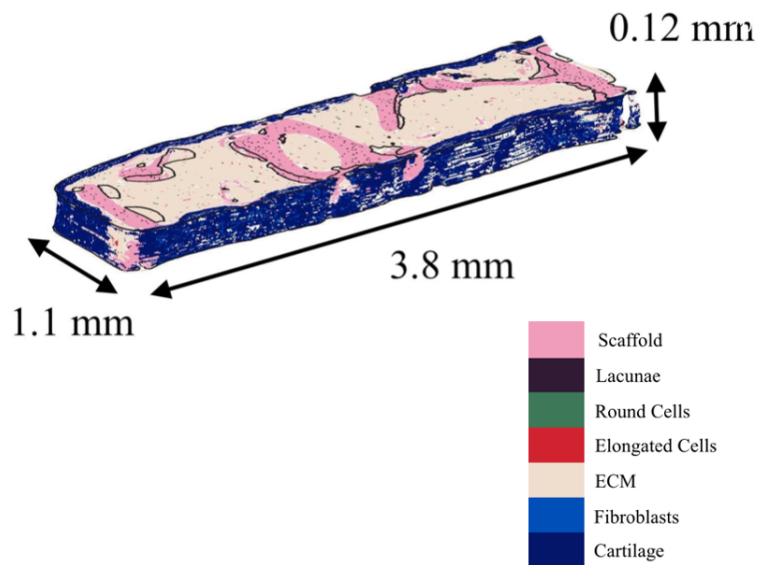


**Figure A.10:** Fully labeled digital reconstruction of sample R4-T3.



## 4 Scaffold Characterization Results

Scaffold Piece	Volume [ $10^{-3}\text{mm}^3$ ]	Extent [%]	Solidity [%]
1	147	13	36

**Table A.2:** Morphological assessment of scaffold pieces in sample R3T2.

Scaffold Piece	Volume [ $10^{-3}\text{mm}^3$ ]	Extent [%]	Solidity [%]
1	16	12	21
2	34	9	18
3	5	14	25

**Table A.3:** Morphological assessment of scaffold pieces in sample R3T3.

Scaffold Piece	Volume [ $10^{-3}\text{mm}^3$ ]	Extent [%]	Solidity [%]
1	27	18	35
2	19	12	20
3	7	6	18
4	3	9	21
5	27	16	27
6	5	16	36

**Table A.4:** Morphological assessment of scaffold pieces in sample R3T4.

Scaffold Piece	Volume [ $10^{-3}\text{mm}^3$ ]	Extent [%]	Solidity [%]
1	40	7	16
2	17	10	17
3	1	10	34
4	1	12	29

**Table A.5:** Morphological assessment of scaffold pieces in sample R4T1.

Scaffold Piece	Volume [ $10^{-3}\text{mm}^3$ ]	Extent [%]	Solidity [%]
1	47	11	20
2	4	17	36
3	8	10	29
4	15	10	22
5	13	13	30
6	12	10	23

**Table A.6:** Morphological assessment of scaffold pieces in sample R4T2.

Scaffold Piece	Volume [ $10^{-3}\text{mm}^3$ ]	Extent [%]	Solidity [%]
1	10	14	42
2	3	16	32
3	83	11	27

**Table A.7:** Morphological assessment of scaffold pieces in sample R4T3.

# Bibliography

- [1] Chapter 3 - physiology of bone. In J Allgrove and N.J Shaw, editors, *Calcium and Bone Disorders in Children and Adolescents, second Revised Edition*, volume 28, pages 33–35. Endocr Dev, Karger, Basel.
- [2] Amy Harwell Robin Hopkins Joel Kaufmann Mike LeMaster Philip Matern Katie Morrison-Graham Devon Quick Jon Runyeon Oregon State University Lindsay M. Biga, Sierra Dawson. Anatomy and physiology, chapter 6.3 : Bone structure. <https://open.oregonstate.edu/aandp/chapter/6-3-bone-structure/>. Accessed on 08/10/2021.
- [3] Anwar R. Padhani Philippe Clézardin Edward Chow Marie Fallon Theresa Guise-Simone Colangeli Rodolfo Capanna Luis Costa Robert E. Coleman, Peter I. Croucher. Bone metastases. *Nat Rev Dis Primers*, 6(83), 2020.
- [4] Fernando Salvador, Alicia Llorente, and Roger R Gomis. From latency to overt bone metastasis in breast cancer: potential for treatment and prevention. *The Journal of Pathology*, 249(1):6–18, 2019.
- [5] Francisco P.M. Oliveira and João Manuel R.S. Tavares. Medical image registration: a review. *Computer Methods in Biomechanics and Biomedical Engineering*, 17(2):73–93, 2014. PMID: 22435355.
- [6] Barbara Zitova. Mathematical approaches for medical image registration. In Roger Narayan, editor, *Encyclopedia of Biomedical Engineering*, pages 21–32. Elsevier, Oxford, 2019.
- [7] Nafaa Nacereddine, Salvatore Tabbone, and Djemel Ziou. Similarity transformation parameters recovery based on radon transform. application in image registration and object recognition. *Pattern Recognition*, 48(7):2227–2240, 2015.
- [8] MathWorks. Help center : radon. <https://nl.mathworks.com/help/images/ref/radon.html>. Accessed on 2021-07-27.
- [9] Askshay L Chandra. Mcculloch-pitts neuron — mankind’s first mathematical model of a biological neuron. <https://towardsdatascience.com/mcculloch-pitts-model-5fdf65ac5dd1>, July 2018. Accessed on 2021-07-07.
- [10] Patrick Winston for MIT OpenCourseWare. Mit 6.034 artificial intelligence, lecture 12a : Neural nets. [https://www.youtube.com/watch?v=uXt8qF2Zzfo&ab\\_channel=MITOpenCourseWare](https://www.youtube.com/watch?v=uXt8qF2Zzfo&ab_channel=MITOpenCourseWare), April 2016. Accessed on 2021-07-07.
- [11] H. Taud and J.F. Mas. *Multilayer Perceptron (MLP)*, pages 451–455. Springer International Publishing, Cham, 2018.

- [12] P.Geurts L.Wehenkel. Introduction to machine learning, lecture 5 : Artificial neural networks. [https://people.montefiore.uliege.be/lwh/AIA/IML\\_\\_\\_Neural\\_networks.pdf](https://people.montefiore.uliege.be/lwh/AIA/IML___Neural_networks.pdf), September 2020. Accessed on 2021-07-09.
- [13] Stanford CS class : CS231n Convolutional Neural Networks for Visual Recognition. Module 2 : Convolutional neural networks. <https://cs231n.github.io/convolutional-networks/>. Accessed on 2021-07-12.
- [14] Mathworks. Convolutional neural network - 3 things you need to know. <https://www.mathworks.com/solutions/deep-learning/convolutional-neural-network.html>. Accessed on 2021-07-12.
- [15] Kaiming He, Xiangyu Zhang, Shaoqing Ren, and Jian Sun. Deep residual learning for image recognition. *CoRR*, abs/1512.03385, 2015.
- [16] A. et al. Villasante. Tissue-engineered model of human osteolytic bone tumor. *Tissue engineering. Part C, Methods*, 23:98–107, 2017.
- [17] Ashley Kiemen, Alicia M. Braxton, Mia P. Grahn, Kyu Sang Han, Jaanvi Mahesh Babu, Rebecca Reichel, Falone Amoa, Seung-Mo Hong, Toby C. Cornish, Elizabeth D. Thompson, Laura D. Wood, Ralph H. Hruban, Pei-Hsun Wu, and Denis Wirtz. In situ characterization of the 3d microanatomy of the pancreas and pancreatic cancer at single cell resolution. *bioRxiv*, 2020.
- [18] Napakorn Sangchay. *Impact of nitric acid exposure on the morphometric analysis of osteon*. PhD thesis, 08 2015.
- [19] Michael A Wirth. Shape and analysis measurement. <http://www.cyto.purdue.edu/cdroms/micro2/content/education/wirth10.pdf>. Accessed on 08/20/2021.
- [20] MathWorks. Help center : trainingoptions. <https://nl.mathworks.com/help/deeplearning/ref/trainingoptions.html>. Accessed on 2021-08-01.
- [21] American Cancer Society. Cancer facts and figures 2021. <https://www.cancer.org/content/dam/cancer-org/research/cancer-facts-and-statistics/annual-cancer-facts-and-figures/2021/cancer-facts-and-figures-2021.pdf>, 2021. Accessed on 2021-05-18.
- [22] Fondation Contre le Cancer. Cancer du sein - généralités. <https://www.cancer.be/les-cancers-types-de-cancers-liste-z/cancer-du-sein>, November 2020. Accessed on 2021-05-18.
- [23] Fondation Contre le Cancer. Cancer de la prostate - généralités. <https://www.cancer.be/les-cancers/types-de-cancers/cancer-de-la-prostate>, March 2020. Accessed on 2021-05-18.
- [24] Llorente A. Gomis R. R. Salvador, F. From latency to overt bone metastasis in breast cancer: potential for treatment and prevention. *The Journal of pathology*, 249(1):6–18, 2019.
- [25] Zhao D. Spring D. J. DePinho R. A. Wang, G. Genetics and biology of prostate cancer. *Genes development*, 32(17-18):1105–1140, 2018.

- [26] Jaime Fornetti, Alana L Welm, and Sheila A Stewart. Understanding the bone in cancer metastasis. *Journal of Bone and Mineral Research*, 33(12):2099–2113, 2018.
- [27] Toru Hiraga. Bone metastasis: Interaction between cancer cells and bone microenvironment. *Journal of Oral Biosciences*, 61(2):95–98, 2019.
- [28] Aranzazu Villasante Gordana Vunjak-Novakovic. Tissue-engineered three-dimensional model for tumor analysis, u.s. patent number 10,883,083. <https://uspto.report/patent/grant/10,883,083>, 2018.
- [29] Jung-Min Kim, Chujiao Lin, Zheni Stavre, Matthew B. Greenblatt, and Jae-Hyuck Shim. Osteoblast-osteoclast communication and bone homeostasis. *Cells*, 9(9), 2020.
- [30] Xiangyu Zhang. Interactions between cancer cells and bone microenvironment promote bone metastasis in prostate cancer. *Cancer Commun*, 39(76), 2019.
- [31] Sheila A Stewart Jaime Fornetti, Alana L Welm. Understanding the bone in cancer metastasis. *Journal of Bone and Mineral Research*, 33(12), 2018.
- [32] Ren Xu, Xiaotao Zhou, Shike Wang, and Christine Trinkle. Tumor organoid models in precision medicine and investigating cancer-stromal interactions. *Pharmacology Therapeutics*, 218:107668, 2021.
- [33] Clevers H. Drost, J. Organoids in cancer research. *Nat Rev Cancer*, 18:407–418, 2018.
- [34] Lara S. Costard, Ryan R. Hosn, Harumi Ramanayake, Fergal J. O’Brien, and Caroline M. Curtin. Influences of the 3d microenvironment on cancer cell behaviour and treatment responsiveness: A recent update on lung, breast and prostate cancer models. *Acta Biomaterialia*, 2021.
- [35] A Ardeshir Goshtasby. *Image Registration : Principles, Tools and Methods*. 2191-6586. Springer-Verlag London, 2012.
- [36] Bernd Fischer and Jan Modersitzki. Ill-posed medicine—an introduction to image registration. *Inverse Problems*, 24(3):034008, may 2008.
- [37] Barbara Zitová and Jan Flusser. Image registration methods: a survey. *Image and Vision Computing*, 21(11):977–1000, 2003.
- [38] T. Long G. He Y. Dong, W. Jiao and C. Gong. An extension of phase correlation-based image registration to estimate similarity transform using multiple polar fourier transform. *Remote Sensing*, 10, 10 2018.
- [39] M. Radermacher. Radon transform techniques for alignment and three-dimensional reconstruction from random projections. 1997.
- [40] Sigurdur Helgason. *The Radon transform*. Progress in mathematics 5. Birkhäuser, Boston, 1980.
- [41] MathWorks. Help center : xcorr2. <https://nl.mathworks.com/help/signal/ref/xcorr2.html>. Accessed on 2021-07-27.

- [42] Ian Goodfellow, Yoshua Bengio, and Aaron Courville. *Deep Learning*. MIT Press, 2016. <http://www.deeplearningbook.org>.
- [43] Hinton G Lecun Y, Bengio Y. Deep learning. *Nature*, 28, May 2015. PMID: 26017442.
- [44] Majid M. Qayyum A. et al. Anwar, S.M. Medical image analysis using convolutional neural networks: A review. *J Med Syst*, 42:226, 2018.
- [45] L. Deng and Dong Yu. Deep learning: Methods and applications. *Found. Trends Signal Process.*, 7:197–387, 2014.
- [46] Bengio Y Lecun Y, Bottou L and Haffner P. Gradientbased learning applied to document recognition. *Proc. IEEE*, 86(11):2278–2324, 1998.
- [47] Neena Aloysius and Geetha M. A review of deep convolutional neural networks. *International Conference on Communication and Signal Processing*, April 2017.
- [48] Srinivasan. An ultimate guide to understanding semantic segmentation. <https://www.digitalvidya.com/blog/semantic-segmentation/>. Accessed on 2021-07-27.
- [49] University of Toronto Tingwu Wang, Machine learning Group. Semantic segmentation. [https://www.cs.toronto.edu/~tingwuwang/semantic\\_segmentation.pdf](https://www.cs.toronto.edu/~tingwuwang/semantic_segmentation.pdf). Accessed on 2021-07-27.
- [50] Mayank Mishra. Convolutional neural networks, explained. <https://towardsdatascience.com/convolutional-neural-networks-explained-9cc5188c4939>. Accessed on 2021-07-14.
- [51] R.M. Neal. Pattern recognition and machine learning. *Technometrics*, 49:366–366, 2007.
- [52] T.Kudo W.Graf M.Covert D.Van Valen E.Moen, D.Bannon. Deep learning for cellular image analysis. *Nature Methods*, 16:1233–1246, December 2019.
- [53] Diederik P. Kingma and Jimmy Ba. Adam: A method for stochastic optimization, 2017.
- [54] P.D.D Dominic N.M Aszemi. Hyperparameter optimization in convolutional neural network using genetic algorithms. *International Journal of Advanced Computer Science and Applications (IJACSA)*, 10(6), 2019.
- [55] Aakash Kauskik. Understanding resnet50 architecture. <https://iq.opengenus.org/resnet50-architecture/>. Accessed on 2021-07-22.
- [56] Nicholas Trahearn, David Snead, Ian Cree, and Nasir Rajpoot. Multi-class stain separation using independent component analysis. 9420:113 – 123, 2015.
- [57] Arnout Ruifrok and Dennis Johnston. Quantification of histochemical staining by color deconvolution. *Anal Quant Cytol Histol*, 23, 01 2001.
- [58] Trahearn N. Raza S. E. Snead D. Rajpoot N. M. Alsubaie, N. Stain deconvolution using statistical analysis of multi-resolution stain colour representation. *PLoS one*, 12, 01 2017.

- [59] Columbia University in the city of New York. Gordana vunjak-novakovic, principal investigator. <https://gvnlab.bme.columbia.edu/people/gordana-vunjak-novakovic>. Accessed on 08/23/2021.
- [60] Liang-Chieh Chen, Yukun Zhu, G. Papandreou, Florian Schroff, and Hartwig Adam. Encoder-decoder with atrous separable convolution for semantic image segmentation. *ArXiv*, abs/1802.02611, 2018.
- [61] Gabriel Landini, Giovanni Martinelli, and Filippo Piccinini. Colour deconvolution: stain unmixing in histological imaging. *Bioinformatics*, 09 2020. btaa847.
- [62] Pei-Hsun Wu, Christopher M Hale, Wei-Chiang Chen, Jerry S H Lee, Yiider Tseng, and Denis Wirtz. High-throughput ballistic injection nanorheology to measure cell mechanics. *Nature Protocols*, 7(1):155–170, jan 2012.
- [63] A.Natan. Fast 2d peak finder. <https://nl.mathworks.com/matlabcentral/fileexchange/37388-fast-2d-peak-finder>, 2021. Accessed on 2021-05-26.
- [64] Wikipedia The Free Encyclopedia. H&e stain. [https://en.wikipedia.org/wiki/H%26E\\_stain](https://en.wikipedia.org/wiki/H%26E_stain). Accessed on 08/18/2021.
- [65] Tan J et al. Hart NH, Newton RU. Biological basis of bone strength: anatomy, physiology and measurement. *J Musculoskelet Neuronal Interact.*, 20(3):347–371, 2020.
- [66] Joseph Ronsin Mingqiang Yang, Kidiyo Kpalma. A survey of shape feature extraction techniques. *Pattern Recognition, IN-TECH, fhal-00446037f*, 20(3):43–90, 2008.
- [67] Andre da Veiga Ferro Forjaz Pereira. Master thesis : Cnn classification of immune cells in tumor sections. (técnico lisboa), 09 2020.
- [68] Alfi DM et al. Bhumiratana S, Bernhard JC. Tissue-engineered autologous grafts for facial bone reconstruction. *Sci Transl Med.*, 8, 2016.
- [69] Merriam-Webster Dictionary. Lacuna definition. <https://www.merriam-webster.com/dictionary/lacuna>. Accessed on 2021-07-29.
- [70] Anh D. Le and Jimmy James Brown. Chapter 2 - wound healing: Repair biology and wound and scar treatment. In Shahrokh C. Bagheri, R. Bryan Bell, and Husain Ali Khan, editors, *Current Therapy In Oral and Maxillofacial Surgery*, pages 6–10. W.B. Saunders, Saint Louis, 2012.
- [71] Javad Parvizi and Gregory K. Kim. Chapter 39 - cartilage. In Javad Parvizi and Gregory K. Kim, editors, *High Yield Orthopaedics*, pages 80–81. W.B. Saunders, Philadelphia, 2010.